博士論文

Measurement of Branching Fractions as well as Isospin and CP Asymmetries in $B \to K^*\gamma$ Decays at the Belle experiment
(Belle 実験における $B \to K^*\gamma$ 崩壊を用いた 崩壊分岐比及びアイソスピン、CP 非対称性の測定)

堀口 朋裕

平成 28 年

Abstract

The decay of $B \to K^*(892)\gamma$ is one of the most sensitive decays to new physics in $b \to s$ transition because it has large branching fraction and there are small amount of backgrounds since $K^*(892)$ is far from higher kaon resonances. The target of this study is to obtain the final Belle result of the branching fractions ($\mathcal{B}$), direct CP asymmetry(A_{CP}), isospin asymmetry (Δ_{0-}) and the difference of CP asymmetry between charged and neutral B decay (ΔA_{CP}).

We use the full data set around $\Upsilon(4S)$ resonance accumulated by the Belle experiment which is corresponding to 772 million $B\overline{B}$ pairs. The obtained results are

$$\begin{aligned}
\mathcal{B}(B^0 \to K^{*0}\gamma) &= (3.99 \pm 0.07 \pm 0.14) \times 10^{-5}, \\
\mathcal{B}(B^+ \to K^{*+}\gamma) &= (3.75 \pm 0.09 \pm 0.12) \times 10^{-5}, \\
A_{CP}(B^0 \to K^{*0}\gamma) &= -0.013 \pm 0.017 \pm 0.001, \\
A_{CP}(B^+ \to K^{*+}\gamma) &= 0.008 \pm 0.024 \pm 0.002, \\
A_{CP}(B \to K^*\gamma) &= -0.006 \pm 0.014 \pm 0.001, \\
\Delta_{0-} &= 0.067 \pm 0.015 \pm 0.013 \quad \text{and} \\
\Delta A_{CP} &= 0.021 \pm 0.029 \pm 0.002
\end{aligned}$$

where the first and second uncertainties are statistical and systematic ones, respectively. Both the branching fractions in the decay of $B^0 \to K^{*0}\gamma$ and $B^+ \to K^{*+}\gamma$ are consistent to the previous results within 1 σ. Obtained CP asymmetries are consistent width zero within 1σ. Obtained isospin asymmetries are close to the standard model prediction and this measurement is the first evidence of isospin violation in $B \to K^*\gamma$ with 3.4 σ precision. The ΔA_{CP} for $B \to K^*\gamma$ is the first measurement. Since in the standard model prediction, ΔA_{CP} is zero, obtained value is the standard model consistent.

The highest measurement accuracies in the world are updated by all observable obtained in this study.

Acknowledgment

First, I would like to express my appreciation to my supervisor Prof. Hitoshi Yamamoto for giving me a opportunity to research in high energy physics. What I could study the physics in both ILC and Belle physics under him is great fortune for me. I also appreciate Dr. Akimasa Ishikawa deeply for his pertinent advises. Without his great support, I could not write this thesis.

I would like to thank to the internal referees in the Belle collaboration. Dr. Shohei Nishida, Dr. Yutaro Sato and Dr. Tobias Weber gave me a lot of valuable suggestions to lead right direction.

I am deeply thankful to all the members of the Belle Ⅱ SVD group. When I collaborated the assembly and R&D of the SVD for Belle Ⅱ, I received many advice and learned the machine tooling. I am specially grateful to Dr. Takeo Higuchi, Dr. Tomoko Morii who are member of the Kavli IPMU and Nobuhiko Sato who is the expert of detector development in KEK.

I would like to thank Dr. Tomoyuki Sanuki and Dr. Tadashi Nagamine for their encouragements. I am deeply thankful to the secretary Ms. Kaori Kobayashi, for taking care of every official business. It is my pleasure to express my biggest thanks to all the members in this laboratory.

At last, I am deeply grateful to my family, my father Hideo and my mother Michiko and my sisters Akiko and Naoko, who gave me so many supports and encouraged me. Thanks to everyone, I wrote up this thesis.

Respectfully
Tomohiro Horiguchi

Contents

Chapter 1

Introduction

There is the standard model (SM) which is the well-formed theory in the elemental particle physic, consists of quark and lepton, gauge interaction and Higgs mechanism. A lot of the experimental results are consistent to the SM, therefore the correctness of the SM has been proved. Especially, it is emphasized by discovering the Higgs boson which is the SM particle found out finally at the ATLAS and the CMS experiment which are in CERN (European Organization for Nuclear Research) in 2012 [1][2].

However, the results which can not be explained in the SM are found. For example, the existence of dark matter is not able to probe in the SM but it is suggested by the galaxy rotation problem [3]. Furthermore, we can not understand the baryogenesis and why number of particles are much grater than that of anti-particles under only the SM.

The particle physicists have suggested a lot of theoretical models and their correctness are tested by a lot of the experiments. The experiment using accelerator is the one of the major experiments for testing the SM and searching the new physics (NP) which means the theory beyond the SM. This type of experiments are performed by reproducing the early universe by making collisions with electrons, protons or other heavy particles which are accelerated close to light speed. There are two kind of accelerator experiments, energy frontier experiment and intensity frontier one. The energy frontier experiment is the one that new particles are generated and detected directly by raising the center-of-mass energy around the energy scale near existing NP candidates. The accelerator with the highest center-of-mass energy, 14 TeV, is LHC (Large Hadron Collider) in CERN. The results reported from them are consistent to the standard model predictions, so this suggests that the NP candidates do not exist near $\mathcal{O}(1)$ TeV. The major energy frontier experiments are the ATLAS and the CMS using LHC accelerator and the CDF and the D0 experiments using Tevatron at which top quark was discovered. Their collisions are performed by proton-proton for LHC and proton-anti-proton Tevatron, which composite particles are used in both experiments for reaching above 1 TeV. In the future, we expect to achieve 1 TeV with electron-positron collision by International Linear Collider (ILC) for testing the NP more precisely.

In the intensity frontier experiments, the NP searches and test of the SM are performed by measuring the deviation of some observables from the SM predictions using the rare decays precisely. The typical examples are the MEG for searching the lepton flavor violation using the decay of $\mu \to e\gamma$, T2K for measuring some neutrino features such as mixing angle θ_{13} and CP asymmetry using the long baseline neutrino oscillation and Belle and BaBar using measuring the decay of B meson. As the Belle and the BaBar experiments, the experiments which can generate huge B mesons are called "B-factory". A lot of measurements for the NP in B-factory are expected the deviation from the SM prediction by quantum effect including NP effect. These measurements are

sensitive to the NP below $\mathcal{O}(100)$ TeV.

The transition of $b \to s\gamma$ is one of the sensitive decays in the B decay. The tree level diagram of this process which is so-called Flavor Changing Neutral Current (FCNC) is strongly suppressed in the SM and the one-loop diagram is lowest order [4].If the NP effects contribute in the loop, some measurements should be deviated from the SM prediction.

In this paper, we report the measurement of the branching fractions, direct CP asymmetries, isospin asymmetries and the difference of CP asymmetry between charged and neutral B using the decay of $B \to K^*(892)\gamma$. In this paper, K^* means $K^*(892)$ without specific mention. This channel is the most sensitive to the NP in $b \to s\gamma$ decays because $K^*(892)$ is the lowest kaonic resonance which has narrow width and the final state is two-body system with almost 100% branching fraction, so this process can be predicted with high precision and analysis can be performed with small amount of backgrounds. The Belle group has 772 million $B\overline{B}$ pairs which is the world record therefore obtained results will able to be the most sensitive one to the NP in the world.

Following sentence shows the outline of this thesis. In section-2, the physics motivation for study of $b \to s\gamma$ is described, in section-3, the experimental equipment such as accelerator and sub-detectors are explained, in section-4, the Monte Carlo simulation condition is introduced, in section-5, event reconstruction procedure is described, in section-6, background suppression methods are shown, in section-7, the methods of signal extraction is explained, in section-8, the sources of systematic uncertainty are listed and estimation method of them are described, in section-9, the obtained results are shown and discussion for sensitivity or limit for some new physics models and we conclude this paper in section-10.

Chapter 2

Physics Motivation

2.1 Introduction of Radiative B Meson Decay

The B meson is the bound state of b quark and a light quark. Since the mass of b quark is much larger than typical strong interaction scale, good theoretical predictions are obtained comparing other mesons' decays. Therefore the B meson provides excellent study environment.

So-called radiative penguin process such as $b \to s\gamma$ is the decay which is one of the Flavor Changing Neutral Current (FCNC) processes and has prompt photon emitted from heavy particles in the loop contribution. Figure-2.1.1 shows the Feynman diagram of radiative penguin process in the SM and some new physics contribution candidates. The tree diagram of radiative penguin decays is forbidden in the SM and the lowest order of them is one loop. The contributions in the loop diagram in the typical $b \to s\gamma$ are the top quark and the W boson in the SM. Instead of the them some new particles can be contributed like Figure-2.1.1, at the model beyond the SM. Other decay of radiative penguin process is $b \to d\gamma$ which is suppressed about 1/100 of $b \to s\gamma$ by CKM factor ($|V_{td}/V_{ts}|^2 \sim 0.01$). Furthermore electroweak penguin process such as $b \to s(d)\ell\ell$ is also calculated with similar theoretical framework to the decay of $b \to s\gamma$.

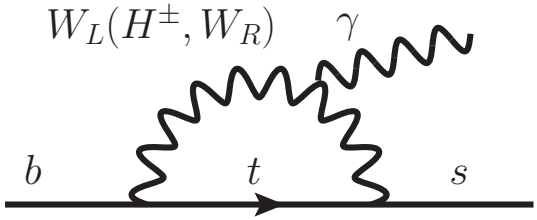

Figure 2.1.1: Feynman diagram of $b \to s\gamma$ decay in the standard model and some new physics contribution candidates. W_L is W boson coupling to left-handed current, and both of $H^{\pm}$ (charged Higgs) and W_R (W boson coupling to right-handed current) are particles in some new physic models.

From 1993 when the first measurement of radiative penguin process was reported in CLEO experiment using $B \to K^*(892)\gamma$ [5], both theoretical prediction and precision of measurements have been improved. In this section, we introduce the theoretical approach and analysis methods and summarize the current measurement status.

2.2 Electroweak Effective Hamiltonian

In general, the theoretical precision of exclusive method is much worse than that of inclusive one because of form factor uncertainty. However, some observables evaluated by calculating the ratio are sensitive to the NP. The radiative penguin decays are governed by an interplay between the weak and strong interactions. Since hard-gluon exchange arises at the quark line in the one loop and enhances the decay rate, to understand it is important.

The perturbative QCD corrections that arise from hard-gluon exchange bring in large logarithms of the form $\alpha_s^n(m_b)\log^m(m_b/M)$ where α_s is the strong coupling constant, $m \leq n$ (with $n = 0, 1, 2, \cdots$) and M is the mass of top quark or W boson [6][7]. There is the feature that these logarithms have to be considered on the two mass scale in the any decay modes. The results are obtained by calculating the summation at least all the leading-log terms with $m = n$, or $\alpha_s^n \log^2(m_b/M)$ with helping of renormalization-group techniques. Next-to-leading-log or next-to-next-to-leading-log calculation method in which the index of m is considered by $n-1$ or $n-2$ are needed for obtaining more precise results.

A suitable framework in which to achieve the satisfied calculation of the large logarithms is an effective low-energy theory with five quarks; this framework is obtained by integrating out the heavy particles which are top quark and electroweak bosons. This effective field theory approach can be applied both exclusive and inclusive methods as theoretical framework.

The standard method of the operator product expansion (OPE) [8][9] allows for a separation of the B meson decay amplitude into two district parts, the long-distance contributions contained in the operator matrix elements and the short-distance physics described by the Wilson coefficients. The electroweak effective Hamiltonian can be written as

$$\mathcal{H}_{\text{eff}} = -\frac{4G_F}{\sqrt{2}} \sum_i \lambda_{\text{CKM}} C_i(\mu, M)\mathcal{O}(\mu) \tag{2.2.0.1}$$

where $\mathcal{O}_i(\mu)$ are the operators of dimension six, $C_i(\mu, M)$ are the corresponding Wilson coefficients, λ_{CKM} are products of CKM matrix elements, and μ is the factorization scale. The top quark and W boson mass dependence are included in the Wilson coefficients completely, because the heavy fields are integrated out. The scale dependence (μ) should be canceled by the effective theory condition.

The effective electroweak Hamiltonian focus to radiative penguin decay in the SM is given as

$$\mathcal{H}_{\text{eff}} = -\frac{4G_F}{\sqrt{2}} \left[\lambda_q^t \sum_{i=1}^{10} C_i\mathcal{O}_i + \lambda_q^u \sum_{i=1}^{2} C_i(\mathcal{O}_i - \mathcal{O}_i^u) \right] \tag{2.2.0.2}$$

where G_F is fermi coupling constant λ_q^t and λ_q^u are the CKM factors described as $V_{tb}V_{tq}^*$ and $V_{ub}V_{uq}^*$ $(q = s, d)$[10]. There is the unitarity relation, $\lambda_q^t + \lambda_q^c + \lambda_q^u = 0$. The dimension-six operators $\mathcal{O}_i^{(u)}$ are defined as

$$\mathcal{O}_1 = (\bar{s}_L\gamma_\mu T^a c_L)(\bar{c}_L\gamma^\mu T^a b_L), \quad (2.2.0.3)$$

$$\mathcal{O}_2 = (\bar{s}_L\gamma_\mu c_L)(\bar{c}_L\gamma_\mu b_L), \quad (2.2.0.4)$$

$$\mathcal{O}_1^u = (\bar{s}_L\gamma_\mu T^a u_L)(\bar{u}_L\gamma^\mu T^a b_L), \quad (2.2.0.5)$$

$$\mathcal{O}_2^u = (\bar{s}_L\gamma_\mu u_L)(\bar{u}_L\gamma_\mu b_L), \quad (2.2.0.6)$$

$$\mathcal{O}_3 = (\bar{s}_L\gamma_\mu b_L)\sum_{q=u,d,c,s,b}(\bar{q}_L\gamma^\mu q_L), \quad (2.2.0.7)$$

$$\mathcal{O}_4 = (\bar{s}_L\gamma_\mu T^a b_L)\sum_{q=u,d,c,s,b}(\bar{q}_L\gamma^\mu T^a q_L), \quad (2.2.0.8)$$

$$\mathcal{O}_5 = (\bar{s}_L\gamma_\mu b_L)\sum_{q=u,d,c,s,b}(\bar{q}_R\gamma^\mu q_R), \quad (2.2.0.9)$$

$$\mathcal{O}_6 = (\bar{s}_L\gamma_\mu T^a b_L)\sum_{q=u,d,c,s,b}(\bar{q}_R\gamma^\mu T^a q_R), \quad (2.2.0.10)$$

$$\mathcal{O}_7 = \frac{e}{16\pi^2}m_b(\bar{s}_L\sigma^{\mu\nu}b_R)F_{\mu\nu}, \quad (2.2.0.11)$$

$$\mathcal{O}_8 = \frac{g_s}{16\pi^2}m_b(\bar{s}_L\sigma^{\mu\nu}T^a b_R)G^a_{\mu\nu}, \quad (2.2.0.12)$$

$$\mathcal{O}_9 = \frac{e^2}{16\pi^2}(\bar{s}_L\gamma_\mu b_L)\sum_\ell(\bar{\ell}\gamma^\mu\ell), \quad (2.2.0.13)$$

$$\mathcal{O}_{10} = \frac{e^2}{16\pi^2}(\bar{s}_L\gamma_\mu b_L)\sum_\ell(\bar{\ell}\gamma^\mu\gamma_5\ell), \quad (2.2.0.14)$$

where T^a are $SU(3)$ color generators, $F_{\mu\nu}$ and $G_{\mu\nu}$ are electromagnetic and chromomagnetic fields, and the subscripts L and R refer to the left- and right-handed components of the fermion fields. In the transition of $b \to s$, the contributions proportional to λ_s^u are rather small, while in the decays of $b \to d$, where λ_d^u is of the same order as λ_d^t, these contributions play an important role in CP and isospin asymmetries. Figure-2.2.1 shows the tree-level annihilation Feynman diagram of the contribution of λ_d^u, which is not a penguin process. $\mathcal{O}_1$ and $\mathcal{O}_2$ are the current-current operators, the operators of $\mathcal{O}_{3-6}$ describe the so-called QCD penguin process, $\mathcal{O}_7$ and $\mathcal{O}_8$ are the electromagnetic and chromomagnetic operators, and $\mathcal{O}_9$ and $\mathcal{O}_{10}$ are the operators for the vector and axial components of electroweak penguin operators, respectively. Since the operators of $\mathcal{O}_9$ and $\mathcal{O}_{10}$ have two leptons, these are only used in the electroweak penguin decay like $b \to s(d)\ell\ell$ and $b \to s(d)\nu\nu$. Using the renormalization group technique, scale factor μ and model independent Wilson coefficients C_i can be calculated, therefore new physics search is performed by measuring and comparing them to the prediction of the SM.

The Wilson coefficients are calculated with perturbative methods in both inclusive and exclusive modes. In exclusive process, we have to consider hadronizing process with estimating matrix elements between meson states. The method of QCD-improve factorization (QCDF)[10][11] which has been systematically formalized for non-leptonic decays in the heavy quark limit $m_b \to \infty$ is the approach having a good agreement. Using this method, perturbative calculation of QCD corrections to naive factorization is provided but this method have the uncertainty of the approximation of $m_b \to \infty$. Current predictions of exclusive penguin decay are calculated based on QCDF methods.

As other useful approach, soft collinear effective theory (SCET)[12] is introduced briefly here. This method is also used for calculating of the current prediction in exclusive decays. SCET approach is trying to solve the multi-scale problem. There are set three energy scales:

(a) Λ = few $\times\Lambda_{\rm QCD}$, where $\Lambda_{\rm QCD}$ is QCD scale, the soft scale set by the typical energies and momenta of the light degree of freedom in the hadronic bound state,

(b) m_b, the hard scale set by both the heavy b quark mass and the energy of the final state hadrons in the B meson rest frame, and

(c) $\mu = \sqrt{m_b\Lambda}$ the hard-collinear scale which appears through interactions between the soft and energetic modes in the initial and final states. This part can be calculated perturbatively in the heavy quark limit.

Thus SCET described the decays of B meson into light hadrons with energies much larger than their masses, assuming that their constituents have momenta collinear to the hadron momentum.

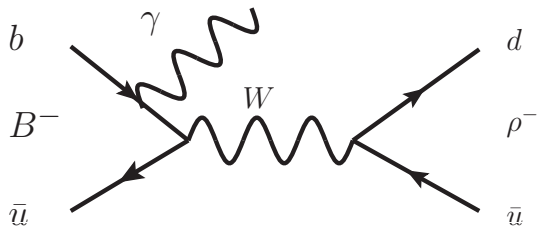

Figure 2.2.1: The Feynman diagram of the contribution of λ_d^u in $B \to \rho\gamma$ annihilation.

2.3 Analysis Method

For radiative and electroweak penguin process, there are two kind of analysis methods, exclusive and inclusive.

2.3.1 Exclusive Analysis

In the exclusive analysis, the specific decay modes are reconstructed perfectly by associating some particles which have long life time such as γ, K, π, e, μ and proton. The intermediate particles are also reconstructed by forming them and requiring the invariant mass condition. The advantage of exclusive method is excellent background suppression performance with requiring kinematic constraint, whereas there are two major disadvantages. One can not obtain the result with high sensitivity due to small amount of events, the other is the precision of the theoretical prediction have large uncertainty due to form factor.

In the decay of $B \to K^*\gamma$, the branching fraction is the largest in the $b \to s\gamma$ transitions and we have 772×10^6 B meson pairs which are corresponding to the world record so former problem is not significant. Furthermore this channel is the lowest kaonic resonance whose width is narrow, far from higher X_s resonance as Figure-2.3.1, therefore the large combinatorial background candidates can be suppressed.

2.3.2 Inclusive Analysis

The major advantage of the inclusive analysis is that theoretical prediction power is much grater than exclusive one because of avoiding form factor uncertainty. In the inclusive analysis of radiative and electroweak penguin process, we have two kind of inclusive analysis methods, which

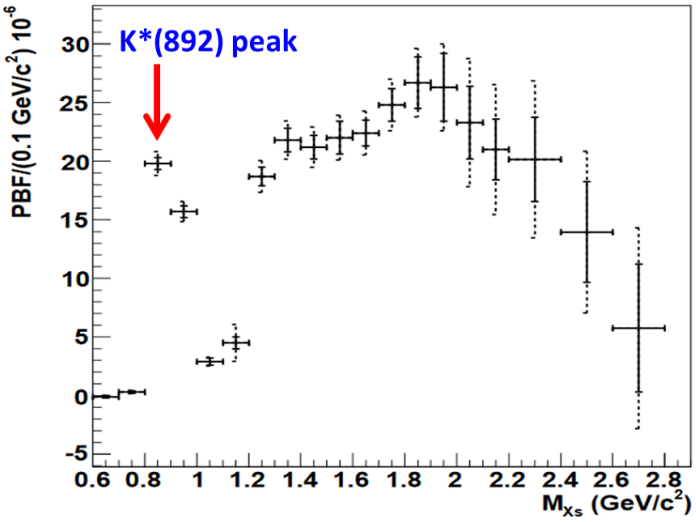

Figure 2.3.1: The plot of the branching fraction each X_s mass bin (100 MeV/c^2 step) [15]. Clear peak can be found near 900 MeV.

are the fully-inclusive and sum-of-exclusive methods. The reconstruction strategy of fully-inclusive method is only capturing the prompt photon therefore background suppression is challenging. The sum-of-exclusive method is that many final states are reconstructed exclusively and are summed. The amount of backgrounds in sum-of-exclusive method are smaller than in fully-inclusive one.

2.4 Previous Measurements

Current status of measurement of $b \to s\gamma$ process are summarized in this section.

2.4.1 Inclusive Measurement

We can obtain the precise theoretical prediction of the branching fraction in inclusive B decay in the SM with good agreement because of small hadronization uncertainty. The main contribution for radiative penguin process is the electroweak FCNC term, therefore the term including $\mathcal{O}_7$ and C_7 is the most sensitive. The matrix element and decay width of the decay of $B \to X_s\gamma$ is given [13] as

$$\mathcal{M}(b \to s\gamma) = \frac{4G_F}{\sqrt{2}} \frac{e}{16\pi^2} V_{ts}^* V_{tb} m_b C_7 (\bar{s}\sigma_{\mu\nu} b_R) F^{\mu\nu}, \quad (2.4.1.1)$$

$$\Gamma(b \to s\gamma) = \frac{G_F^2 \alpha_{em} m_b^5}{32\pi^4} |C_7|^2 |V_{tb} V_{ts}^*|^2. \quad (2.4.1.2)$$

Current predicted branching fraction in next-to-next-to leading order precision is $\mathcal{B}(B \to X_s\gamma) = (3.15 \pm 0.23) \times 10^{-4}$ for a photon energy 1.6 GeV in B meson rest frame [16]. The branching fraction of $B \to X_s\gamma$ has been measured in BaBar and Belle. The current world averages are summarized in Table-2.4.1.

	Branching Fraction (10^{-4})
Belle	3.28 ± 0.20
BaBar	3.41 ± 0.28
CLEO	3.29 ± 0.53
Average	3.32 ± 0.15

Table 2.4.1: The branching fraction of $B \to X_s\gamma$

The $B \to X_s\gamma$ branching fraction is consistent to the SM predictions. This branching fraction is sensitive to the charged Higgs boson mass in the two-Higgs doublet model. The charged Higgs mass is excluded below 238 GeV/c^2 by these results [14].

2.4.2 Exclusive $b \to s\gamma$ Measurement

The branching fraction of $B \to K^*\gamma$ is calculated by SCET and QCDF approach. Considering the hadronization in Eq-2.4.1.2, the decay width can be given as

$$\Gamma(B \to K^*\gamma) = \frac{G_F^2\alpha_{em}}{32\pi^4} m_b^2 M_B^2 |V_{tb}V_{ts}^*|^2 |\xi_\perp(0)|^2 (1 - \frac{m_{K^*}^2}{M_B^2}) \Big[C_7^{\text{eff}} + A\Big]^2, \quad (2.4.2.1)$$

where $\xi_\perp(0)$ is the soft form factor. The next-to-leading order theoretical prediction [17] in the SM is calculated as

$$\mathcal{B}(\overline{B}^0 \to \overline{K}^{*0}\gamma) = 3.36^{+1.62}_{-1.30}(F_{K^*})^{+0.62}_{-0.60}(\mu)^{+0.23}_{-0.09}(\lambda_B) \pm 0.20(m_c) \times 10^{-5}, \quad (2.4.2.2)$$

$$\mathcal{B}(\overline{B}^- \to \overline{K}^{*-}\gamma) = 3.34^{+1.66}_{-1.32}(F_{K^*})^{+0.28}_{-0.47}(\mu)^{+0.33}_{-0.12}(\lambda_B) \pm 0.20(m_c) \times 10^{-5}. \quad (2.4.2.3)$$

Because of the large form factor (F_{K^*}) uncertainty with approximately 30%, the branching fraction of the decay of $B \to K^*\gamma$ is insensitive to the NP. The branching fraction of $B \to K^*\gamma$ has been measured in BaBar and Belle and they are summarized in Table-2.4.2. These results are consistent to the SM predictions.

However, the values which are calculated by the ratios such as CP asymmetry and isospin asymmetry which are the differences between negative and positive charge and between flavors are sensitive to the NP because the form factor uncertainty can be canceled.

Direct CP asymmetry is arisen by the contribution from weak and strong CP phase and the interference of the decay amplitudes. The CP phase of the decay of $B \to K^*\gamma$ is negligible and there are only one major diagram therefore the direct CP is close to zero in the SM. However if the NP which have CP phase exist, the CP asymmetry can appear. Direct CP asymmetry is derived as following calculation. When $\theta_{\text{SM/NP}}$ and $\delta_{\text{SM/NP}}$ are given as weak and strong CP phases of the SM/NP and $\mathcal{A}$ and A are denoted as decay amplitude and the part of decay amplitude except CP phase, the amplitudes of SM and NP in $B \to K^*\gamma$ can be represented by

$$\mathcal{A}_{\text{SM}}(B \to K^*\gamma) = A_{\text{SM}} e^{i\delta_{\text{SM}}} \text{ and}$$
$$\mathcal{A}_{\text{NP}}(B \to K^*\gamma) = A_{\text{SM}} e^{i(\theta_{\text{NP}} + \delta_{\text{NP}})},$$

and

Observable	Experiment	Value	nBB (10^6)
$\mathcal{B}(B^0 \to K^{*0}\gamma)$	Belle [21]	$(4.01 \pm 0.21 \pm 0.17) \times 10^{-5}$	85
	BaBar [20]	$(4.47 \pm 0.10 \pm 0.16) \times 10^{-5}$	383
	Average [36]	$(4.33 \pm 0.15) \times 10^{-5}$	
$\mathcal{B}(B^+ \to K^{*+}\gamma)$	Belle [21]	$(4.25 \pm 0.31 \pm 0.24) \times 10^{-5}$	85
	BaBar [20]	$(4.22 \pm 0.14 \pm 0.16) \times 10^{-5}$	383
	Average [36]	$(4.21 \pm 0.18) \times 10^{-5}$	
$A_{CP}(B^0 \to K^{*0}\gamma)$	Belle [21]	$(-3.0 \pm 5.5 \pm 1.4) \times 10^{-2}$	85
	BaBar [20]	$(-1.6 \pm 2.2 \pm 0.7) \times 10^{-2}$	383
	LHCb [22]	$(0.8 \pm 1.7 \pm 0.9) \times 10^{-2}$	$^*1.0$ fb^{-1}
	Average [36]	$(-0.2 \pm 1.5) \times 10^{-5}$	
$A_{CP}(B^+ \to K^{*+}\gamma)$	Belle [21]	$(0.7 \pm 7.4 \pm 1.7) \times 10^{-2}$	85
	BaBar [20]	$(1.8 \pm 2.8 \pm 0.7) \times 10^{-2}$	383
	Average [36]	$(1.7 \pm 2.7) \times 10^{-2}$	
$A_{CP}(B \to K^*\gamma)$	Belle [21]	$(-1.5 \pm 4.4 \pm 1.2) \times 10^{-2}$	85
	BaBar [20]	$(-0.3 \pm 1.7 \pm 0.7) \times 10^{-2}$	383
	Average [36]	$(-0.5 \pm 2.0) \times 10^{-2}$	
$\Delta_{0-}(B \to K^*\gamma)$	Belle [21]	$(1.2 \pm 4.4 \pm 2.6) \times 10^{-2}$	85
	BaBar [20]	$(6.6 \pm 2.1 \pm 2.2) \times 10^{-2}$	383
	Average [36]	$(5.2 \pm 2.6) \times 10^{-2}$	

Table 2.4.2: The branching fractions, direct CP asymmetries and isospin asymmetries of $B \to K^*\gamma$. Number of $B\bar{B}$ pairs in the CP asymmetry of neutral B meson in LHCb is described as integrated luminosity.

$$\mathcal{A}(B \to K^*\gamma) = |\mathcal{A}_{\rm SM}(B \to K^*\gamma) + \mathcal{A}_{\rm NP}(B \to K^*\gamma)|^2,$$
$$\mathcal{A}(B \to K^*\gamma) = |A_{\rm SM}|^2 + |A_{\rm NP}|^2 + 2|A_{\rm SM}A_{\rm NP}|\cos(\theta_{\rm NP} + \delta_{\rm NP} - \delta_{\rm SM}).$$

Direct CP asymmetry is proportional to the difference between $\mathcal{A}(B \to K^*\gamma)$ and $\mathcal{A}(\overline{B} \to \overline{K}^*\gamma)$ therefore it is given as

$$\begin{aligned} A_{CP} &\propto |\mathcal{A}(B \to K^*\gamma)|^2 - |\mathcal{A}(\overline{B} \to \overline{K}^*\gamma)|^2 \\ &= -4|A_{\rm SM}A_{\rm NP}|\sin\theta_{\rm NP}\sin(\delta_{\rm SM} - \delta_{\rm NP}). \end{aligned}$$

The definition of the direct CP asymmetry is given as

$$A_{CP}(K^*\gamma) = \frac{\Gamma(\overline{B} \to \overline{K}^*\gamma) - \Gamma(B \to K^*\gamma)}{\Gamma(\overline{B} \to \overline{K}^*\gamma) + \Gamma(B \to K^*\gamma)} \quad (2.4.2.4)$$

where Γ is the partial decay width. The SM prediction is $|A_{CP}| < 1\%$ [17][18][19][23] therefore all of current results are consistent to the SM. According to the reference of [19][23], direct CP asymmetry in the decay of $B^0 \to K^{*0}\gamma$ is sensitive to the imaginary part of C_7, which can represented by

$$A_{CP}(B^0 \to K^{*0}) \sim [0.003 - 0.45{\rm Im}C_7(m_b)]\frac{\mathcal{B}(B^0 \to K^{*0}\gamma)_{\rm SM}}{\mathcal{B}(B^0 \to K^{*0}\gamma)} \quad (2.4.2.5)$$

here the energy scale of C_7 is the m_b. The constraint to imaginary part of C_7 using world average which is dominated by the LHCb result is $|\mathrm{Im}C_7(m_b)| < 0.16$ with 95% confidence level. Figure-2.4.1 shows the counter plot of imaginary and real component of C_7.

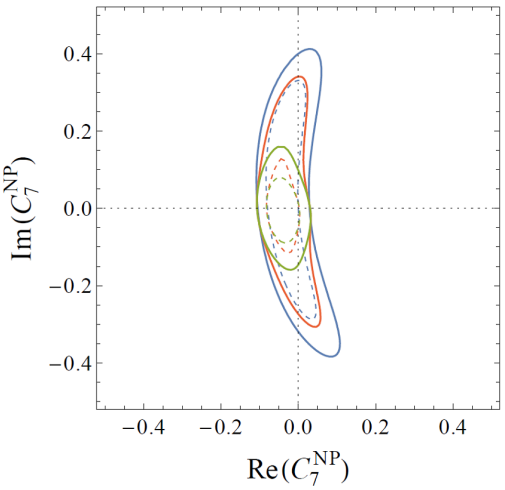

Figure 2.4.1: The contour plot of Re(C_7^{NP})-Im(C_7^{NP}). The blue dot and solid line show the 1 and 2 σ constraint without the result of $A_{CP}(B \to K^*\gamma)$. The red (green) line show the constraint including 50 (25)% theoretical uncertainty with including the result of $A_{CP}(B \to K^*\gamma)$. [23]

The isospin asymmetry is defined as

$$\begin{aligned} \Delta_{0-}(K^*\gamma) &= \frac{\Gamma(\overline{B}^0 \to \overline{K}^{*0}\gamma) - \Gamma(B^- \to K^{*-}\gamma)}{\Gamma(\overline{B}^0 \to \overline{K}^{*0}\gamma) + \Gamma(B^- \to K^{*-}\gamma)} \\ &= \frac{(\tau_{B^+}/\tau_{B^0})\mathcal{B}(\overline{B}^0 \to \overline{K}^{*0}\gamma) - \mathcal{B}(B^- \to K^{*-}\gamma)}{(\tau_{B^+}/\tau_{B^0})\mathcal{B}(\overline{B}^0 \to \overline{K}^{*0}\gamma) + \mathcal{B}(B^- \to K^{*-}\gamma)} \end{aligned} \tag{2.4.2.6}$$

where τ is the life time and $\mathcal{B}$ is the branching fraction. The SM prediction is $\Delta_{0-} = (5.8^{+4.5}_{-2.8}) \times 10^{-2}$ [17] and the large uncertainties are scale dependence and remaining form factor uncertainty. All of current results are consistent to the SM. The cause of the non-zero SM prediction of the isospin asymmetry is the existence of three miner contributions, radiation from spectator quark annihilation diagram and charmonium penguin diagram [24]. Former two contributions are main effects. In the spectator particle effect, the charge of spectator particles are difference in B^0 and B^+ with charge conjugate therefore the decay rates of emitting photon from them are not same. In the annihilation contribution case, the coupling of b and u which form B^+ exist in other hand that of b and d which form B^0 does not exist in the SM, so this difference arise non-zero isospin asymmetry. Figure-2.4.2 shows the Feynman diagrams of them.

The Supersymmetry (SUSY) have bean considered as one of the most important NP model. However, since there are a lot of free parameters in the SUSY model, we constrain the parameters with setting the range or fixing when considering the NP effect in the measurements [25][26]. In the SUSY mechanism, the theory which is the minimal Supersymmetry extended the SM is called as minimal Super-Gravity (mSUGRA) described by only five parameters, m_0 which is the mass of

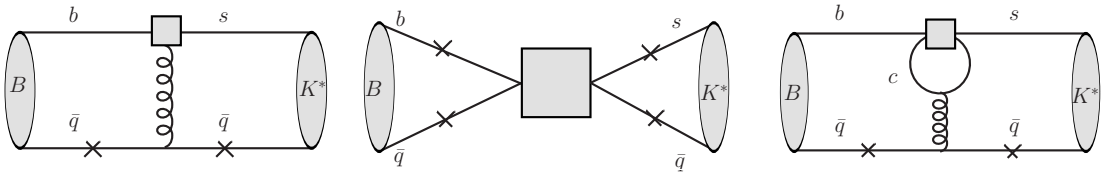

Figure 2.4.2: The Feynman diagrams which effect to non-zero isospin. Left, center and right diagram show the photon emission from spectator particle, annihilation contribution and charmonium penguin effect. The crosses in the diagrams are the point which can couple to photon. The gray box shows vertex of the quantum effect.

scalar particles at the supersymmetric grand unification scale, $m_{1/2}$ which is the universal gaugino mass, A_0 which is the universal trilinear SUSY breaking parameter, μ which is sine of the Higgs mixing parameter and the fraction of the two Higgs vacuum expection value $\tan\beta$. The isospin asymmetry of $B \to K^*\gamma$ have a relation to the mSUGRA parameter space in the context of minimal flavor violation.

When the effect of mSUGRA contributes to the SM, new operators do not have to be added in Eq-2.2.0.2 but we must modify the Wilson coefficients. The next-to-leading order calculation of Wilson coefficients expanded about strong coupling constant α_s whose energy scale is $\mu_W = \mathcal{O}(M_W)$ is represented by

$$C_i(\mu_W) = C_i^{SM}(\mu_W) + \delta C_i^{H^\pm}(\mu_W) + \delta C_i^{\chi}(\mu_W) + \delta C_i^{(SM,\tan\beta)}(\mu_W) + \delta C_i^{(H^\pm,\tan\beta)}(\mu_W), \quad (2.4.2.7)$$

where first, second and third terms are the SM W boson contribution, charged Higgs ($H^\pm$), charginos term (χ) contributions, and forth and fifth terms are the correlation term between $\tan\beta$ and W boson in the SM, and $\tan\beta$ and charged Higgs $H^\pm$. Figure-2.4.3 shows the theoretical calculation result for mSUGRA. From world average in Table-2.4.1, the 95% confidence level to $m_{1/2}$ and $\tan\beta$ are found in Fig2.4.3.

Furthermore, the difference of the direct CP asymmetries between charged and neutral B meson defined as

$$\Delta A_{CP} = A_{CP}^{B^-} - A_{CP}^{\overline{B}^0}, \quad (2.4.2.8)$$

where $A_{CP}^{B^-}$ and $A_{CP}^{\overline{B}^0}$ are the CP asymmetries of charged/neutral B decay are sensitive to new physics. ΔA_{CP} is zero exactly in the SM and new physics with CP violation of the SM [27]. The ΔA_{CP} of $B \to K^*\gamma$ have never been measured, therefore if we measure it, the first measurement can be reported.

The current situation for the measurements are summarized in Figure-2.4.4,2.4.5 and compared among experiments.

2.4.3 Time-dependent CP Asymmetry

Only left-handed particle or right-handed anti-particle are allowed to interact, so left-handed photon is mainly generated at radiative penguin decay in the SM, and right-handed photon emission is suppressed by $C_7' = \frac{m_s}{m_b} C_7$. However if the new particle which can couple to right-handed particle is contributed in the diagram such as Figure-2.1.1, the probability of the generation of right-handed

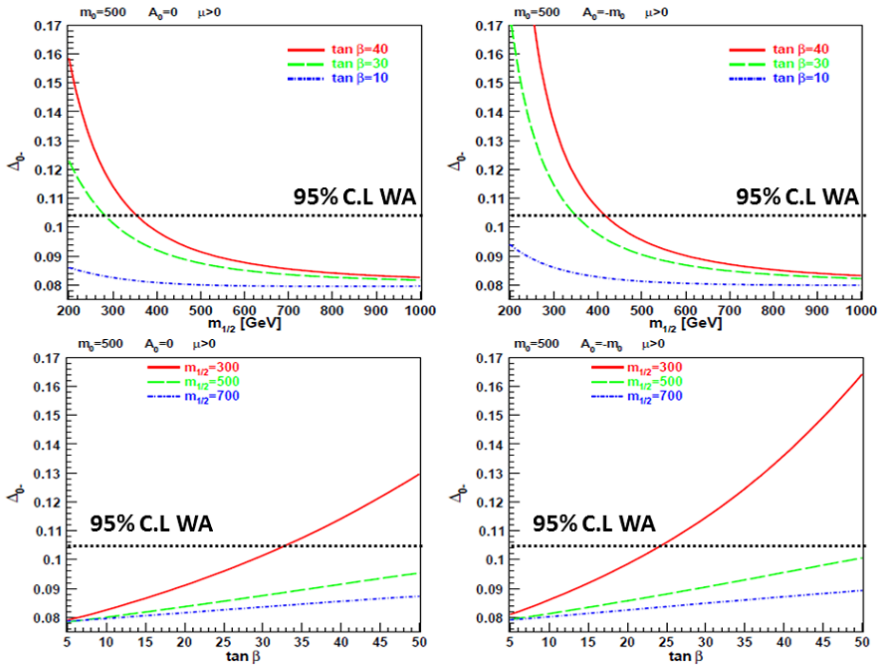

Figure 2.4.3: Isospin asymmetry vs $m_{1/2}$ and $\tan\beta$ for $A_0 = 0$ and $A_0 = -m_0$. WA means world average.

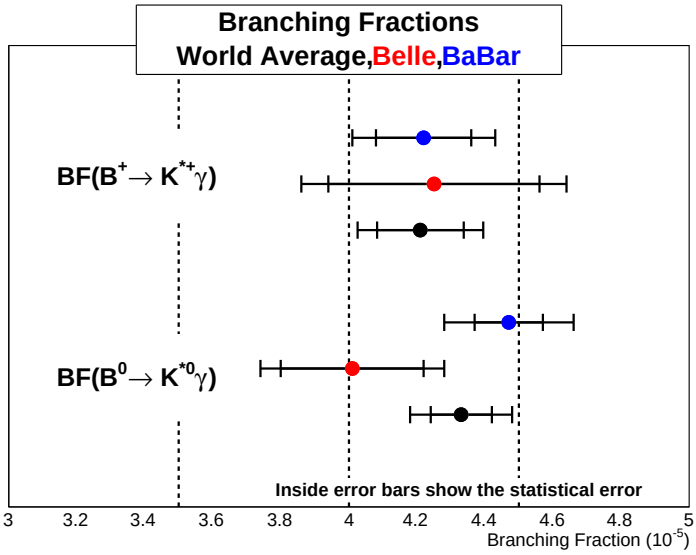

Figure 2.4.4: The plot of the result of the branching fraction each experiment. The black, red and blue points show world average and Belle and BaBar results. The internal error bars show only the statistical uncertainty and outer ones show the uncertainty combined statistical and systematic one.

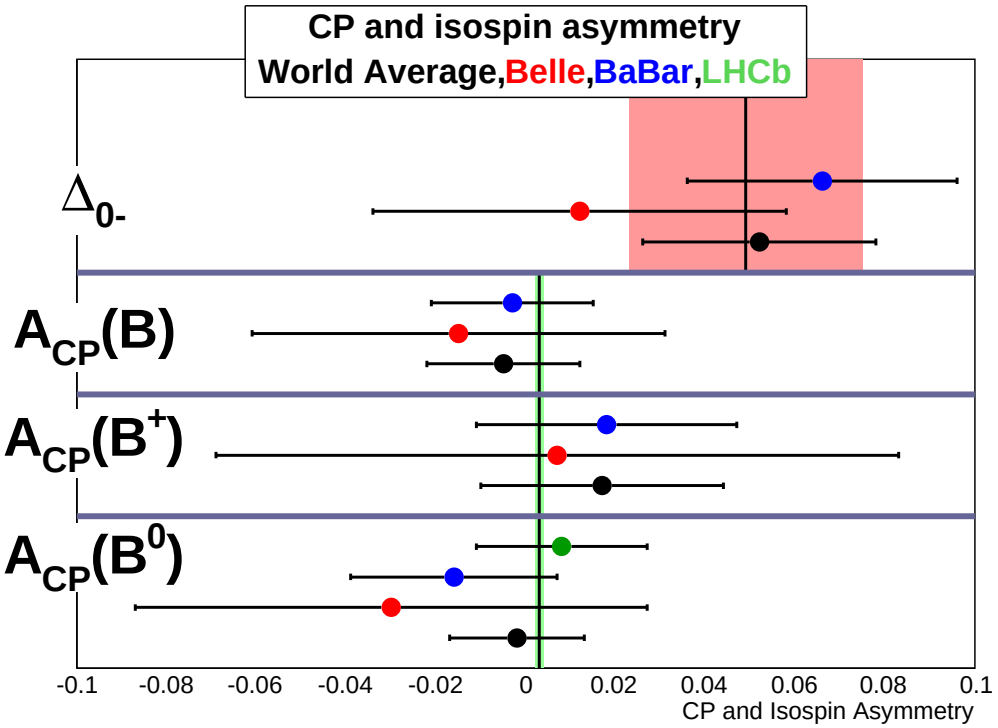

Figure 2.4.5: The plot of the result of the direct CP and isospin asymmetry, and ΔA_{CP} each experiment. The black, red, blue and green points show world average and Belle, BaBar and LHCb results.

photon is enhanced. The effect is not pensive to the branching fractions since one is sensitive to the absolute value such as $|C_7|^2+|C_7'|^2$. The time-dependent CP asymmetry can understand the effect of C_7'/C_7, so this measurement is useful. The expected mixing induced CP asymmetry parameter (S) is $\mathcal{O}(3\%)$.

To measure the time-dependent CP asymmetry, the vertex position of B meson must be decided by using two charged particles such as K_s and ρ. The most pensive decay modes to the NP is $B^0 \to K_s\pi^0\gamma$ which have large branching fractions and can perform the strong background suppression because this process is mainly generated through K^* resonance. The decay of $B \to K_s\rho\gamma$ also have good sensitivity because the branching fractions is not small and the decay vertex determination of B meson is performed by $\rho \to \pi\pi$ which decay immediately because of strong interaction.

The current measurements are visualized in Figure-2.4.6.

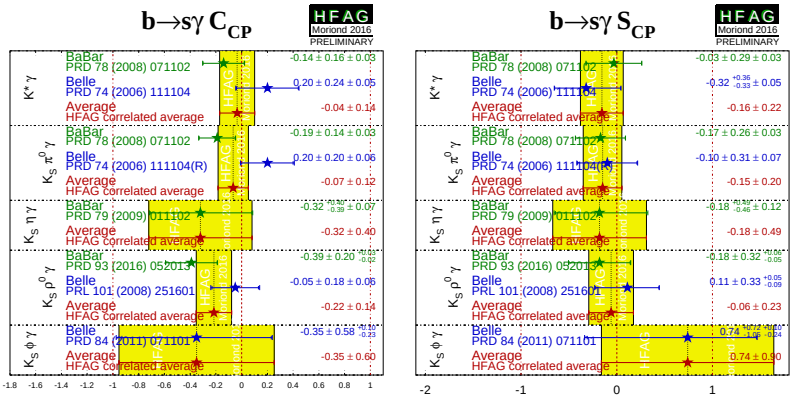

Figure 2.4.6: The status of the measurement of time-dependent CP violation in the decay of $b \to s\gamma$. The left figure shows the measurement status of the parameter "C" which means the direct CP violation. The right figure shows the measurement status of the parameter "S" which means the mixing-induced CP violation.

Chapter 3

KEKB Accelerator and Belle Detector

In this section, we describe the equipment of this analysis, the KEKB accelerator and the Belle detector which are located at at High Energy Accelerator Research Organizational (KEK) in Tsukuba, Japan.

3.1 KEKB Accelerator

The KEKB accelerator [28] provides a large quantity of $B\overline{B}$ pairs with the asymmetric e^+e^- collision. The tunnel including the accelerator was used in TRISTAN [29] which is the experiment with e^+e^- collision tuned at $\sqrt{s} = 64$ GeV and it is at ten meter underground. Figure-3.1.1 shows a layout of the KEKB accelerator. Electrons and positrons are accelerated in linear part of accelerator (Linac) up to collision energy, 8 and 3.5 GeV, and injected to storage rings whose perimeter is 3 km. The KEKB accelerator has two rings which storage electrons and positrons, respectively. The ring for storaging 8 GeV electrons is called as high energy ring (HER) and another ring for storaging 3.5 GeV positrons is called as low energy ring (LER). Two rings are crossed at one point which is placed the Belle detector with ± 11 mrad of crossing angle and this is called interaction point (IP). The presence of crossing angle is one of the features in the KEKB accelerator. This is a good idea to avoid a lot of background after collision.

The center-of-mass energy is set at

$$\sqrt{s} = 2\sqrt{E_{HER} \cdot E_{LER}} = 10.58 \text{ GeV}, \tag{3.1.0.1}$$

which is the threshold energy to generate $B\overline{B}$ pairs and corresponding to the mass of $\Upsilon(4S)$ resonance. This energy can be determined with 0.6 MeV uncertainty.

The major decay process of $\Upsilon(4S)$ is B^+B^- and $B^0\overline{B}^0$ and these are created with boost factor due to asymmetric collision. The magnitude of boost ($\beta\gamma$) is calculated as

$$\beta\gamma = \frac{E_{HER} - E_{LER}}{2\sqrt{E_{HER}E_{LER}}} = 0.425. \tag{3.1.0.2}$$

Due to this boost, time dependent CP asymmetry can be measured by measuring the difference of decay point in z-axis.

Amount of generated $B\overline{B}$ pairs are determined by the cross section and the luminosity. The cross sections at $\sqrt{s} = 10.58$ GeV are found in Table-3.1.1. The cross section of $e^+e^- \to b\bar{b}$ is

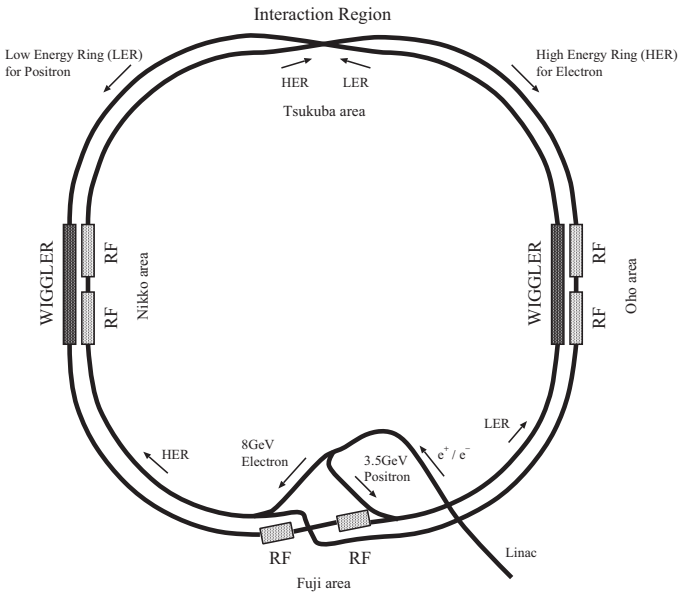

Figure 3.1.1: A layout of the KEKB accelerator [28]

1.1 nb and sum of cross section of $c\bar{c}$ and $q\bar{q}$ which is considered as major background candidates is three times larger.

Decay	cross section (nb)
$b\bar{b}$	1.1
$c\bar{c}$	1.3
$q\bar{q}$ $(q = u, d, s)$	2.1
$\tau^+\tau^-$	0.93
QED $(25.551° < \theta < 159.94°)$	37.8
$\gamma\gamma$	37.8

Table 3.1.1: The cross section table at $\sqrt{s} = 10.58$ GeV

Instantaneous luminosity is given as

$$\mathcal{L} = \frac{n_{e^-} n_{e^+} f}{4\pi\sigma_x\sigma_y}, \tag{3.1.0.3}$$

where n_{e^-} and n_{e^+} are number of electrons and positrons in a bunch which is the group of particles, f is the crossing frequency and σ_x and σ_y are uncertainty of beam size in horizontal and vertical axis. Design value of instantaneous luminosity is $10^{34}\mathrm{cm}^{-2}s^{-1}$ and this requirement is archived in 2004. Furthermore, maximum instantaneous luminosity,

$$\mathcal{L} = 2.11 \times 10^{34}\mathrm{cm}^{-2}\mathrm{s}^{-1},$$

is obtained in June 2009 and this is the current world record [30]. Due to some ideas, these records are attended. In the beginning of running the KEKB, the bunches of electrons and positrons

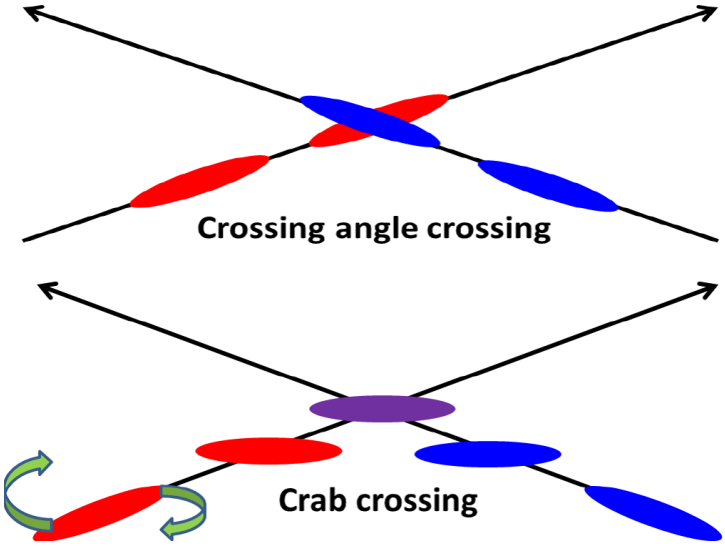

Figure 3.1.2: Illustration of collision without and with crab crossing

had been injected from linac to storage rings discretely. However the operation of contentious injection [30] was started in 2004 to reduce the dead time caused by previous method. Furthermore, to reduce the loss of the cross section by crossing angle, "crab crossing" method had been started from 2007. In this method, since bunches are rotated in horizontal direction, the head-on collision can be realized. Figure-3.1.2 show the illustration of crab crossing.

Finally, the KEKB accelerator was operated by June 2010. The total integrated luminosity is 1 ab^{-1} and that of around $\Upsilon(4S)$ resonance is 711 fb^{-1} which is the largest in the lepton colliders in the world [30]. Figure-3.1.3 shows integrated luminosity of B factories comparing the BaBar experiment.

3.2 Belle Detector

The Belle detector is the complex detector which consists of many sub-detectors, such as silicon vertex detector, gas tracker system, particle identification detectors, electromagnetic calorimeter and muon-hadron detector. Figure-3.2.1 shows the overview of the Belle detector. 1.5 T B-field is produced by superconducting solenoidal magnet for measuring the momenta of charged tracks. Acceptance, which is the range covering by the Belle detector, is $17° < \theta < 150°$.

Because particles which have short life time can not be detected directly such as B meson, they are reconstructed by $e^{\pm}$, proton, $\mu^{\pm}$, γ, $\pi^{\pm}$, $K^{\pm}$ and K^0_L which are mainly captured by the Belle detector. Decay vertex of B meson is measured by Silicon vertex detector (SVD, Section-3.2.1) which is placed outside of beam pipe. Charged particle momentum is measured by central drift chamber (CDC, Section-3.2.2) combined with SVD. CDC covers the full acceptance of the Belle detector. Identification of K and π is performed by dE/dx measured in CDC, hit information of the aerogel Cherenkov counter (ACC, Section-3.2.4) which is threshold type Cherenkov counters and time-of-flight (TOF, Section-3.2.3) counter information. ACC and TOF cover the end-cap and barrel region outside of CDC. Electromagnetic calorimeter (ECL, Section-3.2.5) is used for

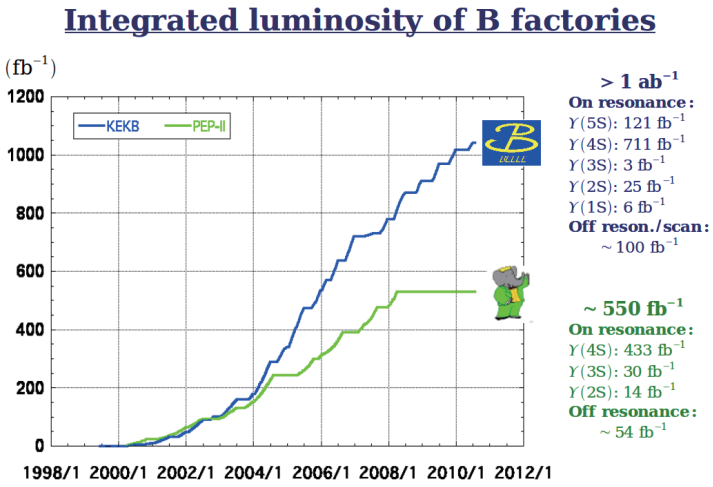

Figure 3.1.3: Integrated luminosity of B factory

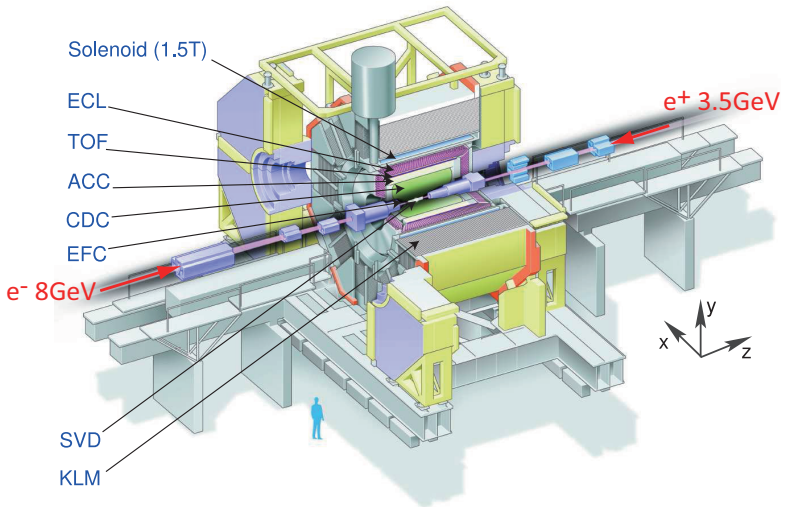

Figure 3.2.1: A overview of the Belle detector [31]

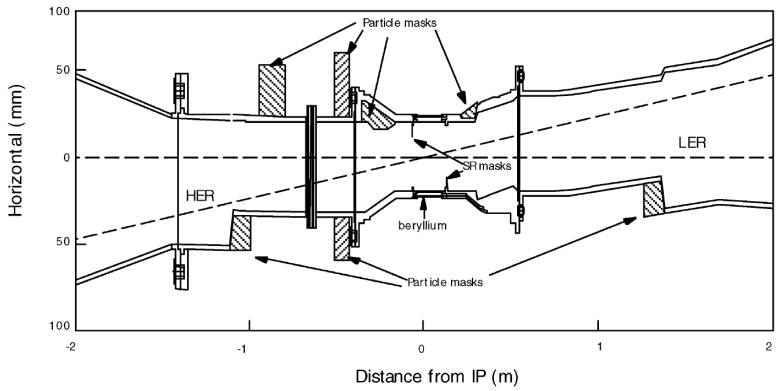

Figure 3.2.2: Figure of the interaction point. HER and LER mean "High Energy Ring" and "Low Energy Ring", electron and positron beam [31].

electron identification and photon detection. This is placed outside of ACC and TOF and inside of solenoid coil. K_L and muon detector (KLM, Section-3.2.6) is performed by resistive plate counter system placed at outermost detector.

To determine the decay vertex precisely is important in the Belle experiment. The thickness of beam pipe and closeness of SVD first layer to IP is effective for improving vertex resolution [31]. The beam pipe is made by beryllium. The central part ($-4.6 \leq z \leq 10.1$ cm) of beam pipe have double-wall beryllium cylinder with 4.0 cm of an inner diameter. There is a 2.5 mm gap between inner and outer walls and helium gas is filled for cooling in its gap. The thickness of inner and outer wall is 0.5 mm. Since thanks to thin beam pipe, multiple coulomb scattering can be reduced, the performance of vertex resolution in z-axis is not decreased.

In addition the beam pipe of the LER is constructed in parallel to B-field but that of the HER is constructed with 22 mrad angle against the LER for generating crossing angle because of reducing the effect from B-field in LER which is bent strongly comparing HER. Therefore the definition of the $z-$axis is opposite direction to positron beam direction. Figure-3.2.2 is the figure focus to interaction point.

3.2.1 Silicon Vertex Detector (SVD)

The precise vertex measurement is performed by the Silicon Vertex Detector (SVD) [31]. Owing to this, time-dependent CP-violation in the neutral B meson can be measured. In addition, SVD helps measuring to detect the vertexes of D and τ. By accumulating 140 fb^{-1}, three SVD layers had been set. We call the SVD equipment in this phase "SVD1". The covered range at SVD1 is $23^\circ < \theta < 139^\circ$, which full acceptance is not covered by but 86% of polar angle is covered. The radii of three layers are 3.0, 4.55 and 6.05 cm which are placed out of the beam pipe. For first, second and third layers, 8, 10, 14 ladders are set, respectively. In the summer of 2003, number of SVD layers was changed from 3 to 4 by the end of the Belle experiment, and we call the SVD equipment at this phase "SVD2". The covered range in SVD2 is $17^\circ < \theta < 150^\circ$, which can be covered with full acceptance, 92% of polar angle and this is corresponding to CDC acceptance. The radii of four layers are 2.00, 4.35, 7.00 and 8.80 cm. Since the thickness of beam pipe was got thin and its radius was close to IP, the inner most SVD layer is also closed to IP. For first, second, third and forth layers, 6, 12, 18, 18 ladders are set, respectively.

The major requirements for SVD are low mass and high radiation tolerance. Since the momenta of a lot of particles which is interesting in the Belle analysis are around 1 GeV/c, the multiple Coulomb scattering is the main source for reducing vertex resolution. To solve this, the support structures are made by low mass materials but ridit and high mass parts such as readout electronics are placed outside of the tracking volume for SVD1 and the acceptance for SVD2. For example, the support ribs for constructing ladders are made of boron nitride sandwiched by carbon-fiber reinforced plastic. The SVD is the closest sub-detector in the Belle detector to IP, so it is suffered from a lot of radiation dose. At the maximum designed luminosity and current operation of the KEKB, the expected radiation dose at the inner most detector is 30 krad/year due to beam background. Radiation doses of this level can cause the degrading the noise performance of the electronics and the inducing leakage currents but the VA1 [32][33] integrated circuit assigned to readout system of SVD has excellent noise performance ($200e^-$+$8e^-$/pF) and good radiation tolerance of 200 krad.

Double-sided silicon strip detectors (DSSD) [34] are used for SVD sensors and basically a depleted pn junction. By passing through the junction of a charged particle, electrons are excited from valence band into the conduction band creating electron-hole pairs. Signals generated corresponding to the currents made by these pairs in the p^+ and n^+ strips located no the surface of the DSSD. The $p^+(n^+)$ strips are aligned along the beam axis (transversely) therefore measure the azimuthal angle $\phi(z)$.

The impact parameter resolution depended on the momentum $\sigma_{r\phi}$ and σ_z measured using cosmic rays are shown in Figure-3.2.5. Obtained resolutions can be described as
for SVD1

$$\sigma_{r\phi} = 19.2 \oplus 54.0/p\beta\sin^{3/2}\theta \ \ (\mu\mathrm{m}), \tag{3.2.1.1}$$

$$\sigma_z = 21.9 \oplus 35.5/p\beta\sin^{5/2}\theta \ \ (\mu\mathrm{m}), \tag{3.2.1.2}$$

for SVD2

$$\sigma_{r\phi} = 42.2 \oplus 44.3/p\beta\sin^{3/2}\theta \ \ (\mu\mathrm{m}), \ \text{and} \tag{3.2.1.3}$$

$$\sigma_z = 27.8 \oplus 31.9/p\beta\sin^{5/2}\theta \ \ (\mu\mathrm{m}). \tag{3.2.1.4}$$

Impact parameter resolutions in both $r-\phi$ and z coordinates were improved by the SVD upgrade dramatically.

3.2.2 Central Drift Chamber (CDC)

Central Drift Chamber (CDC) [31] is installed in the Belle detector for measuring the momentum for charged particle from the curvature bent by 1.5 T B-field and providing the information of particle identification using dE/dx measurement. Figure-3.2.6 shows the CDC structure. The CDC has 50 cylindrical layers of anode wires, which consist of 32 axial- and 18 stereo-wire layers, and three cathode strip layers. In summer of 2003, the inner three layers have been replaced by two small-cell layers for chaining from SVD1 to SVD2. Axial wires are parallel to the z axis and stereo wires are slanted to the z axis to provide z position information. The total number of drift cell is 8400(8464) for SVD1 (SVD2).

Filled gases in chamber are helium (50%) and ethane (50%). In order to suppress the multiple Coulomb scattering, selected gases are low Z. A charge avalanche which is generated by a charged particle passing through the CDC filled ionized gases drifts to a sense wire with specific velocity. Because of this feature, the information of the energy deposit and distance from the sense wire can be obtained by measuring drift time and signal height. Figure-3.2.7 shows the measured transverse

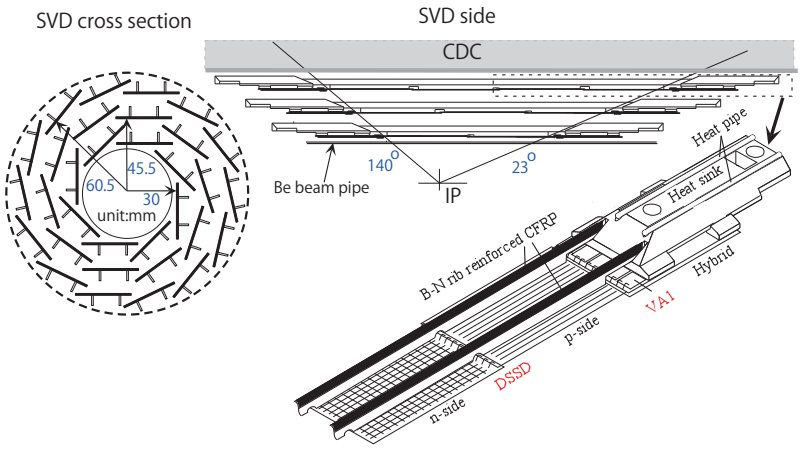

Figure 3.2.3: The geometry of SVD1 [31]

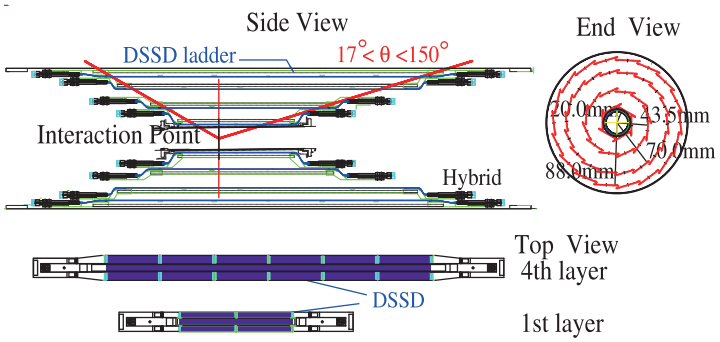

Figure 3.2.4: The geometry of SVD2 [31]

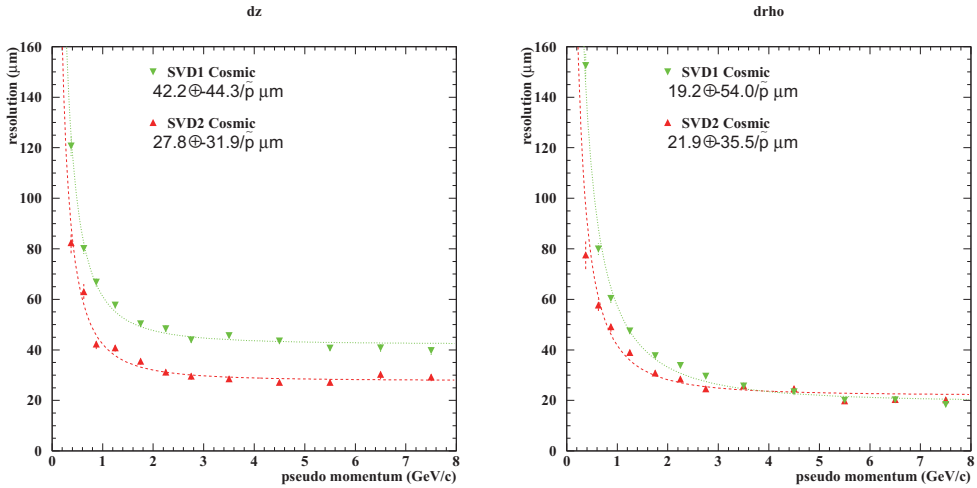

Figure 3.2.5: SVD performance measured by cosmic ray. $\tilde{p}$ shows the pseudo momentum defined as $\tilde{p} = p\beta \sin^{3/2}\theta$ and $\tilde{p} = p\beta \sin^{5/2}\theta$ in $r-\phi$ and z direction [31].

momentum resolution using cosmic ray (left side) and the scatter plot of measured dE/dx for each particle and its momentum (right side). Obtained transverse momentum resolution is

$$\frac{\sigma_{p_t}}{p_t}(\%) = 0.19\ p_t \oplus 0.30/\beta. \tag{3.2.2.1}$$

The resolution of dE/dx was measured to be 7.8% within $0.4 < p < 0.6$ GeV/c of momentum range. This measurement guarantees the K/π separation up to 0.8 GeV/c of momentum.

3.2.3 Time-of-Flight Counter (TOF)

The Time-of-Flight Counter (TOF) which is plastic scintillation counter provides the information for K/π identification below 1.2 GeV/c which is the momentum magnitude of detected track and fast timing signals used for the trigger, together with thin Trigger Scintillation counters (TSC). TSC is used for keeping the fast trigger rate below 70 kHz to avoid pile-up. The mass of particle (m) can be determined by

$$m = p\sqrt{\left(\frac{cT}{L}\right)^2 - 1} \tag{3.2.3.1}$$

where p is measured momentum at the CDC, T is measured time-of-flight at TOF and L is the length of the flight.

The TOF system consists of 128 TOF counters and 64 TSC. Two trapezoidally shaped TOF counters and one TSC counter form one module with a 1.5-cm intervening radial gap. Figure-3.2.8 shows the construction of TOF/TSC module. In total 64 TOF/TSC modules located at a radius of 1.2 m from the interaction point cover a polar angle range from 34° to 120° which is above 90% of barrel region. The minimum transverse momentum to reach the TOF counters is about 0.28 GeV/c.

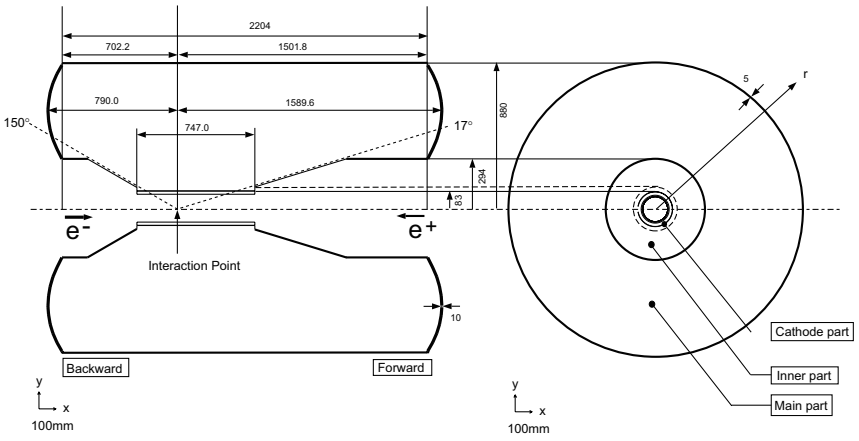

Figure 3.2.6: Overview of CDC structure [31]

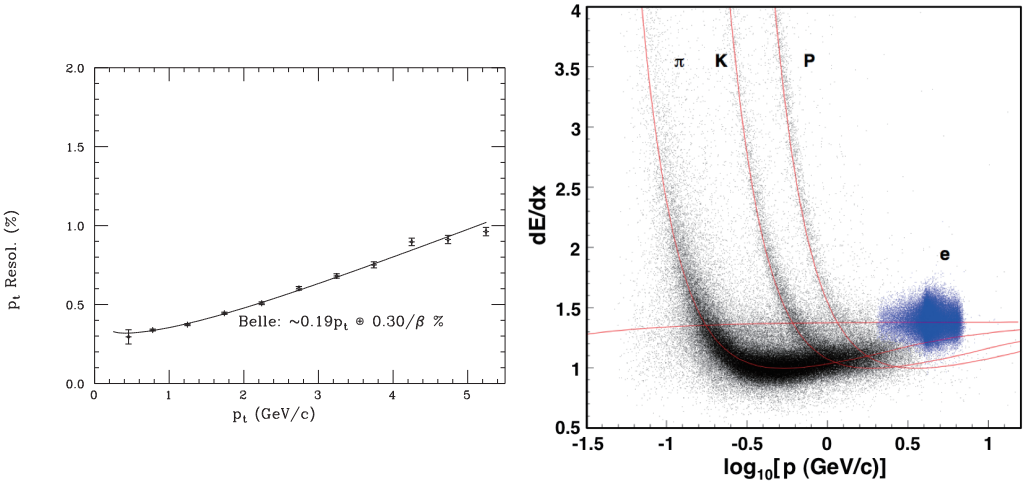

Figure 3.2.7: CDC performance figures. The transverse momentum resolution measured by CDC together with SVD (left) and the scatter plots of track momentum vs dE/dx (right figure) [31]

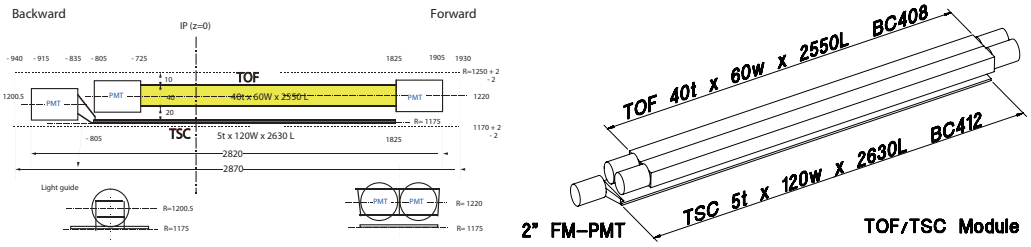

Figure 3.2.8: The construction of TOF/TSC module [31]

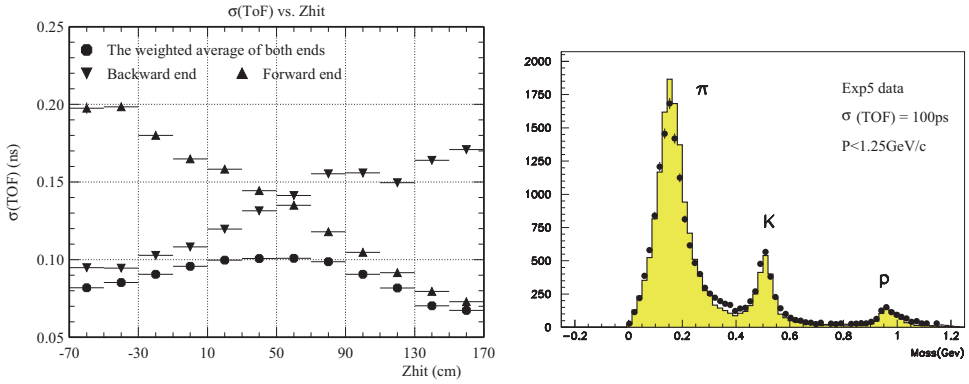

Figure 3.2.9: These two figures show the performance of TOF. Left figure shows the timing resolution for μ-pair events. Right figure shows the mass distribution from TOG measurements for particle momenta below 1.2 GeV/c. Histogram shows the exception assuming time resolution of 100 ps [31].

The readout of TOF counters at each end are performed by fine-mesh photomultiplire tubes (FM-PMT), with a 2-inch diameter and 24 stages of 2000 mesh/inch dynodes. The 24 dynode stages give a gain of 3×10^6 at a high voltage below 2800 V in a magnetic field of 1.5 T. The TSC readout is performed by FM-PMT at only backward end.

Figure-3.2.9 shows the timing resolution of hit position dependence in z-axis and mass distribution from TOF measurements below 1.2 GeV/c. The resolution for the weighted average time is about 100 ps with a small z dependence. Clear peaks corresponding to π, K and protons can be seen. The data points are obtained good agreement with a Monte Carlo prediction assuming timing resolution of 100 ps.

3.2.4 Aerogel Cherenkov Counter (ACC)

Aerogel Cherenkov Counter (ACC) [31] which provides the information of K/π identification in high-momentum range ($1.2 < p < 3.5$ GeV/c) is the threshold type Cherenkov Counter made by silica aerogel and covering end cap region. Since Cherenkov radiation is emitted when the particle passes through material medium in the ACC with speed above phase velocity of light in that medium. The Cherenkov light can be obtained if equation

$$n > \frac{1}{\beta} = \sqrt{1 + \left(\frac{m}{p}\right)^2}, \qquad (3.2.4.1)$$

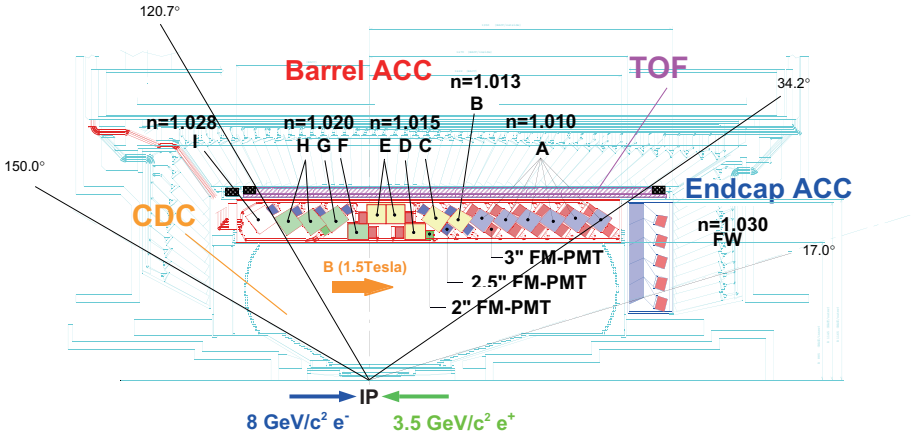

Figure 3.2.10: The geometry of ACC [31]

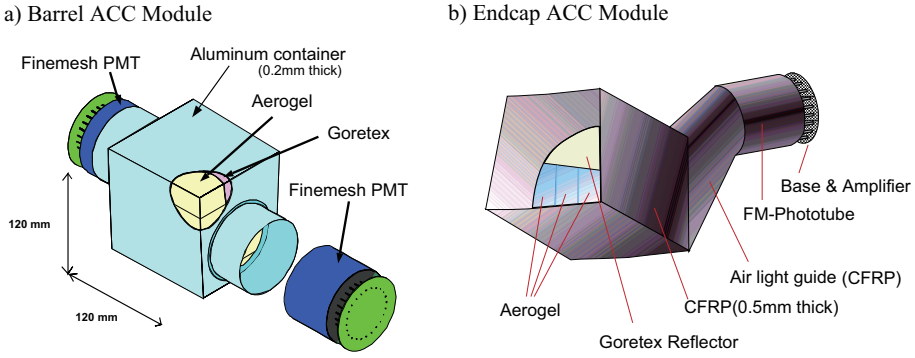

Figure 3.2.11: ACC module [31]

where n is is the refractive index of the matter and m and p are the mass and momentum of injection particle, is satisfied.

Figure-3.2.10 shows the geometry of ACC. The ACC is formed by 960 counter modules which are segmented into 60 cells in the ϕ direction for the barrel part and 228 modules which are placed in five concentric layers for the forward end-cap part of the detector [31]. All the modules are arranged in a semi-tower geometry, pointing to the interaction point. In order to obtain the good performance of $K\pi$ identification for the whole kinematical range, the range between 1.01 and 1.03 for the refractive indices of aerogels are assigned, depending on their polar angle region. A typical single ACC module is shown in Figure-3.2.11 for the barrel (a) and the end-cap (b) ACC, respectively. Five aerogel tiles are stacked in a thin (0.2 mm thick) aluminum box of approximate dimensions $12 \times 12 \times 12$ cm^3. In order to detect Cherenkov lights effectively, as same as TOF FM-PMT is used for readout.

The performance of ACC is checked using the decay of $D^{*-} \to \overline{D}^0\pi^-$, $\overline{D}^0 \to K^+\pi^-$. The π^- decayed from D^{*-}, so-called slow pion, allows to identify the daughter K and π from the $\overline{D}^0$ directly by their relative charges with respect to the slow pion. Figure-3.2.12 shows the distribution

of the number of photoelectrons, where the K/π separation is good and consistent with MC.

3.2.5 Electromagnetic Calorimeter (ECL)

Electromagnetic Calorimeter [31], ECL, which is made by CsI doped thallium, CsI(Tl), is constructed for measuring the energy and direction of photon and electron. Figure-3.2.13 shows the overview of ECL. When the particle injects to the ECL, almost of its energy is deposited in the ECL and transformed to scintillation lights. We can know the energy and direction of particles by measuring these lights.

The size of CsI(Tl) is determined whether all of energy of injection particle can be deposited. The event existing high energy photon like this study, $B \to K^*\gamma$, is typical topic for determination of CsI(Tl) size. This is determined by radiation length (X_0) and the Moliere radius (R_M) defined as

$$X_0 = \frac{716.4\ (\mathrm{g/cm^2})A}{Z(Z+1)\ln(287/\sqrt{Z})}, \tag{3.2.5.1}$$

$$E_c \sim \frac{800\ \mathrm{MeV}}{Z+1.2}, \tag{3.2.5.2}$$

$$R_M = 21.2\ \mathrm{MeV}\ \frac{X_0}{E_C}, \tag{3.2.5.3}$$

where A and Z are the atomic number and weight and E_C is the critical energy which is the value when ionization loss is same to radiation loss. The Moliere radius and radiation length of CsI(Tl) are 3.57 cm and 1.86 cm. In general, small Moliere radius material is favored because detector size can also be small. Designed CsI(Tl) crystal is that its length is 30 cm which is corresponding to 16 X_0, size of crystal nearer to IP side is 5.5×5.5 cm^2 which is corresponding to 1.5 R_M and that of opposite side is 6.5×6.5 cm^2. The readout system is performed by PIN photodiodes and a preamplifier mounted at the end of each crystal. The advantage of PIN photodiodes is that can be used in 1.5 T magnetic field and since the amount of light emission is large at CsI(Tl), the amplification factor is 1. ECL contains 8736 CsI(Tl) crystal counters. We constructed the ECL with three sections, forward end-cap section covering $12.4^\circ < \theta < 31.4^\circ$ including 1152 crystals, barrel section covering $32.2^\circ < \theta < 128.7^\circ$ including 6624 crystals and backward end-cap section covering $130.7^\circ < \theta < 155.1^\circ$ including 960 crystals.

The energy resolution is measured by a beam test as

$$\frac{\sigma_E}{E}(\%) = \frac{0.066}{E} \oplus \frac{0.81}{\sqrt[4]{E}} \oplus 1.34\ (E \ \text{ in GeV}) \tag{3.2.5.4}$$

where 1st term is the value affected by the electronic noise, 2nd terms describe the shower leakage fluctuation, and 3rd term shows the systematic effect such as the uncertainty of calibration. The spacial resolution is obtained as nearly 0.5 cm/$\sqrt{E}$.

3.2.6 Muon and K_L Detector (KLM)

To identify K_L and μ with high efficiency over a broad momentum range above 600 MeV/c, K_L and Muon Detector (KLM) [31] is constructed.

The KLM structure is successive layers of charged particle detector (resistive plate counters, RPC) and iron plates (4.7 cm thick). The neutral K_L meson makes a hadronic shower by strong interaction in the iron. For this shower we can measure the position detection, however, no useful measurement of its energy is possible because of the fluctuations of this shower. The energy deposit

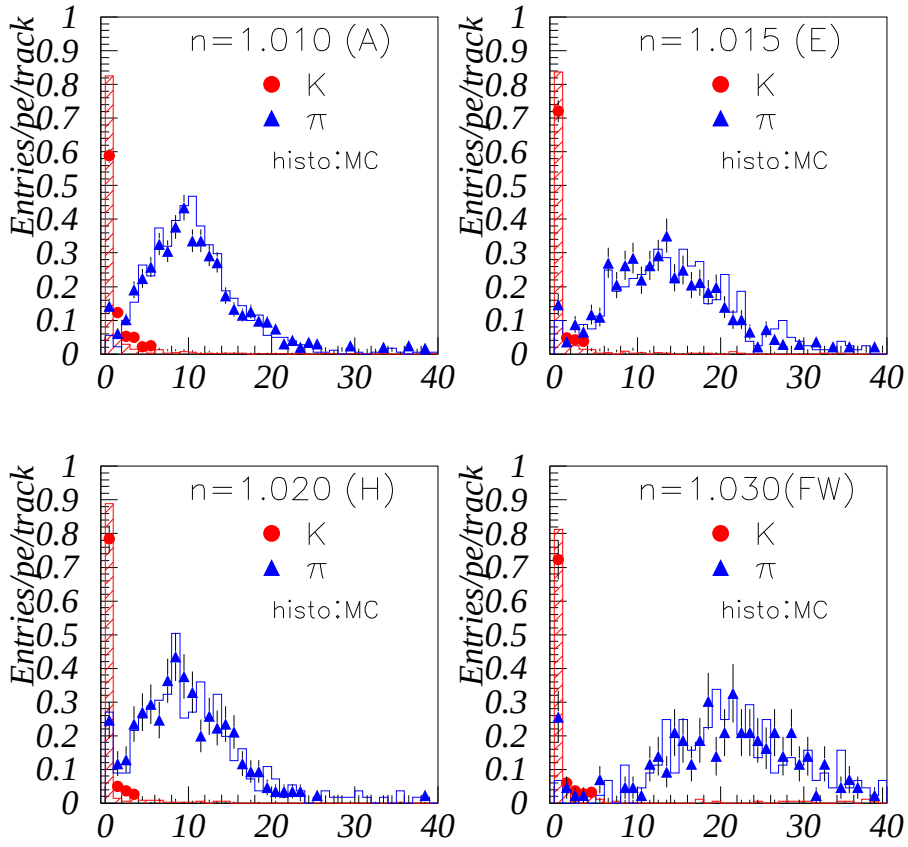

Figure 3.2.12: Performance of ACC [31]

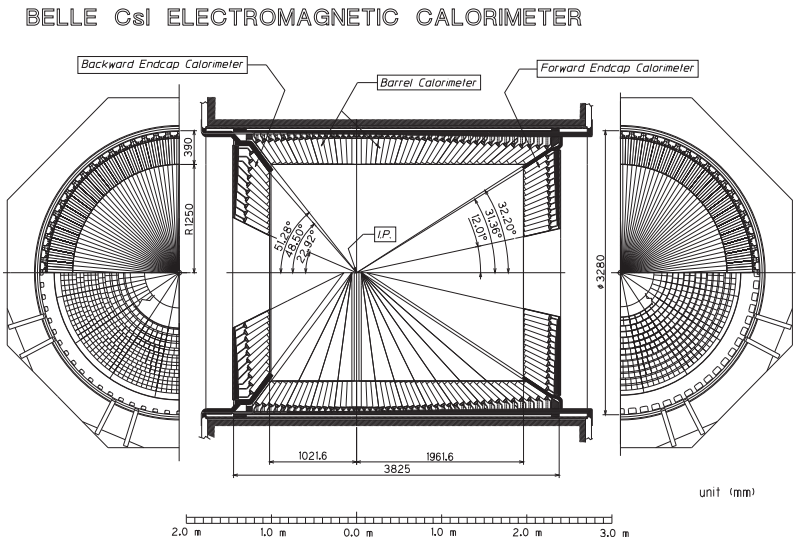

Figure 3.2.13: ECL geometry [31]

of the muon in the Belle detector except the KLM is much smaller than electrons and hadronic shower is not occurred because of its mass and feature of interaction. Muons can be measured using RPC which is explained following sentence. Other particles, such as pions and kaons are stopped in the system and can easily be separated from muons.

The KLM is formed by 15 detector layers and 14 iron layers in the barrel part ($45^\circ < \theta < 125^\circ$), and 14 detector layer in each of the forward and backward end-caps region ($20^\circ < \theta < 150^\circ$). The iron plates have 3.9 interaction length of material, in addition to 0.8 interaction length of ECL. The iron layers is also worked as a return yoke which is the superconducting solenoid and provides 1.5 T of the magnetic field. The KLM layers are grouped in superlayers, as shown in Figure-3.2.14. A superlayer is made of θ and ϕ cathode strips surrounding two RPCs. RPCs have two parallel-plate electrodes separated by a gas-filled gap. An ionizing particle traveling the gap initiates a streamer in the gas that results in a local discharge. This discharge creates a signal on the external cathode strips which can be used to record the location and time of the ionization. The number of KL clusters per event is in good agreement with the prediction. Typical muon identification efficiency is 90% with a fake rate around 2%.

3.2.7 Trigger and DAQ System

Trigger and data acquisition (DAQ) system is one of the important parts in the Belle experiment which is high luminosity operation collider [31]. Since there are a lot of events which are not interesting as physics topic such as e^+e^- scattering which is so-called Bhabha scattering, beam-gas interaction in the beam pipe, cosmic rays, etc., these event have to be rejected using high efficiency trigger. Furthermore in order to operate under high collision rate, DAQ system which can be performed high speed readout is needed.

Table-3.2.1 shows the trigger rate for each process at designed luminosity operation. There are two types of tringger in the Belle trigger system, a hardware trigger and a software trigger. An overview of the hardware trigger system is shown in Figure-3.2.15. The hardware trigger is formed by the sub-detector trigger systems and the central trigger system called the Global

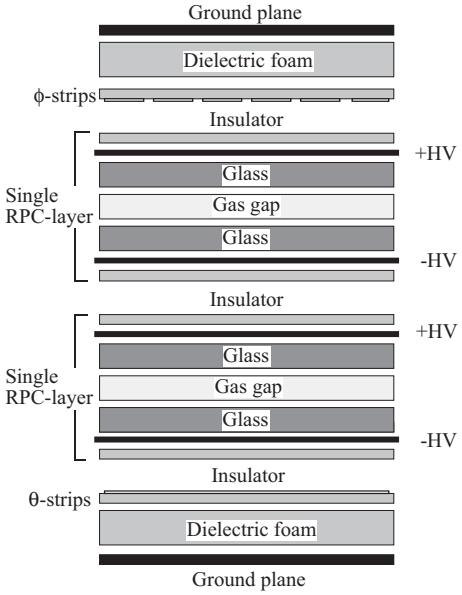

Figure 3.2.14: Overview of KLM [31]

Decision Logic (GDL). The GDL receives sub-detector triggers within 1.85 μs after the collision and issues a decision within 2.2 μs after the collision. There are two type of triggers in the sub-detector trigger systems, track triggers and energy triggers. The CDC and the TOF are used to yield trigger signals for charged particles. The ECL trigger system provides triggers based on total energy deposit and cluster counting of crystal hits. These two categories allow sufficient redundancy. Additional information for the muons are given by the KLM trigger and two photon and Bhabha events are decided by the ECL triggers. When the hardware trigger is issued, the Data Acquisition system (DAQ) collects signal data from sub-detectors and them on the data storage system. Fig.-3.2.16 shows the overview of the DAQ system. The entire system is segmented into seven subsystems running in parallel, each handling the data from a sub-detector. The received signals come from the sub-detectors except KLM pass a charge-to-time (Q-to-T) converter and are processed by a time-to-digital converter (TDC). For the SVD, DSSDs are read out by on-board chips and passed to flash analog-to-digital converters (FADC). The readout sequence starts when the sequence controller (SEQ) receives a final trigger from the GDL and distributes a common stop signal to the TDCs. The event builder converts detector-by-detector parallel data streams to an event-by-event data river and sent the data to an online computer farm.

Process	Rate (Hz)
$\Upsilon \to B\bar{B}$	12
$e^+e^- \to qq$ $(q = u, d, s, c)$	28
$e^+e^- \to \ell^+\ell^-$ $(\ell = \mu, \tau)$	16
Bhabha $(\theta_{lab} > 17^\circ)$	4.4
$\gamma\gamma$ $(\theta_{lab} > 17^\circ)$	2.4
two-photon process $(\theta_{lab} > 17^\circ)$	35
Total	86

Table 3.2.1: Trigger rate for each process [31]

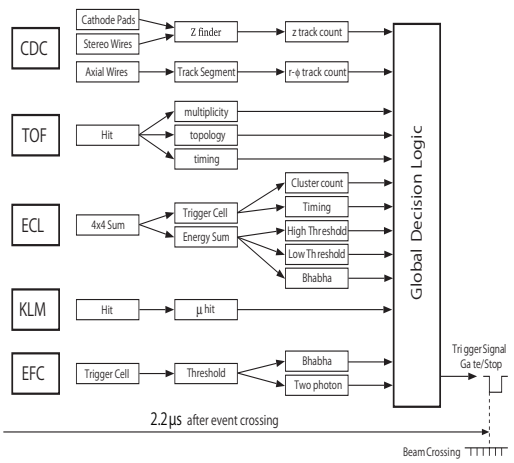

Figure 3.2.15: Overview of the trigger [31]

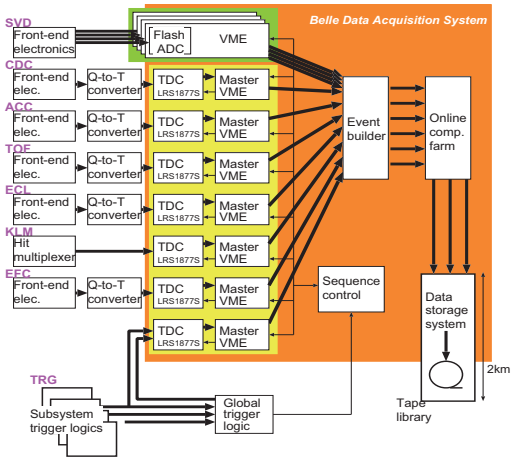

Figure 3.2.16: Overview of the DAQ system [31]

Chapter 4

Monte Carlo Simulation and Analysis Tool in Belle

We introduce the Monte Carlo simulation setup condition and a tool for analysis.

4.1 Monte Carlo Simulation Condition

To estimate the reconstruction efficiency and amount of major background contributions, we check the performance of this analysis with Monte Carlo (MC) simulation. In this analysis, blind analysis method is adopted, which means that the analysis using the real data is performed after finishing the estimation of sensitivity completely by MC sample. The signal, $B \to K^*\gamma$, MC sample is generated by event generation tool EVTGEN [35] which is suitable to B physics because this tool covers many physics cases such as CP-violating decays and angular analysis. In this analysis case, $K\pi$ invariant mass distribution is calculated using P-wave Breit-Wigner distribution, which is the improvements from previous tool "qq98". Detector simulation and digitization are performed by "gsim" which is standard Belle analysis tool which describes the Belle detector response. Assuming number of $B\overline{B}$ pair is 771.581 $\times 10^6$ which is same as all of amount of $B\overline{B}$ Belle experiment has, and since considering the branching fraction of $\Upsilon(4S)$, the number of $B^0\overline{B}^0$ and B^+B^- are scaled by 0.486 and 0.514. The method for counting BB pairs are written in Section-8.1. Assigned branching fraction is same as latest PDG (2016) value [36] $\mathcal{B}(B^0 \to K^{*0}\gamma) = 4.33 \times 10^{-5}$ and $\mathcal{B}(B^+ \to K^{*+}\gamma) = 4.21 \times 10^{-5}$. In this study, 200 streams of signal MC sample are generated where the stream is corresponding to the number of Belle experiments.

We divided the type of background sample into six. Expected main background source is continuum events such as $e^+e^- \to q\overline{q}$, here "q" means the quark which is lighter than bottom quark, i.e. $q = u, d, c, s$. The cross section of $e^+e^- \to q\overline{q}$ is three times larger than $e^+e^- \to \Upsilon(4S)$. We use six streams of MC data set and four streams of them are for analysis and the other two streams are used for the training sample for continuum suppression. The detail is written in section-6.1. In this paper, we call this type of background "qq bkg".

General B meson decay, $b \to cW^-$, is estimated by six streams of MC data. Since the signal has high energy photon, we expect the contribution from this background is small. In this paper we call this type of background "BB bkg".

Non-radiative peaking background candidates such as $B \to K^*\eta, B \to K^*\pi^0$ is estimated by 50 streams of MC data set. The branching fractions of these decay channels are not so large but these can make peaking background in the distribution. In this paper we call this type of background

"rare$B$ bkg".

Radiative peaking background candidates such as $B \to K_2^*(1430)\gamma$ and non-resonant $B \to K\pi\gamma$ are estimated by MC sample based on Kagan-Neubert model [37] and there are 40 streams data set. The lower mass limit of X_s is 1.15 GeV/c^2 and the signal $B \to K^*(892)\gamma$ is not included in this sample. Since for this lower mass limit, the amount of $X_s\gamma$ can be underestimated, the samples which include the decay of $B \to K\pi\pi\gamma$ are generated and replaced to those of MC samples. The latest study of $B \to K\pi\pi\gamma$ decay is performed by BaBar [38]. In this BaBar's study, the branching fractions of $B^+ \to K^+\pi^+\pi^-\gamma$ through five type of the resonances which have a strangeness, $K_1^+(1270)$, $K_1^+(1400)$, $K^{*+}(1410)$, $K_2^{*+}(1430)$ and $K^{*+}(1680)$, and these are listed in Table-4.1.1. Neutral B decay modes are not measured, so we generate the samples with same branching fractions as charged B decay modes assuming isospin symmetry. In this paper we call this type of background "$X_s\gamma$ bkg".

Decay Mode	$\mathcal{B}(B^+ \to K_{res}^+\gamma)\times$ $\mathcal{B}(K_{res}^+ \to K^+\pi^+\pi^-) \times 10^{-6}$	$\mathcal{B}(B^+ \to K_{res}^+\gamma) \times 10^{-6}$
$B \to K_1(1270)\gamma$	$14.5^{+2.1+1.2}_{-1.4-1.2}$	$44.1^{+6.3+3.6}_{-4.4-3.6}\pm$ 4.6
$B \to K_1(1400)\gamma$	$4.1^{+1.9+1.2}_{-1.2-1.0}$	$9.7^{+4.6+2.8}_{-2.9-2.3}\pm$0.6
$B \to K^*(1410)\gamma$	$11.0^{+2.2+2.1}_{-2.0-1.1}$	$27.1^{+5.4+5.2}_{-4.8-2.6}\pm$2.7
$B \to K_2^*(1430)\gamma$	$1.2^{+1.0+1.2}_{-0.7-1.5}$	$8.7^{7.0+8.7}_{-5.3-10.4}\pm$0.4
$B \to K^*(1680)\gamma$	$15.9^{+2.2+3.2}_{-1.9-2.4}$	$66.7^{+9.3+13.3}_{-7.8-10.0}\pm$ 5.4

Table 4.1.1: The Branching fractions of the decay modes of $B \to K\pi\pi\gamma$. The mean of K_{res} is the name of Kaon resonance.

We also consider the two type of background from $B \to K^*\gamma$, combinatorial background and cross-feeds. Combinatorial background is the B candidate which is incorrect combination. Cross-feeds is the interference between neutral and charged $B \to K^*\gamma$.

4.2 Particle Identification for $K^\pm/\pi^\pm$

Particle identification for $K^\pm$ and $\pi^\pm$ is performed based on the information obtained from sub-detectors, dE/dx given by the CDC, the Cherenkov light given by the ACC and time-of-flight measured in the TOF.

Figure-4.2.1 shows the momentum dependence of K/π separation performance for each sub-detectors and K/π separation performed with 3 σ confidence below 3.5 σ. The likelihood for K and π and likelihood ratio $\mathcal{LR}_{K/\pi}$ can be defined as

$$\mathcal{L}_i = \mathcal{L}_i^{dE/dx} + \mathcal{L}_i^{ACC} + \mathcal{L}_i^{TOF}, \quad (4.2.0.1)$$

$$\mathcal{LR}_{K/\pi} = \frac{\mathcal{L}_K}{\mathcal{L}_K + \mathcal{L}_\pi}. \quad (4.2.0.2)$$

where i means the particles, K or π.

The performance for K/π determination is checked using the decay of $D^{*+} \to D^0\pi^+$, $D^0 \to K^-\pi^+$. This channel can realize the study with good S/N ratio without $K\pi$ identification requirement. Therefore the detector performance can be directly probed with the daughter K and π mesons decayed from D meson, which can be tagged by their relative charged with respect to the

slow pion. With $\mathcal{LR}_{K/\pi} > 0.6$, the average of kaon efficiency and fake rate of π for the momentum range of $0.5 < p < 4.0$ GeV/c are about 88% and 8.5%.

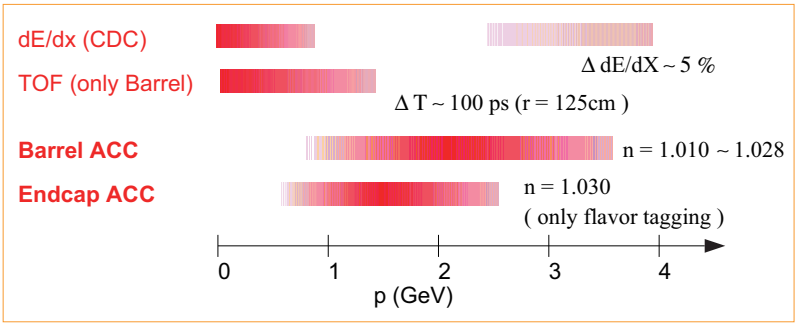

Figure 4.2.1: Momentum dependent $K\pi$ separation power for each sub-detectors

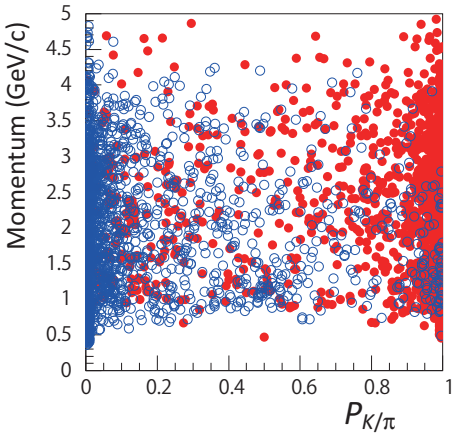

Figure 4.2.2: Likelihood Ratio vs momenta for daughter tracks from the decay of $D^0 \to K^-\pi^+$, tagged by the charge of the slow π^+'s. The closed red circles correspond to kaons and the open blue circles to pions.

Chapter 5

Reconstruction

The signal, $B \to K^*\gamma$ has four decaying channels, $B^0 \to K_s\pi^0\gamma, K^+\pi^-\gamma$ and $B^+ \to K_s\pi^+\gamma, K^+\pi^0\gamma$ with charge conjugate then we have to reconstruct $\gamma, K^\pm, \pi^\pm, K_s, \pi^0$, respectively. Selection criteria are decided based on detector performance and by maximizing the significance given as

$$\text{Significance} = \frac{N_{sig}}{\sqrt{N_{sig} + N_{bkg}}}, \tag{5.0.0.1}$$

where N_{sig} and N_{bkg} are the number of signal and all of background events.

5.1 Prompt Photon Selection

Prompt photon is characteristic evidence of the decay of $b \to s\gamma$. Since we can regard the decay of $b \to s\gamma$ as two body decay, the isolated cluster which has the energy around 2.2 GeV, half of bottom quark mass, of deposit energy in the ECL is prompt photon candidate. The energy range of photon candidates are determined by the amount of low energy photon backgrounds and the fit region of $K\pi$ invariant mass. In general, the relation between the mass of X_s (M_{X_s}) and the energy of photon (E_γ) is represented by

$$E_\gamma^{c.m.s} = \frac{m_B^2 - m_{X_s}^2}{2m_B}, \tag{5.1.0.2}$$

where m_B is the mass of B meson. Since the mass of K^{*0} is 0.89581 GeV/c^2, the nominal E_γ is 2.564 GeV. Considering the low energy photon background contributions and energy leakage of ECL, we decided $1.8 < E_\gamma^{c.m.s} < 3.4$ GeV. To remove the backgrounds from charged particles, isolated clusters are required. For the requirements, we defined "E9/E25" which is the ratio of "E9" which is the total energy of 3×3 CsI(Tl) crystal cells around the cell detected maximum energy in 9 cells and "E25" is same as "E9" and only switched from 9 to 25, 5×5. Figure-5.1.1 shows the rough picture to explain the E9E25 definition. If "E9/E25" is close to 1, the shower shape is sharp then we required the photon candidates whose "E9/E25" is greater than 0.95. To reduce the systematic uncertainty, photon candidates detected in the end cap region are rejected. High energy initial state radiations can be suppressed by this selection. We require that the angle of photon candidate against beam axis ($\theta_\gamma^{lab.}$), polar angle, is from 33 to 128 degree.

When the high momentum π^0 and η decay into two photons with asymmetric energies, photons which have higher energy can be background of prompt photon. To suppress them, we combine

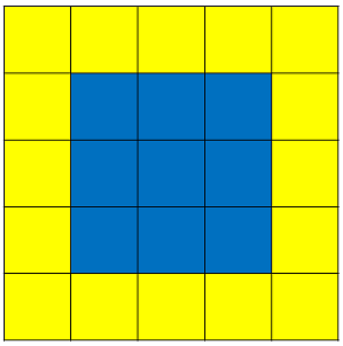

Figure 5.1.1: Rough picture for explanation of "E9/E25". E9 is corresponding to the total detected energy of blue region, 9 cells. E25 is corresponding to the total detected energy of blue and yellow regions, 25 cells.

the prompt photon candidate (γ_p) and other photon candidate (γ_o) and their π^0 and η likeness are evaluated by likelihood ratio based on invariant mass of two photons and energy of γ_o [39]. We require both of π^0 and η probability less than 0.3. Figure-5.5.1 show the distributions of photon energy, E9/E25, photon polar angle, and π^0 and η veto performance.

5.2 Charged Particles Selection, $K^{\pm}$ and $\pi^{\pm}$

All of charged track candidates are reconstructed by CDC and SVD, and their transverse momenta at the closest point to the origin in the x-y plane are calculated by extrapolating the tracks and obtaining the curvature of the tracks. The requirements for charged tracks to reconstruct the signal is written in following. Since the signal events should decay near the interaction point(IP), using impact parameter in x-y plane (dr) and z direction (dz) we require that the tracks are generated near IP. Here $|dr|$ <0.5 cm and $|dz|$ <5.0 cm are required. Figure-5.5.2 show the distributions of dr and dz of K and π, respectively. To reduce the contribution of low momentum charged particles, grater than 0.10 GeV/c of the track momentum is required. K/π decision is based on the likelihood ratio value ($\mathcal{LR}_{K/\pi}$) defined in section-4.2. We require $\mathcal{LR}_{K/\pi}$ for kaon candidate is grater than 0.6 and for pion candidate is less than 0.9. Figure-5.5.3 show the distributions of K and π identification.

5.3 K_s Selection

We use only the decay of $K_s \to \pi^+\pi^-$ for this analysis because it is hard to reconstruct the decay of $K_s \to \pi^0\pi^0$ and there are large systematic uncertainty.

K_s candidates are reconstructed by combining two charged pions with "vertex fit" [40]. Vertex fit is the method of recalculating the K_s momentum using new vertex which is the closest point between two charged tracks and treated as K_s vertex. This is one of the techniques to improve mass resolution. Figure-5.3.1 shows the powerfulness of vertex fit using the K_s mass resolution. Required invariant mass of K_s candidate is within 0.010 GeV/c^2 of nominal K_s mass (=0.497648 GeV/c^2). K_s mass distribution is shown in left side of Figure-5.5.4. To select good quality K_s candidate, we use "nisK_s" finder [41] which is the latest K_s selection tool based on Neurobayes technique [42] in the Belle experiment. Neurobayes provide high quality multivariate analysis. In nisK_s we define

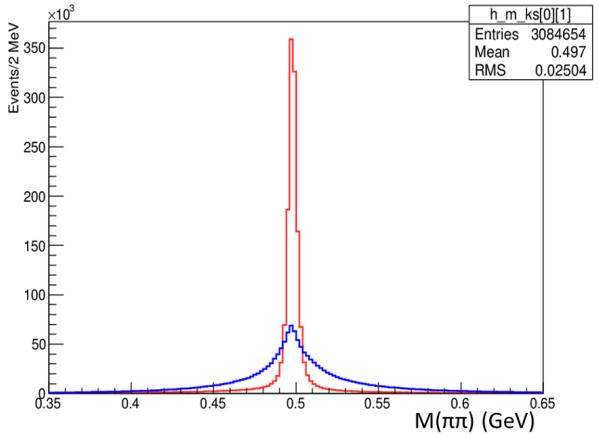

Figure 5.3.1: K_s mass distribution with(red)/without(blue) vertex fit

the two types of probabilities. One is V-particle probability, the other is $non-\Lambda$ probability. V-particle is the name of the particle decaying into two charged tracks such as K_s and Λ. A lot of background can be rejected by the mass selection and V-particle requirement however Λ which is the main background can be included in K_s candidates when occurring the wrong particle identification between π and proton. As a result we select K_s candidates using two probabilities. The training parameters for V-particle probability are

- the momentum of K_s candidate in laboratory frame,
- distance between two helices in z direction,
- the distance between interaction point and the decay vertex of K_s candidate in x-y frame,
- angle between K_s momentum and IP direction,
- shorter distance between interaction point and daughter helix,
- longer distance between interaction point and daughter helix,
- angle between K_s momentum (laboratory frame) and π momentum (K_s rest frame),
- SVD hit,
- CDC hit

and for $non-\Lambda$ probability are

- binned particle identification likelihood between π and proton, $(\mathcal{L}_\pi/(\mathcal{L}_\pi+\mathcal{L}_p))$,
- reconstructed mass with lambda hypothesis which means lorentz vector of one π is recalculated as proton,
- momentum of K_s daughter,
- sine of azimuth angle of K_s daughter.

Selection cut by which K_s can be extracted with 94.0% of purity and 86.9% of efficiency is applied.

5.4 π^0 Selection

π^0 candidates are reconstructed by combining the two photon candidates detected in ECL. Required invariant mass of two photons is within 0.010 GeV/c^2 around nominal π^0 mass (=0.13497 GeV/c^2). π^0 mass distribution is shown in right side of Figure-5.5.5. The requirement of the momentum with π^0 mass constraint in center-of-mass system is grater than 0.50 GeV/c. To reduce low energy photon background, we required energies in laboratory system of both of two photons are grater then 0.050 GeV. Since a lot of π^0 candidates are boosted, the angle between two photons ($\theta_{\gamma\gamma}$) should be close to 0. We required that $\cos\theta_{\gamma\gamma}$ is grater than 0.50. Figure-5.5.5 show the π^0 momentum and $\cos\theta_{\gamma\gamma}$ distributions.

5.5 Reconstruction of B meson

K^* candidates are reconstructed by combining K and π. We require the upper limit of invariant mass of $K\pi$ ($M(K\pi)$) is 2.0 GeV/c^2. This high upper limit come from M($K\pi$) fitting for estimating the amount of backgrounds from higher resonance. Fitting method and its result are described in Section-8.7. B meson candidates are reconstructed by combining prompt photon candidates and K^* candidates. Two kinematic variables, the beam energy constrained mass ($M_{\rm bc}$) and the energy difference (ΔE) are defined in Eq-(5.5.0.3), -(5.5.0.4) and calculated in center-of-mass frame.

$$M_{\rm bc} = \sqrt{(E^{c.m.s}_{beam}/c^2)^2 - |\vec{p}^{\,c.m.s}_B/c|^2} \tag{5.5.0.3}$$

$$\Delta E = E^{c.m.s}_B - E^{c.m.s}_{beam} \tag{5.5.0.4}$$

where $E^{c.m.s}_{beam}$ is the half of center-of-mass energy, $\vec{p}^{\,c.m.s}_B$ and $E^{c.m.s}_B$ are the momentum and energy of the reconstructed B meson candidate in the center-of-mass frame. To improve the momentum resolution of B meson, one is calculated without prompt photon energy and defined using momentum of $K\pi$ system in Eq-(5.5.0.5).

$$\vec{p}^{\,c.m.s}_B = \vec{p}^{\,c.m.s}_{K\pi} + \frac{\vec{p}^{\,c.m.s}_\gamma}{|\vec{p}_\gamma|^2} \times (E^{c.m.s}_{beam} - E^{c.m.s}_{K\pi}), \tag{5.5.0.5}$$

where $E^{c.m.s}_B$ is calculated as $E^{c.m.s}_B = E^{c.m.s}_\gamma + E^{c.m.s}_{K\pi}$. The peak of $M_{\rm bc}$ distribution should be near the mass of B meson (5.279 GeV/c^2) and that of ΔE should be near zero. Finally, we required that the window of $M_{\rm bc}$ is from 5.20 to 5.29 GeV/c^2 and that of ΔE is from -0.2 to 0.1 GeV. Summary of selection cut is shown in Table-5.5.1 and $M_{\rm bc}$, ΔE and $M(K\pi)$ distributions summed four channels are shown in Figure-5.5.6. Their distributions of individual four channels are shown in Figure-5.5.6 on Appendix.

Here we define the two regions, fit region and signal box. Fit region which is used for signal extraction is defined as $|M(K\pi) - m_{K^*}| < 0.075$ GeV/c^2, $5.20 < M_{\rm bc} < 5.29$ GeV/c^2. Signal box which is only used for optimization of background suppression selection is defined as $|M(K\pi) - m_{K^*}| < 0.075$ GeV/c^2, $5.27 < M_{\rm bc} < 5.29$ GeV/c^2.

Target Particles	cut value
Prompt photon	$1.8 < E_{\gamma}^{c.m.s} < 3.4$ GeV E9/E25 > 0.95 $33 < \theta_{\gamma}^{lab.} < 128$ degree (barrel only) $\mathcal{L}_{\gamma}^{\pi} < 0.3$, $\mathcal{L}_{\gamma}^{\eta} < 0.3$
Charged particle	$\|dz\| < 5.0$ cm $\|dr\| < 0.5$ cm charged track $p > 0.1$ GeV/c $\mathcal{LR}^{K/\pi} > 0.6$ for kaon $\mathcal{LR}^{K/\pi} < 0.9$ for pion
K_s	$\|m_{K_s}^{\rm PDG} - m_{\pi^+\pi^-}\| < 0.010$ GeV/c^2 apply standard selection of nisK_s finder
π^0	$\|m_{\pi^0}^{\rm PDG} - m_{\gamma\gamma}\| < 0.010$ GeV/c^2 $p_{\pi^0} > 0.50$ GeV/c $E_{\gamma} > 0.05$ GeV for two photons decayed from π^0 $\cos\theta_{\gamma\gamma} > 0.50$
$K\pi$ system	$M(K\pi)$ <2.0 GeV/c^2
B meson reconstruction selection	$5.20 < M_{\rm bc} < 5.29$ GeV/c^2 -0.2 $< \Delta E <$ 0.1 GeV
Fit region	$\|M(K\pi) - M_{K^*}\|$ <0.075 GeV/c^2 $5.20 < M_{\rm bc} < 5.29$ GeV/c^2
Signal box	$\|M(K\pi) - M_{K^*}\|$ <0.075 GeV/c^2 $5.27 < M_{\rm bc} < 5.29$ GeV/c^2

Table 5.5.1: Summary of selection criteria

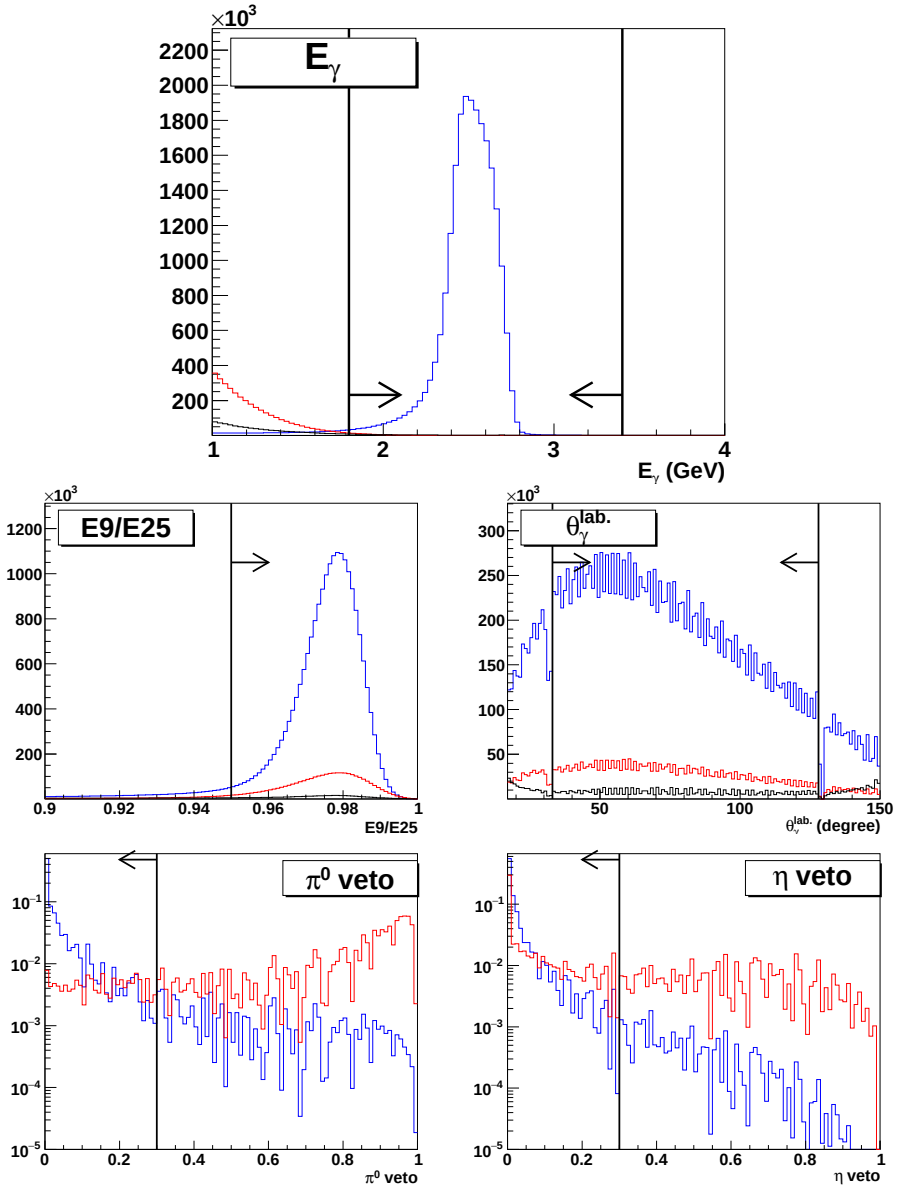

Figure 5.5.1: The distributions of energy of prompt photon candidate, E9/E25, photon polar angle in laboratory system, $\mathcal{LR}_{\pi^0}$ and $\mathcal{LR}_{\eta}$. Distributions of photon energy, E9/E25 and photon polar angle are made by only signal MC sample. Normalized distributions of $\mathcal{LR}_{\pi^0}$ and $\mathcal{LR}_{\eta}$ are made by signal MC and generic MC. Blue : truth prompt photon, red : photon background, Black : other backgrounds in figures of photon energy, E9/E25 and photon polar angle and Blue : truth prompt photon, red : photon decayed from π^0 or η.

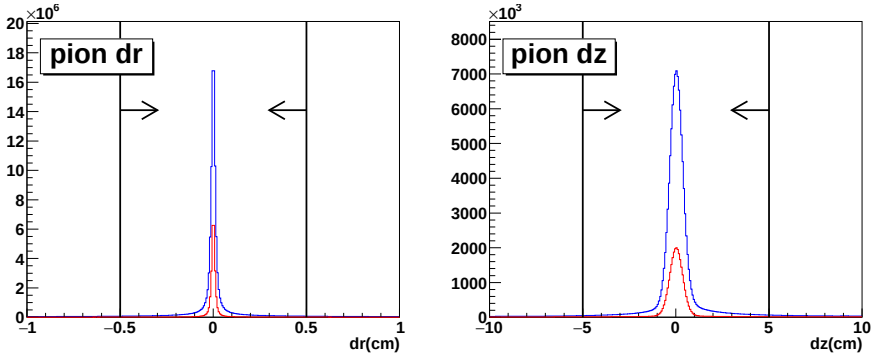

Figure 5.5.2: The distributions of "dr" and "dz" of π(blue) and K(red).

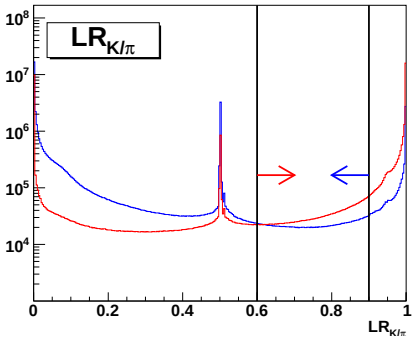

Figure 5.5.3: The distribution of K/π likelihood ratio. Red : π, Blue : K

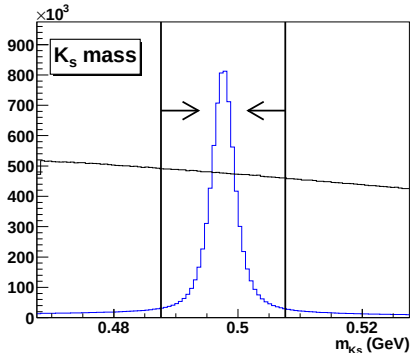

Figure 5.5.4: Reconstructed K_s mass distribution. Blue : Truth K_s or π^0, Black : fake candidates

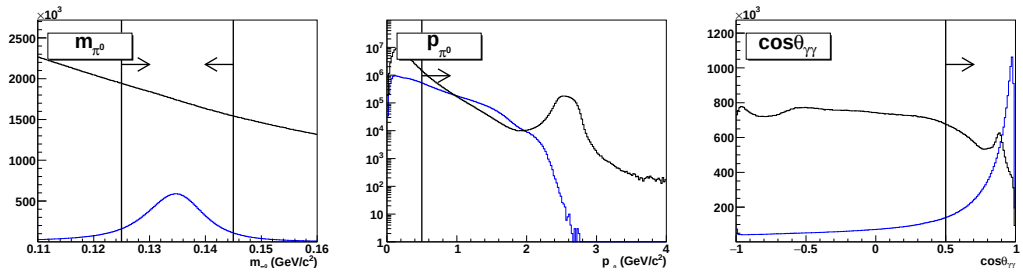

Figure 5.5.5: π^0 mass (left) and momentum (center) and $\cos\theta_{\gamma\gamma}$ (right) distributions. Blue : True π^0, Black : fake candidates

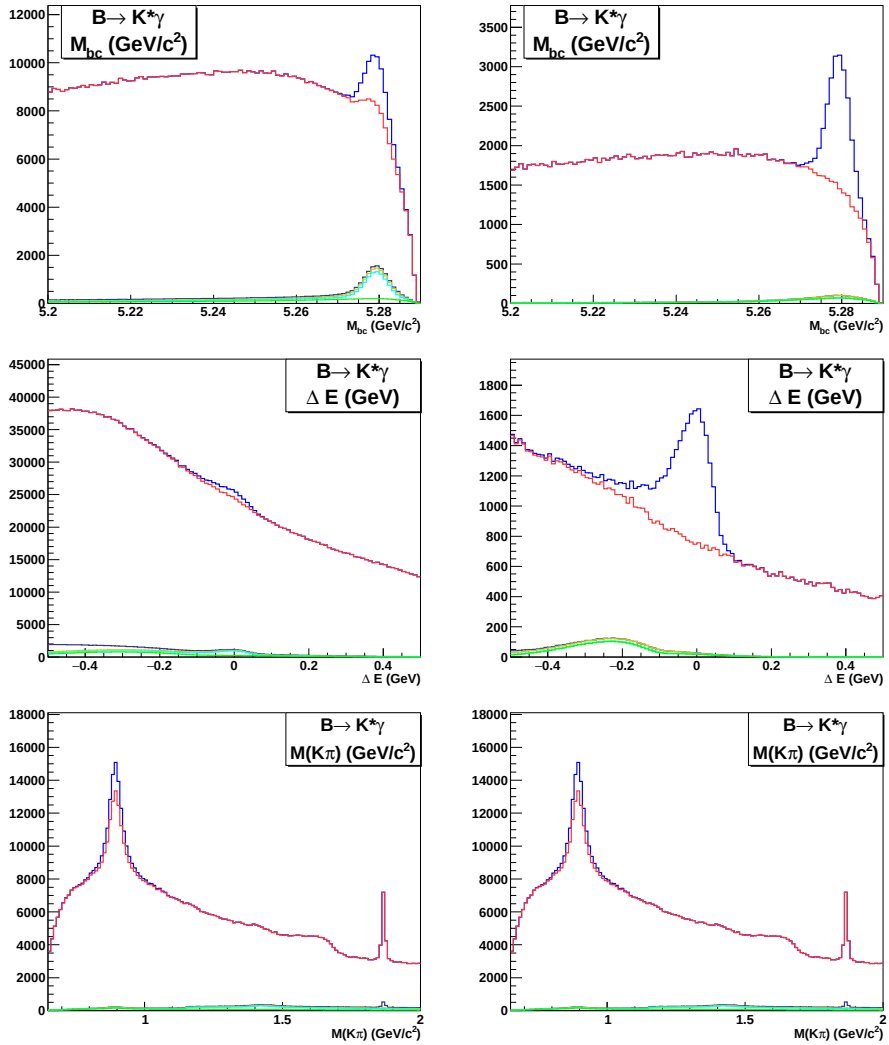

Figure 5.5.6: $M_{\rm bc}$, ΔE and $M(K\pi)$ distributions summed four channels with/without signal box requirement. Three left (right) side figures are no (a) requirement of signal box selection. Blue : signal, Red : $q\bar{q}$, Dark Blue : BB bkg, Yellow : Rare$B$ bkg, Cyan : $X_s\gamma$ bkg, Green : combinatorial bkg and cross-feeds

Chapter 6

Background Study

In this analysis, we considered six types of background, qq bkg, BB bkg, rare$B$ bkg, $X_s\gamma$ bkg combinatorial background and cross-feeds, which are defined in Section 4. The qq bkg is the largest contribution in both of fit region and signal box but this can be separated by event shape clearly. The method of qq bkg suppression is shown in Section 6.1. Since the expected number of BB bkg is small in fit region and signal box, there are no problem even without suppression. Since the contribution of rare$B$ bkg, $X_s\gamma$ bkg, combinatorial background and cross-feeds are not so large but these backgrounds make peaks in $M_{\rm bc}$ distribution, we have to know the behavior exactly. The study about rare$B$ and $X_s\gamma$ is written in Section 6.4. Contributions of combinatorial background and cross-feeds are evaluated in Section-6.3 and listed in Table 6.3.1.

6.1 qq bkg Suppression

To suppress the $q\overline{q}$ bkg, we use "Neurobayes" technique which is the multivariate analysis tool by machine learning. Nine types of input parameter are used and written in following.

Likelihood Ratio of KSFW ($\mathcal{LR}_{\rm KSFW}$)

In general, Kakuno Super Fox-Wolfram (KSFW) method is used for suppression of continuum background which is the largest background in the B decay analysis. KSFW which was developed in 2003 is the method of extended method of Super Fox-Wolfram method (SFW) which is the method to characterize the event shape using Fox-Wolfram moment. Here we introduce them.

◯ **Fox-Wolfram Moment**

Some variables such as thrust and sphericity, which are explained in following, to describe the event shape have to find a jet axis by minimizing. However, the event shape is able to characterized directly by Fox-Wolfram Momenta [43].

The l-th Fox-Wolfram momenta is defined in the center-of-mass frame as

$$H_l = \sum_{ij} |\vec{p}_i||\vec{p}_j| P_l(\cos\theta_{ij}), \tag{6.1.0.1}$$

where $\vec{p}_i$ and $\vec{p}_j$ are the momenta of the i-th and j-th particles in an event, respectively, P_l is the l-th Legendre polynomial and θ_{ij} is the angle between the two momentum vectors. The sum is over the particles in the final state. Note that the overall constant is ignored here for simplicity. The advantage using Fox-Wolfram Moment is this can provide rotationally invariant observables,

because the final state of e^+e- collision have no natural axis.

◯ **SFW (Super Fox-Wolfram)**

The SFW [44] is the method of calculating the Fox-Wolfram momenta with separating signal and other side B mesons, which means all of remaining particles except particles associated signal B meson and evaluated by two kinds of Fisher discriminant. Fisher discriminant is one of the techniques of the separating signal and background when performing multivariate analysis and can characterize the event by linear combination. SFW can is defined as

$$SFW = a_2 h_2^{so} + a_4 h_4^{so} + \sum_{j=1}^{4} b_j h_j^{oo}, \tag{6.1.0.2}$$

where a_2, a_4 and b_j are the coefficients of Fisher discriminant, h_2^{so} and h_4^{so} are second and forth normalized Fox-Wolfram moment, defined as Eq-6.1.0.3, consisted of two particles which are signal and other side B mesons, and h_j^{oo} is normalized $j-th$ Fox-Wolfram moment associated by only two particle in other side B meson candidate. Fisher coefficients are decided by optimizing the separation performance using signal and background MC sample. Normalized $l-th$ Fox-Wolfram momenta is given as

$$h_l^k = \frac{\sum_{m,n} |\vec{p_m}||\vec{p_n}| P_l(\cos\theta_{mn})}{\sum_{m,n} |\vec{p_m}||\vec{p_n}|}, \tag{6.1.0.3}$$

where k is the index to categorize the kind of Fox-Wolfram moment, so and oo, for example, when k is so, $\vec{p_m}$ and $\vec{p_n}$ are the momenta of the particles "m" associating signal side B meson and "n" associating other side B meson, and when k is oo, $\vec{p_m}$ and $\vec{p_n}$ are the momenta of the particles "m" and "n" associating only other side B meson. If the daughter particles decayed from B meson decay into some particles, the event shape should be isotropic but at the continuum events. Figure-6.1.1 show the image of event shape of qq and BB decays.

◯ **KSFW**

To improve the discrimination performance, the SFW is modified to Kakuno Super Fox-Wolfram (KSFW)[45] adding the information of charges of the particles, the missing mass of the event and normalization factor.

The KSFW is defined as

$$KSFW = \sum_{l=0}^{4} R_l^{so} + \sum_{l=0}^{4} R_l^{oo} + \gamma \sum_{n=1}^{N_t} |(P_t)_n| \tag{6.1.0.4}$$

where R_l^{so} and R_l^{oo} are modified Fox-Wolfram moments like h_l^{so} and h_l^{oo} defined in Eq-6.1.0.3, their detailed explanation can be found in following sentence and the third term is the sum of the transverse momenta in an event, γ is coefficient and and N_t is the number of particles.

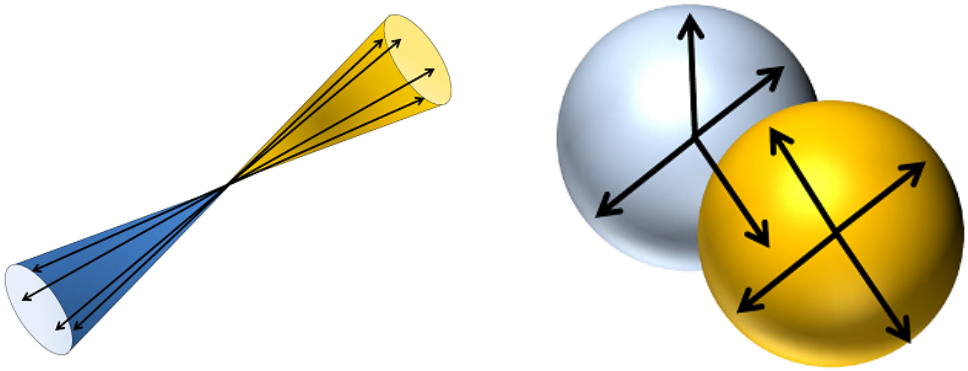

Figure 6.1.1: Event shape pictures of continuum (left) and BB (right)

- R_l^{so}

  In the calculation of R_l^{so}, particles are divided into three, charged particle (c), neutral particle (n), and missing particle (m). Since the missing four vector is treated as a particle, the type of missing particle is prepared. R_l^{so} is defined as

$$R_l^{so} = \frac{\alpha_l^c H_l^{so,c} + \alpha_l^n H_l^{so,n} + \alpha_l^m H_l^{so,m}}{E_{\text{beam}} - \Delta E}, \tag{6.1.0.5}$$

  where three αs are Fisher coefficients, and E_{beam} is the center of mass energy.

  If l is odd, Fox-Wolfram moments are given as

$$H_l^{so,n} = H_l^{so,m} = 0, \tag{6.1.0.6}$$

$$H_l^{so,c} = \sum_i \sum_{jx} Q_i Q_{jx} |p_{jx}| P_l(\cos\theta_{i,jx}), \tag{6.1.0.7}$$

  where i means the daughter particle of signal side B, j means that of other side one, x shows the type of particles ($x = c, n, m$), Q_i and Q_{jx} are the charge of the particle i and jx, $\theta_{i,jx}$ means the angle between i and jx. If l is even, the moments are given as

$$H_l^{so,x} = \sum_i \sum_{jx} |p_{jx}| P_l(\cos\theta_{i,jx}), \tag{6.1.0.8}$$

  which is similar function to Eq-6.1.0.7. In this term, two free parameters for odd l and nine free parameters for even l exist, therefore there are eleven free parameters corresponding to Fisher coefficients.

- R_l^{oo}

R_l^{oo} is associated by only other side B candidate and also has two definitions in the difference whether l is odd or even but do not separate the type of particles. These are described as

$$\begin{cases} R_l^{oo} = \sum_j \sum_k \beta_l Q_j Q_k |p_j||p_k| P_l(\cos\theta_{j,k}) \quad (l \ \text{ is odd}), & (6.1.0.9) \\ R_l^{oo} = \sum_j \sum_k \beta_l |p_j||p_k| P_l(\cos\theta_{j,k}) \quad (l \ \text{ is even}), & (6.1.0.10) \end{cases}$$

where β is free parameters corresponding to Fisher coefficient. This tern has five Fisher coefficients.

There are 17 Fisher coefficients in KSFW formula and these are optimized and probability density function (PDF) for signal and background are made using MC sample. Finally, using PDF generated above signal and background events are separated by likelihood ratio defined as

$$\mathcal{LR}_{KSFW} = \frac{\mathcal{L}^{signal}}{\mathcal{L}^{signal} + \mathcal{L}^{background}}. \quad (6.1.0.11)$$

Additionally, to improve the signal-to-background separation, 17 Fisher coefficients are optimized in each bin of missing mass square (M_{miss}) defined as

$$M_{miss}^2 = \left(E_{\Upsilon(4S)} - \sum_{n=1}^{N_t} E_n\right)^2 - \sum_{n=1}^{N_t} |p_n|^2, \quad (6.1.0.12)$$

where $E_{\Upsilon(4S)}$ is the energy of $\Upsilon(4S)$ corresponding to center-of-mass energy and E_n and p_n are the energy and momentum of n, respectively. There are seven separated regions by M_{miss}, (– -0.5 – 0.3 – 1.0 – 2.0 – 3.5 – 6.0 – GeV/c^2).

Cosine theta distribution of signal side B meson

$\Upsilon(4S)$ is spin-1 meson and decays into $B\overline{B}$ which are spin-0, so the angular distribution of B meson in the $\Upsilon(4S)$ frame can be represented by D-function like

$$|d^1_{1,0}(\theta)| \propto \frac{\sin^2\theta}{2} = \frac{1-\cos^2\theta_B}{2}, \quad (6.1.0.13)$$

where θ_B is an angle between the direction of electron beam and momentum direction of B meson in center-of-mass system. On the other hand, the $\cos\theta_B$ distribution of $q\overline{q}$ bkg should be flat because reconstructed B meson candidates are randomly.

Thrust

Thrust is one of the variables which can represent the event shape. For all of particles in an event, sum of the inner product of a unit vector and momenta of particles is calculated and

normalized with their momenta magnitude. When this value is maximized, it and the unit vector are described as thrust (T) and thrust vector ($\vec{n}_T$). These can be defined as

$$T = max \frac{\sum_{i=1}^{N} |\vec{\boldsymbol{n}}_{\boldsymbol{T}} \cdot \boldsymbol{p_i}|}{\sum_{i=1}^{N} |\boldsymbol{p_i}|}, \tag{6.1.0.14}$$

where p_i is i-th momentum.

$|\cos\theta_T|$ is one of the useful variable, where θ_T is the angle between the thrust axis calculated by momentum vectors of particles associated in signal and other B candidates, in center-of-mass system. $\cos\theta_T$ value of the event of BB should be flat within the range from 0 to 1 because $B\overline{B}$ pair which is almost rest in center-of-mass system is generated, and the distribution of their decay products is isotropic, so thrust axes distributions are random. However in $q\bar{q}$ events, due to jet like events, thrusts of signal and other side B candidates are parallel, so $|\cos\theta_T|$ value should be distributed close to 1. We assign $\cos\theta_T$ to input value for Neurobayes training but do not use thrust value.

Sphericity and related variables

Sphericity is also one of the parameters which can represent the event shape. The sphericity tensor S_{tensor} is given as

$$S^{\alpha,\beta}_{tensor} = \frac{\sum_{i=1}^{N} p_i^{\alpha} p_i^{\beta}}{\sum_{i=1}^{N} |\vec{p}_i|^2}, \tag{6.1.0.15}$$

where p is the momentum of (x, y, z) components, α and β are indicated x, y and z. Since sphericity S which is scalar value is defined by three-dimensional representation of the spatial distribution of the p_i collection, three eigen values of Eq-(6.1.0.15) which are positive and real are calculated. Using these eigen values λ_1, λ_2 and λ_3 constrained with sum of them corresponding to one and $\lambda_1 \geq \lambda_2 \geq \lambda_3$, sphericity and its related value, aplanarity (A), are defined as

$$S = \frac{3}{2}(\lambda_2 + \lambda_3) = \frac{3}{2}(1 - \lambda_1), \tag{6.1.0.16}$$

$$A = \frac{3}{2}\lambda_3. \tag{6.1.0.17}$$

The distributed range are $0 \leq S \leq 1$ and $0 \leq A \leq 1/2$ from the definition of $\lambda_{1,2,3}$. For the isotropic distribution, since eigen values should be close to each other, $\lambda_{1,2,3} \sim 1/3$, S and A are distributed close to 1 and 1/2. For jet like distribution such as continuum events, maximum eigen value (λ_3) is distributed near one, so both S and A values are close to zero.

In this analysis, sphericity S and aplanarity A calculated by only the particles associating other side B meson candidate are assigned to input variable for Neurobayes training to avoid to make bias to $M(K\pi)$ distribution. Furthermore, two variables related with sphericity axes are used. The $\cos\theta_{\mathrm{v1-z}}$ which is the cosine of an angle between 1st sphericity axis of all tracks and z direction and the $\cos\theta_{\mathrm{v1\_v1}}$ is the cosine of an angle between 1st sphericity axes of signal-side and of other B side are added to that of input parameters. The sphericity axes are collinear to the eigen vectors of Eq-6.1.0.17, and the mean of 1st sphericity axis is corresponding to the eigen vector of λ_1. The concept of v1_v1 is near $\cos\theta_T$, so these distributions are similar to each other.

B flavor tagging quality, *qr*

Flavor tagging of the other-side B meson is useful for the additional background discrimination because flavor tagging performance is not good in continuum events [46]. Flavor tagging quality is evaluated using two parameters q and r in the Belle experiment. q is 3 times of b quark charge and r is MC value of flavor reliability and consistent to $1-2w$, where w is the fraction of mis-identification of B meson flavor so-called wrong tag fraction. The range of r is from zero for the event which has no flavor information to one for the event whose flavor can be determined obviously.

Following five types of particle are used for the good performance of flavor tagging and the decay by which these particles are generated can be found in Figure-6.1.2, 6.1.3, 6.1.4,

(1) high-momentum lepton from $\overline{B}^0 \to Xl^-\nu$ decays, primary lepton,

(2) intermediate momentum leptons from $\overline{b} \to \overline{c} \to \overline{s}$, secondary lepton,

(3) kaons in the decay chain of $b \to c \to s$,

(4) slow pions from $B^0 \to D^{*-}X$, $D^{*-} \to \overline{D^0}\pi^-$ decays, and

(5) $\overline{\Lambda}$ baryons from the cascade decays $\overline{b} \to \overline{c} \to \overline{s}$.

Using a look-up table of binned multi-dimensional likelihood which is consisted of momentum magnitude in center-of-mass system, polar angle in laboratory system and K/π identification, the signed probability, $q \cdot r$, is given by

$$q \cdot r = \frac{N(B^0) - N(\overline{B^0})}{N(B^0) + N(\overline{B^0})} \tag{6.1.0.18}$$

where $N(B^0)$ and $N(\overline{(B^0)})$ are the numbers of B^0 and $\overline{B^0}$ in each bin of the look-up table prepared from a large statistics MC event sample. Since the particles used for flavor tagging are considered based on in the decay chain of $b \to c \to s$, continuum events have poor information so $q \cdot r$ should be distributed near 0. For the events decayed from B meson, $q \cdot r$ is distributed around 0 and ± 1 because flavor of some events can be determined clearly.

Figures in Figure-6.1.5 show the normalized distributions of Neurobayes input parameters.

6.2 Neurobayes Training and Performance Check

200 streams signal MC sample and 2 streams $q\overline{q}$ bkg sample are used as training samples. The selection value is determined by maximizing the significance defined in Eq-5.0.0.1. The significance optimization is performed in the signal box. In this selection, 89% of continuum backgrounds are

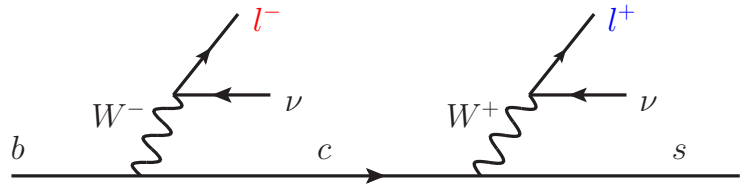

Figure 6.1.2: A diagram of the decay used for flavor tagging. By capturing primary and secondary lepton, flavor tagging information is obtained. The red l is primary lepton and blue one is secondly lepton. Here τ is not considered, therefor we only use e and μ.

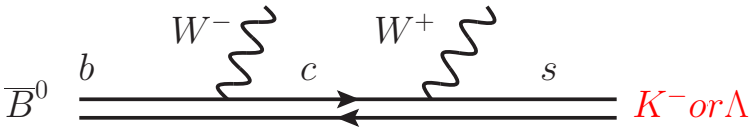

Figure 6.1.3: A diagram of the decay used for flavor tagging. By capturing charged K and Λ, flavor tagging information is obtained.

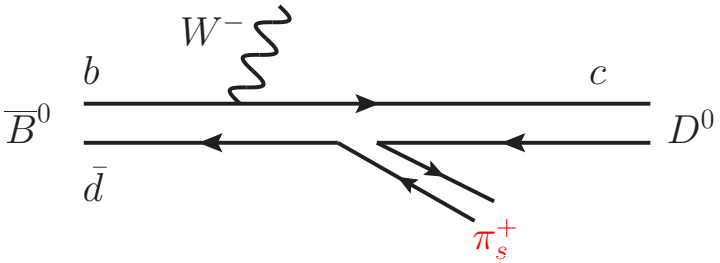

Figure 6.1.4: A diagram of the decay used for flavor tagging. By capturing slow charged pion, flavor tagging information is obtained.

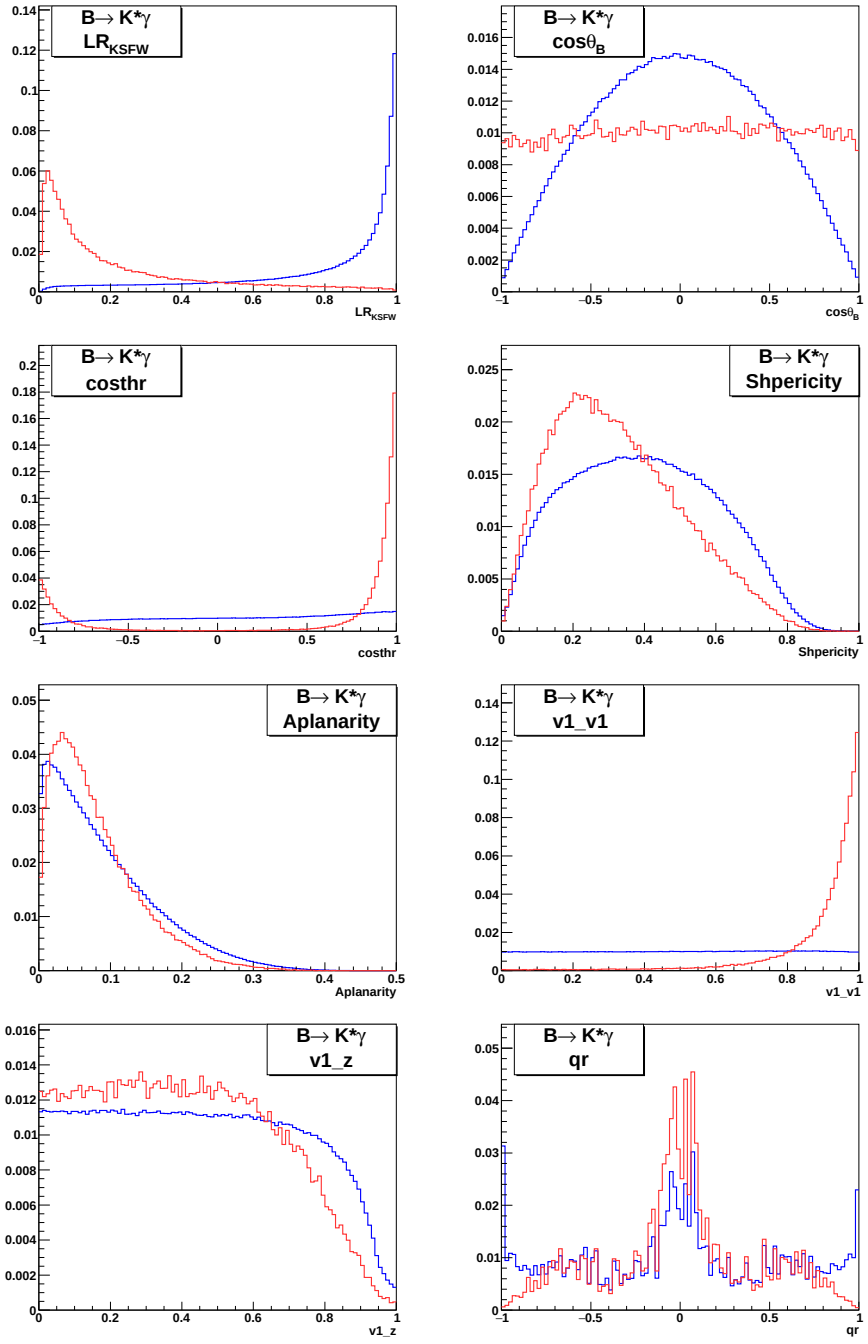

Figure 6.1.5: Input parameters of Neurobayes, Blue:Signal, Red:Background

rejected with remaining 83% of signal events and Table-6.2.1 shows the continuum suppression performance for individual modes. Figure-6.2.2 shows the separation of signal and background by Neurobayes output. Figure-6.2.3 shows the variation of significance and efficiency with changing NB output. The efficiency is defined as **efficiency** $= N_{\rm signal}/N_{\rm gen}$, where $N_{\rm signal}$ is the number of remaining signal and $N_{\rm gen}$ is the number of generated events which is the all of events of $B^0 \to K^{*0}\gamma$ or $B^+ \to K^{*+}\gamma$ with charge conjugate. When we calculate the efficiency of $B^0 \to K_s\pi^0\gamma$, efficiency is defined as (Number of remaining events of $B^0 \to K_s\pi^0\gamma$) / (Number of generated events of $B^0 \to K^{*0}\gamma$). We check the correlation between $M_{\rm bc}$, signal extraction parameter, and Neurobayes output. Figure-6.2.1 shows the correlation plots among Neurobayes input parameters, its output and $M_{\rm bc}$ and we can find there is no correlation.

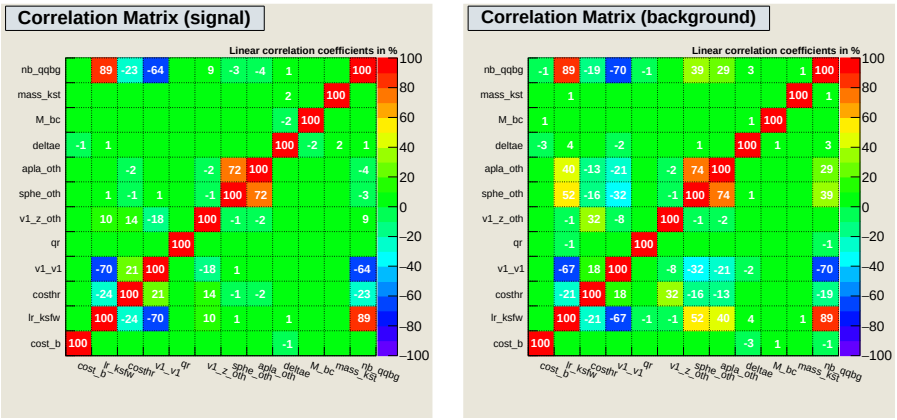

Figure 6.2.1: Correlation among input parameters for Neurobayes training, parameters of signal extraction and Neurobayes output. Left figure is signal and right one is background. The means of parameter name are following, "cost_b":$\cos\theta_B$, "lr_ksfw":likelihood ration of KSFW, "costhr":$\cos\theta_T$, "v1_z_oth":cosine of the angle between 1st sphericity vector axis in other side B meson and electron beam direction, "sphe_oth":sphericity of other side B, "apla_oth":aplanarity of other side B, "nb_qqbg":output value of Neurobayes

Decay	$K_s\pi^0\gamma$	$K^+\pi^-\gamma$	$K_s\pi^+\gamma$	$K^+\pi^0\gamma$
qq bkg reject. (%)	89.1%	89.3%	88.0%	89.2%
signal keep (%)	84.6%	83.4%	83.1%	84.0%

Table 6.2.1: Summary of qq bkg suppression using Neurobayes. "qq rejection" and "signal keeping" are the fraction between remaining qq or signal events after NB selection and their initial events

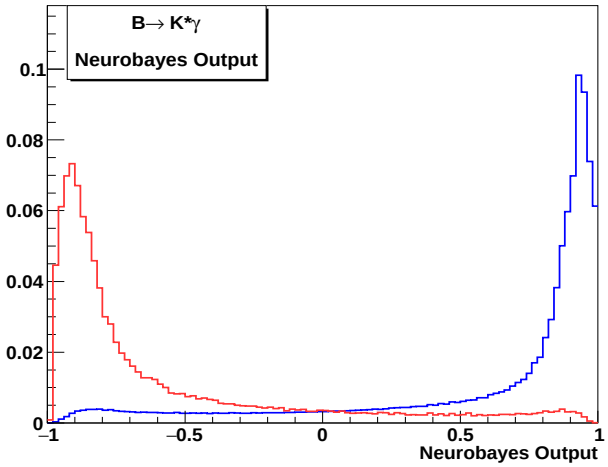

Figure 6.2.2: Neurobayes output distributions. Blue:Signal, Red:continuum

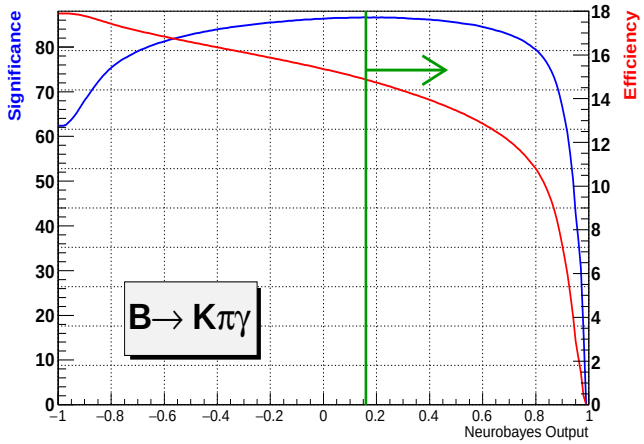

Figure 6.2.3: The graph of significance (blue) and efficiency (red) v.s NB output.

$K_s\pi^0\gamma$	Signal	qq	BB	rare$B$	$X_s\gamma$	Comb.	Cross.	Eff.	Signif.
Generate	10798.9	2.3×10^9	7.5×10^8	5.1×10^6	4.9×10^5	0.0	55068.2	33.41%	0.19
Reconstruct	569.1	2211.8	2.8	8.3	42.4	38.2	6.0	1.76%	10.61
π^0/η veto	522.9	889.8	2.0	6.8	38.3	35.0	5.5	1.62%	13.50
qq suppress	442.5	95.2	0.8	5.5	30.3	27.0	3.1	1.37%	18.00
Rand. Select	405.1	89.2	0.7	5.1	28.0	18.8	1.8	1.25%	17.29

$K^+\pi^-\gamma$	Signal	qq	BB	rare$B$	$X_s\gamma$	Comb.	Cross.	Eff.	Signif.
Generated	21599.9	2.3×10^9	7.5×10^8	5.1×10^6	4.9×10^5	0.0	44267.2	66.82%	0.39
Reconstruct	7457.2	33597.2	8.3	247.1	404.6	109.6	52.9	23.07%	36.44
π^0/η veto	6852.4	13207.0	5.7	178.0	366.3	99.5	47.8	21.20%	47.56
qq suppress	5712.9	1412.0	2.7	143.2	287.1	70.2	31.0	17.67%	65.28
Rand. Select	5340.2	1292.2	2.5	124.7	263.4	50.1	23.3	16.52%	63.39

$K_s\pi^+\gamma$	Signal	qq	BB	rare$B$	$X_s\gamma$	Comb.	Cross.	Eff.	Signif.
Generated	22245.0	2.3×10^9	7.5×10^8	5.1×10^6	4.9×10^5	0.0	43622.1	66.79%	0.40
Reconstruct	2650.4	10955.0	4.0	155.7	186.9	79.3	30.0	7.96%	22.35
π^0/η veto	2425.7	4430.0	2.7	90.1	169.3	71.8	27.1	7.28%	28.55
qq suppress	2016.6	529.2	2.0	71.8	132.7	52.5	17.7	6.05%	37.96
Rand. Select	1791.7	445.0	1.5	55.9	111.9	33.1	10.5	5.38%	36.20

$K^+\pi^0\gamma$	Signal	qq	BB	rare$B$	$X_s\gamma$	Comb.	Cross.	Eff.	Signif.
Generated	11112.0	2.3×10^9	7.5×10^8	5.1×10^6	4.9×10^5	0.0	54755.1	33.36%	0.20
Reconstruct	1762.5	12652.8	9.8	62.8	117.0	110.5	19.9	5.29%	14.52
π^0/η veto	1614.7	5023.2	6.0	40.3	105.9	100.8	17.9	4.85%	19.43
qq suppress	1358.4	537.8	3.3	32.8	81.3	76.1	10.3	4.08%	29.64
Rand. Select	1284.5	507.0	3.2	31.3	77.0	54.9	7.0	3.86%	28.98

Table 6.2.2: Number of remaining events for each selection in the signal box at the type of qq suppression **after** random selection. Signal is each exclusive signal decay channel but The efficiency is remaining events over generated events and significance is defined as $S/\sqrt{S+B}$ where S and B are the number of remaining events of signal and backgrounds components.

$K_s\pi^0\gamma$	Signal	qq	BB	rare$B$	$X_s\gamma$	Comb.	Cross.	Eff.	Signif.
Generated	10798.9	2.3×10^9	7.5×10^8	5.1×10^6	4.9×10^5	0.0	55068.2	33.41%	0.19
Reconstruct	569.1	2211.8	2.8	8.3	10.6	38.2	6.0	1.76%	10.67
π^0/η veto	522.9	889.8	2.0	6.8	9.5	35.0	5.5	1.62%	13.63
Rand. Select	465.0	722.8	1.7	6.0	34.8	22.9	2.7	1.44%	12.6
qq suppress	400.2	83.5	0.3	5.0	28.4	18.0	1.6	1.24%	17.26

$K^+\pi^-\gamma$	Signal	qq	BB	rare$B$	$X_s\gamma$	Comb.	Cross.	Eff.	Signif.
Generated	21599.9	2.3×10^9	7.5×10^8	5.1×10^6	4.9×10^5	0.0	44267.2	66.82%	0.39
Reconstruct	7457.2	33597.2	8.3	247.1	136.2	109.6	52.9	23.07%	36.56
π^0/η veto	6852.4	13207.0	5.7	178.0	122.8	99.5	47.8	21.20%	47.84
Rand. Select	6292.7	11524.0	4.2	151.5	332.3	67.1	34.9	19.47%	46.38
qq suppress	5250.5	1176.8	2.0	121.5	264.6	48.5	22.6	16.24%	63.27

$K_s\pi^+\gamma$	Signal	qq	BB	rare$B$	$X_s\gamma$	Comb.	Cross.	Eff.	Signif.
Generated	22245.0	2.3×10^9	7.5×10^8	5.1×10^6	4.9×10^5	0.0	43622.1	66.79%	0.40
Reconstruct	2650.4	10955.0	4.0	155.7	72.7	79.3	30.0	7.96%	22.44
π^0/η veto	2425.7	4430.0	2.7	90.1	65.9	71.8	27.1	7.28%	28.76
Rand. Select	2094.3	3471.2	2.0	68.7	144.8	42.0	15.8	6.29%	27.41
qq suppress	1733.2	372.5	1.2	54.4	106.8	30.9	9.9	5.20%	36.07

$K^+\pi^0\gamma$	Signal	qq	BB	rare$B$	$X_s\gamma$	Comb.	Cross.	Eff.	Signif.
Generated	11112.0	2.3×10^9	7.5×10^8	5.1×10^6	4.9×10^5	0.0	54755.1	33.36%	0.20
Reconstruct	1762.5	12652.8	9.8	62.8	33.9	110.5	19.9	5.29%	14.56
π^0/η veto	1614.7	5023.2	6.0	40.3	30.1	100.8	17.9	4.85%	19.53
Rand. Select	1489.9	4273.8	5.7	37.2	94.5	69.6	10.8	4.47%	19.26
qq suppress	1213.3	340.2	2.5	29.1	63.7	49.8	5.7	3.64%	29.39

Table 6.2.3: Number of remaining events for each selection in the signal box at the type of qq suppression **before** random selection. Signal is each exclusive signal decay channel but The efficiency is remaining events over generated events and significance is defined as $S/\sqrt{S+B}$ where S and B are the number of remaining events of signal and backgrounds components.

6.3 Random Candidate Selection

After the continuum background suppression, we have to select one B meson candidate in an event which is stored multi-candidates. Figure-6.3.1 shows the number of B meson candidate in an events. 87 % of signal MC events have only one candidate. The average of number of B meson candidate in an event is 1.16. In this study, we select the candidate at random using random number generator of TRandom3 class in ROOT package [47]. Table 6.3.1 shows the purity of each decay channel. "Perfect" reconstruction in Table 6.3.1 means that we can reconstruct the B meson with three correct particles. Other boxes are combinatorial backgrounds and cross-feeds. The number of remaining events every selection is summarized in Table-6.2.2. The difference of background suppression performance between the order of background suppression after random candidate selection and before one is evaluated and we apply background suppression "before" random candidate selection. The number of remaining events every selection which is applied background suppression after random candidate selection is summarized in Table-6.2.3.

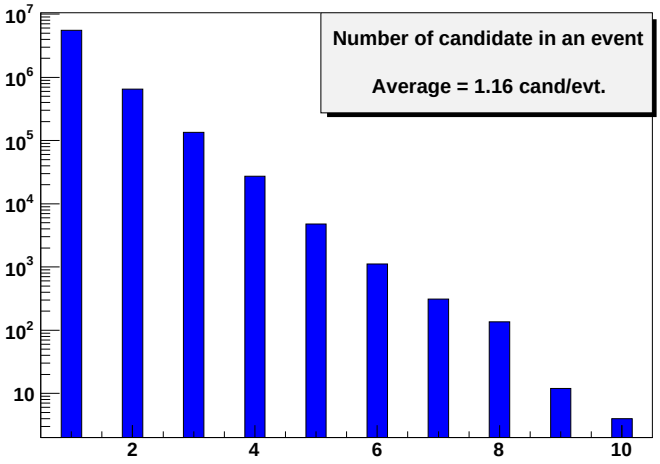

Figure 6.3.1: The average of number of candidates in an event

Decay	Perfect	$K_s\pi^0\gamma$	$K^+\pi^-\gamma$	$K_s\pi^+\gamma$	$K^+\pi^0\gamma$
$K_s\pi^0\gamma$	92.7%	6.0%	0%	1.3%	0%
$K^+\pi^-\gamma$	95.3%	0%	3.0%	0.1%	1.6%
$K_s\pi^+\gamma$	93.1%	2.4%	0.2%	4.3%	0%
$K^+\pi^0\gamma$	92.8%	0.2%	1.2%	0.2%	5.6%

Table 6.3.1: Purity and cross-feeds and combinatorial background fractions table in signal box. The row of the table shows reconstruction channel, the column shows the truth decay channel. "Perfect" in the table means reconstructed B meson candidate is associated by particles which are decayed from signal side B meson based on MC truth checking. The boxes which are located in the same reconstruction channel and truth channel show the combinatorial backgrounds. The other boxes show cross-feeds.

6.4 Major Background from B decay

The peak position of K^* in $M(K\pi)$ distribution can be separated from that of other $X_s\gamma$, so there are small contributions and we do not have to reconstruct the main source and reject it. In this section, we only check the kind of background source.

The source of peaking background in $M_{\rm bc}$ is rare$B$ bkg, $X_s\gamma$ bkg and cross-feeds. Contribution of BB generic decay is negligible. Assumed branching fraction of rare$B$ sample is based on PDG2008. Since the branching fraction of $B \to K^*\pi^0$ is updated [48] from $\mathcal{B}(B^+ \to K^{*+}\pi^0) = (6.9 \pm 2.4) \times 10^{-6}$ to $\mathcal{B}(B^+ \to K^{*+}\pi^0) = (8.2 \pm 1.9) \times 10^{-6}$, contribution from $B^+ \to K^{*+}\pi^0$ is scaled. Table-(6.4.1) and (6.4.2) are summary table of contribution fraction of rare$B$ bkg and $X_s\gamma$ bkg respectively.

Rank	$K_s\pi^0\gamma$	$K^+\pi^-\gamma$	$K_s\pi^+\gamma$	$K^+\pi^0\gamma$
1	$K^{*0}\eta$ (69%)	$K^{*0}\eta$ (60%)	$K^{*+}\eta$ (48%)	$K^{*+}\eta$ (48%)
2	$X_s^0\eta$ (16%)	$X_s^0\eta$ (8%)	$K^{*+}\pi^0$ (28%)	$K^{*+}\pi^0$ (28%)
3	$K^{*0}(1410)\eta$ (2%)	$X_d^0\gamma$ (5%)	$X_s^+\eta$ (6%)	$X_d^+\gamma$ (6%)
4	$X_s^0\eta'$ (2%)	$\rho^0\gamma$ (4%)	$K^0\pi^0$ (4%)	$X_s^+\eta$ (6%)
5	$X_d\gamma$ (1%)	$K^+\pi^0$ (3%)	$K^0\eta'$ (3%)	$\rho^+\gamma$ (4%)
others	10%	20%	11%	8%

Table 6.4.1: Summary of background contributions in rare$B$ bkg

Rank	$K_s\pi^0\gamma$	$K^+\pi^-\gamma$	$K_s\pi^+\gamma$	$K^+\pi^0\gamma$
1	$K^0\rho^+\gamma$ (50%)	$K^+\rho^-\gamma$ (34%)	$K^0\rho^+\gamma$ (25%)	$K^+\rho^-\gamma$ (49%)
2	$K^{*0}\pi^+\gamma$ (15%)	$K^{*0}\pi^+\gamma$ (20%)	$K^{*+}\pi^-\gamma$ (22%)	$K^{*+}\pi^-\gamma$ (14%)
3	$K^{*0}\pi^0\gamma$ (11%)	$K^+\rho^0\gamma$ (16%)	$K^0\rho^0\gamma$ (22%)	$K^{*+}\pi^0\gamma$ (12%)
4	$K^{*+}\pi^0\gamma$ (8%)	$K^{*0}\pi^0\gamma$ (11%)	$K^{*+}\pi^0\gamma$ (8%)	$K^{*0}\pi^0\gamma$ (8%)
5	$K^+\pi^0\gamma$ (5%)	$K^{*+}\pi^-\gamma$ (6%)	$K^{*+}(1410)\pi^-\gamma$ (6%)	$K^0\pi^0\gamma$ (5%)
others	11%	13%	17%	12%

Table 6.4.2: Summary of $X_s\gamma$ bkg background contributions, here $K\pi\gamma$ is non-resonant contribution.

Chapter 7

Signal Extraction

Signal yields are extracted by unbinned maximum likelihood fitting of $M_{\rm bc}$.

7.1 The Decision of Probability Density Function (PDF)

By a binned likelihood fitting, the PDFs of signal and six types of background are decided. All PDFs are used a common in four decay channels.

We use different **Signal** PDFs depending on whether the modes include π^0 or not. Gaussian is used for modes without π^0, for modes and without π^0. For modes with π^0, Crystal Ball function [49] defined as

$$f_{CrystalBall}(x) = \frac{1}{\sigma \cdot \left(\frac{n}{|\alpha|\cdot}\frac{1}{n-1}\exp\left(-\frac{|\alpha|^2}{2}\right) + \sqrt{\frac{\pi}{2}}\left(1+erf(\frac{|\alpha|}{\sqrt{2}})\right)\right)} \tag{7.1.0.1}$$

$$\cdot \begin{cases} \exp(-\frac{(x-\mu)^2}{2\sigma^2}), & \text{for } \frac{x-\mu}{\sigma} > -\alpha \\ \left(\frac{n}{|\alpha|}\right)^n \exp\left(-\frac{|\alpha|^2}{2}\right)\cdot\left((\frac{n}{|\alpha|}-|\alpha|)-\frac{x-\mu}{\sigma}\right)^{-n}, & \text{for } \frac{x-\mu}{\sigma} < -\alpha \end{cases} \tag{7.1.0.2}$$

where μ is the mean, σ is the width, α and n are the parameters to represent the tail part is used.

***qq* bkg** PDF is defined as ARGUS function[50] defined in Eq-(7.1.0.3)

$$f_{ARGUS}(x) = x\cdot\left\{1-\left(\frac{x}{m_0}\right)^2\right\}^p \cdot \exp\left[-c\left\{1-\left(\frac{x}{m_0}\right)^2\right\}\right] \tag{7.1.0.3}$$

where m_0 is the end point and c is slope parameter. The parameter m_0 is fixed at the value determined by fitting the $M_{\rm bc}$ distribution of the control sample of $B \to D\pi$ is explained in Section-8.8 and p is also fixed at 0.5. Figure-7.1.1 show the two type of signal PDFs fitted by Crystal ball function and Gaussian and qq bkg PDF fitted by ARGUS function.

PDF of ***BB* bkg** are determined as ARGUS function. PDFs of **rare*B* bkg**, ***X*$_s\gamma$ bkg**, combinatorial background and cross-feeds are determined as ARGUS function added Bifurcated Gaussian All PDF parameters of BB, rare$B$, $X_s\gamma$, combinatorial and cross-feeds backgrounds and number of events of BB, rare$B$ and $X_s\gamma$ backgrounds are fixed at MC value. Number of events of combinatorial backgrounds and cross-feeds is scaled by signal yields because these background generated by $B \to K^*\gamma$ decay. We summarized the fit functions for each sample and the condition of fit parameters are listed in Table 7.1.1. The all figures of fitted distributions can be found in Appendix-11.3.

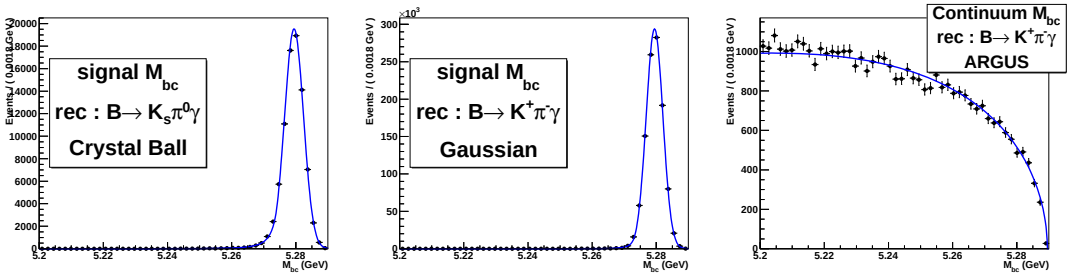

Figure 7.1.1: $M_{\rm bc}$ distribution fitted by Crystal ball function for $B^0 \to K_s\pi^0\gamma$ (left), Gaussian for $B^0 \to K^+\pi^-\gamma$ (center) and qq bkg sample (right).

Fit sample	$M_{\rm bc}$ fit function	Fit Parameters
Signal	Gaussian (without π^0 modes) Crystal Ball function (with π^0 modes)	**Gaussian** (without π^0 modes) mean : fixed at the mean of $M_{\rm bc}$ distribution of $B \to D\pi$ width : float **Crystal Ball function** (with π^0 modes) mean : fixed at the mean of $M_{\rm bc}$ distribution of $B \to D\pi$ width : float tail parameter α: fixed at MC value tail parameter n : fixed at MC value **yield** : float
qq bkg	ARGUS function	end point m0 : fixed at MC value p : fixed at 0.5 slope parameter c : float **yield** : float
$B\bar{B}$ bkg	ARGUS function	end point m0 : fixed at MC value p : fixed at 0.5 slope parameter c : fixed at MC value **yield** : fixed at MC value
rare$B$ bkg $X_s\gamma$ bkg Combinatorial bkg Cross-feeds	ARGUS function + Bifurcated Gaussian	**ARGUS function** end point m0 : fixed at MC value p : fixed at 0.5 slope parameter c : fixed at MC value number of events : fixed at MC value **Bifurcated Gaussian** mean : fixed at MC value left width : fixed at MC value right width : fixed at MC value **yield** : • rare$B$ and $X_s\gamma$ bkg : fixed at MC value • combinatorial cross-feeds bkg : determining the fraction for signal events and scaled.

Table 7.1.1: Summary of fit function and fitter parameters. The same PDFs are defined in rare$B$, $X_s\gamma$ bkg, Combinatorial and cross-feeds bkg sample but we fit them individually.

7.2 Fitting Method

To perform the extended maximum likelihood fitting, likelihood function is defined as

$$\mathcal{L}(x_1, \ldots, x_N) = \prod_{i=1}^{N} \mathcal{P}_{M_{\rm bc}}(x_i, \Theta_{M_{\rm bc}}), \tag{7.2.0.4}$$

where $\Theta_{M_{\rm bc}}$ is fit parameter for $M_{\rm bc}$, x_i is measured $M_{\rm bc}$ variables and $\mathcal{P}_{M_{\rm bc}}$ is PDF of $M_{\rm bc}$ determined in section-7.1.

In this analysis, measured variables are obtained by simultaneous fitting except branching fraction and CP asymmetry for individual channels. We can redefine the branching fraction and CP asymmetry defined in Eq-(2.4.2.4) using bottom quark charge difference such as

$$BF = \frac{N_{sig}^{\overline{B}}}{N_{B\overline{B}}\epsilon^{\overline{B}}} + \frac{N_{sig}^{B}}{N_{B\overline{B}}\epsilon^{B}} \tag{7.2.0.5}$$

$$A_{CP} = \frac{1}{1-2w}\frac{N_{sig}^{\overline{B}}/\epsilon^{\overline{B}} - N_{sig}^{B}/\epsilon^{B}}{N_{sig}^{\overline{B}}/\epsilon^{\overline{B}} + N_{sig}^{B}/\epsilon^{B}} \tag{7.2.0.6}$$

where N_{sig}, $N_{B\overline{B}}$, ϵ and w are signal yield, number of $B\overline{B}$ pairs, detection efficiency and wrong-tag fraction. Using Eq-(7.2.0.5) and Eq-(7.2.0.6), signal yields of $\overline{B}$ and B can be described as

$$N_{sig}^{\overline{B}} = BF \cdot N_{B\overline{B}} \cdot \epsilon^{\overline{B}} \cdot \frac{(1 + (1-2w)A_{CP})}{2}, \tag{7.2.0.7}$$

$$N_{sig}^{B} = BF \cdot N_{B\overline{B}} \cdot \epsilon^{B} \cdot \frac{(1 - (1-2w)A_{CP})}{2} \tag{7.2.0.8}$$

and then we can obtain the signal yield, branching fraction and A_{CP} by maximum likelihood fitting.

In the decay of $B \to K_s\pi^0\gamma$, since we can not identify the flavor by self-tagging, A_{CP} can not be determined then the signal yields is defined as

$$N_{sig} = BF \cdot N_{B\overline{B}}\epsilon \tag{7.2.0.9}$$

and we can also obtain the signal yield and branching fraction.

Here we perform six type of fitting and their likelihood function definitions are

$$f_0(M_{\rm bc}) = - \sum_i \ln \mathcal{L}_i^{K_s\pi^0\gamma}(BF^0), \tag{7.2.0.10}$$

$$f_1(M_{\rm bc}) = - \sum_i \ln \mathcal{L}_i^{K^+\pi^-\gamma}(BF^1, A_{CP}^1) - \sum_i \ln \mathcal{L}_i^{K^-\pi^+\gamma}(BF^1, A_{CP}^1), \tag{7.2.0.11}$$

$$f_2(M_{\rm bc}) = - \sum_i \ln \mathcal{L}_i^{K_s\pi^+\gamma}(BF^2, A_{CP}^2) - \sum_i \ln \mathcal{L}_i^{K_s\pi^-\gamma}(BF^2, A_{CP}^2), \tag{7.2.0.12}$$

$$f_3(M_{\rm bc}) = - \sum_i \ln \mathcal{L}_i^{K^+\pi^0\gamma}(BF^3, A_{CP}^3) - \sum_i \ln \mathcal{L}_i^{K^-\pi^0\gamma}(BF^3, A_{CP}^3), \tag{7.2.0.13}$$

$$\begin{aligned} f_4(M_{\rm bc}) = & - \sum_i \ln \mathcal{L}_i^{K_s\pi^0\gamma}(BF^N) \\ & - \sum_i \ln \mathcal{L}_i^{K^+\pi^-\gamma}(BF^N, A_{CP}^{comb.}) - \sum_i \ln \mathcal{L}_i^{K^-\pi^+\gamma}(BF^N, A_{CP}^{comb.}) \\ & - \sum_i \ln \mathcal{L}_i^{K_s\pi^+\gamma}(BF^C, A_{CP}^{comb.}) - \sum_i \ln \mathcal{L}_i^{K_s\pi^-\gamma}(BF^C, A_{CP}^{comb.}) \\ & - \sum_i \ln \mathcal{L}_i^{K^+\pi^0\gamma}(BF^C, A_{CP}^{comb.}) - \sum_i \ln \mathcal{L}_i^{K^-\pi^0\gamma}(BF^C, A_{CP}^{comb.}), \end{aligned} \tag{7.2.0.14}$$

$$\begin{aligned} f_5(M_{\rm bc}) = & - \sum_i \ln \mathcal{L}_i^{K_s\pi^0\gamma}(BF^N) \\ & - \sum_i \ln \mathcal{L}_i^{K^+\pi^-\gamma}(BF^N, A_{CP}^{N}) - \sum_i \ln \mathcal{L}_i^{K^-\pi^+\gamma}(BF^N, A_{CP}^{N}) \\ & - \sum_i \ln \mathcal{L}_i^{K_s\pi^+\gamma}(BF^C, A_{CP}^{C}) - \sum_i \ln \mathcal{L}_i^{K_s\pi^-\gamma}(BF^C, A_{CP}^{C}) \\ & - \sum_i \ln \mathcal{L}_i^{K^+\pi^0\gamma}(BF^C, A_{CP}^{C}) - \sum_i \ln \mathcal{L}_i^{K^-\pi^0\gamma}(BF^C, A_{CP}^{C}), \end{aligned} \tag{7.2.0.15}$$

where upper index of BF and A_{CP} represent decay channels, in order of small number they are $K_s\pi^0\gamma$, $K^+\pi^-\gamma$, $K_s\pi^+\gamma$ and $K^+\pi^0\gamma$, and the mean of "C" and "N" are decay of $B^+ \to K^{*+}\gamma$ and $B^0 \to K^{*0}\gamma$ with charge conjugate, and the mean of "$A_{CP}^{comb.}$" is the CP asymmetry between $\overline{B}$ and B. Likelihood function f_0 and f_1 are defined in Eq-(7.2.0.10) and Eq-(7.2.0.11) are assigned for obtaining the branching fractions of $B \to K_s\pi^0\gamma$ and $B \to K^+\pi^-\gamma$, f_2 and f_3 defined in Eq-(7.2.0.12) and Eq-(7.2.0.13) are assigned for obtaining the branching fractions and CP asymmetries of $B^+ \to K_s\pi^+\gamma$ and $B^+ \to K^+\pi^0\gamma$, f_4 defined in Eq-(7.2.0.14) is assigned for obtaining the combined A_{CP} with constraint of common A_{CP} in three modes and f_5 defined in Eq-(7.2.0.15) is assigned for obtaining the branching fractions and CP asymmetries of $B^0 \to K^{*0}\gamma$ and $B^+ \to K^{*+}\gamma$, isospin asymmetry defined in Eq-(2.4.2.6) and ΔA_{CP} defined in Eq-(2.4.2.8) with constraint of common branching fractions and CP asymmetries in neutral and charged B decay channels, respectively. In summary, we can obtain 6 observables with fitting 7 $M_{\rm bc}$ distributions simultaneously using f_5. There are two advantages to use these functions compared to numerical calculation method. One is the systematic uncertainty for fitter can be canceled and got small, the other is we can obtain the correct systematic uncertainty without calculating the hard proportional of error.

7.3 Estimation of Wrong-tag Fraction

In the CP asymmetry measurement, we have to consider the events which are peaking components of combinatorial backgrounds and cross-feeds derived from opposite flavor of B meson, since these can induce CP asymmetry. The typical wrong-tag fraction source is double mis-PID events in $B^0 \to K^+\pi^-\gamma$. To extract peaking component of combinatorial background and cross-feeds, $M_{\rm bc}$ distributions combined these two type of backgrounds are fitted. Gaussian and ARGUS function are assigned for the PDFs of the peaking and other non-peaking components. Figure-7.3.1 show the $M_{\rm bc}$ distribution of combinatorial background and cross-feeds. The wrong-tag fraction is calculated by the ratio of peaking components and all of signal events, as a result we obtain 0.53% for $B^0 \to K^+\pi^-\gamma$ and zero for $B^+ \to K^{*+}\gamma$ decay.

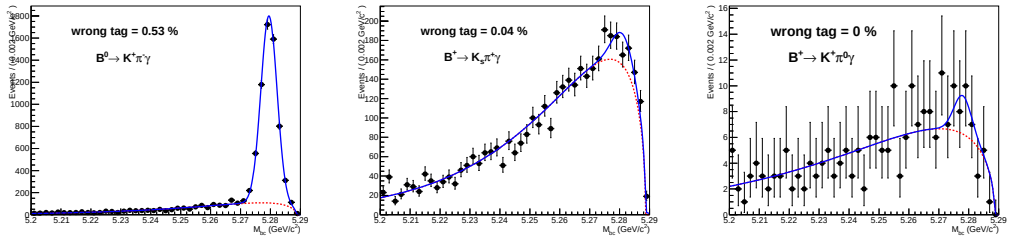

Figure 7.3.1: $M_{\rm bc}$ distributions of opposite flavor B meson in three channels.

7.4 ToyMC

50,000 toy MC fit is performed for checking the fitter bias. Signal yields are extracted by fitting for the sample which are generated from estimated PDFs and number of events are generated by random number generator based on Gaussian distribution. Then "pull" defined as

$$Pull = \frac{N_{toy} - N_{MC}}{\sigma_{toy}} \tag{7.4.0.16}$$

where N_{toy}, N_{MC} and σ_{toy} are measured variables, the standard model predictions of each measurement and fit error, are calculated. Figure-(7.6.1) shows the pull distributions for each observable. All pull distributions can be fitted by Gaussian with small deviation of the mean from zero in CP asymmetry, isospin asymmetry and ΔA_{CP}. The deviation of the mean is not small in the branching fractions measurements but fit bias is not so large because fit bias is calculated by

$$\text{Fit bias} = \frac{(\text{deviation of mean}) \times (\text{statistical error})}{(\text{Center value})}. \tag{7.4.0.17}$$

For example in $BF(B \to K_s\pi^0\gamma)$ whose deviation of mean is the largest in measured observables, -0.0985, and largest statistical uncertainty, 0.261×10^{-5}, in the study, the fit bias is assigned 0.6% with 4.33×10^{-5} of input parameter. Fit bias of the others parameters are smaller than 0.6% and these are listed in Table-7.5.1. Assumed input value of branching fractions are 4.33×10^{-5} for neutral and 4.21×10^{-5} for charged B decays, CP asymmetries and ΔA_{CP} are zero and isospin asymmetry is 5.07.

7.5 Linearity Check

We also check the linearity of the fitter using toy MC. For branching fractions, we float the input branching fractions within $\pm 5\sigma$ of their uncertainties in PDG in 20 steps. For CP asymmetries and isospin asymmetry, we define number of signal events such as

$$\begin{cases} \overline{N} = \dfrac{\overline{N}+N}{2}(1+A_{CP}) \\ N = \dfrac{\overline{N}+N}{2}(1-A_{CP}) \end{cases}, \tag{7.5.0.18}$$

$$\begin{cases} \overline{N} = \dfrac{\tau_{B^+}/\tau_{B^0}(1-\Delta_{0-})}{\tau_{B^+}/\tau_{B^0}(1-\Delta_{0-})+(1+\Delta_{0-})}(\overline{N}+N) \\ N = \dfrac{(1+\Delta_{0-})}{\tau_{B^+}/\tau_{B^0}(1-\Delta_{0-})+(1+\Delta_{0-})}(\overline{N}+N) \end{cases}, \tag{7.5.0.19}$$

where $\overline{N}$ and N mean number of events of $\overline{B}$ and B decaying to, and floating range of each variable are $\pm 100\%$ in 20 steps. Toy MC run corresponding to 3000 experiments and fitting by Gaussian are performed in each point and obtained means and errors with 1st order polynomial fitting are shown in Figure-7.6.2.

Calculated fit bias are summarized in Table-7.5.1. From these result, fit bias can be found in the branching fractions and little bias can be found in the CP asymmetries, isospin asymmetry and ΔA_{CP}. That of ΔA_{CP} is evaluated by sum of squares of CP asymmetries in neutral and charge B. These uncertainties are included in systematic uncertainty.

Measurement variables	Mean Dev. (ToyMC)	Linearity (%)	Fit bias (%)
BF($B^0 \to K_s\pi^0\gamma$)	-0.098 ± 0.005	2.348 ± 0.123	2.353
BF($B^0 \to K^+\pi^-\gamma$)	-0.033 ± 0.004	0.190 ± 0.033	0.193
BF($B^+ \to K_s\pi^+\gamma$)	-0.058 ± 0.005	-0.758 ± 0.051	0.762
BF($B^+ \to K^+\pi^0\gamma$)	-0.082 ± 0.005	1.122 ± 0.067	1.309
BF($B^+ \to K^{*+}\gamma$)	-0.084 ± 0.005	-0.131 ± 0.045	0.162
BF($B^0 \to K^{*0}\gamma$)	-0.043 ± 0.005	0.154 ± 0.039	0.165
$A_{CP}^{B^+\to K_s\pi^+\gamma}$	0.011 ± 0.005	0.038 ± 0.000	0.116
$A_{CP}^{B^+\to K^+\pi^0\gamma}$	-0.007 ± 0.005	-0.164 ± 0.012	0.164
$A_{CP}^{B^+\to K^{*+}\gamma}$	-0.001 ± 0.005	0.092 ± 0.000	0.092
$A_{CP}^{B^0\to K^{*0}\gamma}$	0.008 ± 0.005	0.069 ± 0.000	0.070
$A_{CP}^{B\to K^*\gamma}$	0.011 ± 0.004	0.081 ± 0.000	0.082
Δ_{0-}	0.036 ± 0.005	0.075 ± 0.006	0.083
ΔA_{CP}	-0.004 ± 0.005	0.115 ± 0.000	0.115

Table 7.5.1: The result of checking the fitter. mean whose Gaussian pull distribution fitted by Gaussian mean "Mean Dev." means the deviation of mean of Gaussian which is the fit function of pull distribution from zero. Fit bias come from this is calculated by Eq-7.4.0.17. The fit bias evaluated by linearity check are listed in the column of "Linearity". These are ratio of the absolute term at fitting by 1-st order polynomial to each center value. The row of fit bias shows the total uncertainty of these two checks.

7.6 Sensitivity Check

Using toy MC result, the sensitivity is estimated in this section. Table-(7.6.1) shows extracted signal yields and Table-(7.6.2) shows obtained branching fraction and CP asymmetry. Initial number of signal event is corrected by efficiency ratio and input branching fraction is $\mathcal{B}(B^0 \to K^{*0}\gamma) = 4.33 \times 10^{-5}$ and $\mathcal{B}(B^+ \to K^{*+}\gamma) = 4.21 \times 10^{-5}$ and CP asymmetries are assumed at zero. Since all of obtained values are close to input value, fitters can be worked correctly.

Decay mode	Input	Yields for toy MC
$K_s\pi^0\gamma$	393	391.5 ± 23.7
$K^+\pi^-\gamma$	5204	5201.7 ± 80.8
$K_s\pi^+\gamma$	1755	1753.1 ± 39.3
$K^+\pi^0\gamma$	1241	1239.1 ± 27.8

Table 7.6.1: Summary of toy MC fit result for obtaining each branching fraction run. All of obtained values are close to input values.

Channel	$\mathcal{B}(\times 10^{-5})$	$\mathcal{B}^{combined}(\times 10^{-5})$	A_{CP}	$A_{CP}^{combined}$
$K_s\pi^0\gamma$	4.31 ± 0.26	-	-	-
$K^+\pi^-\gamma$	4.33 ± 0.07	4.33 ± 0.07	0.000 ± 0.016	0.000 ± 0.016
$K_s\pi^+\gamma$	4.21 ± 0.13	-	0.000 ± 0.029	-
$K^+\pi^0\gamma$	4.20 ± 0.16	4.20 ± 0.09	0.000 ± 0.037	0.000 ± 0.023

Table 7.6.2: Obtained branching fraction ($\mathcal{B}$), combined one ($\mathcal{B}^{combined}$) and CP asymmetry (A_{CP}) at "MC" sample. First value is measured value, second one is statistical error.

Obtained CP asymmetry combined three channels, ΔA_{CP} and isospin asymmetry are

$$A_{CP} = 0.000 \pm 0.013(stat.) \quad (7.6.0.20)$$
$$\Delta A_{CP} = 0.000 \pm 0.027(stat.) \quad (7.6.0.21)$$
$$\Delta_{0-} = 0.051 \pm 0.014(stat.), \quad (7.6.0.22)$$

and these are consistent to input or standard model prediction.

Figure-7.6.3 shows the fitted $M_{\rm bc}$ distribution of one of toy MC for obtaining isospin asymmetry.

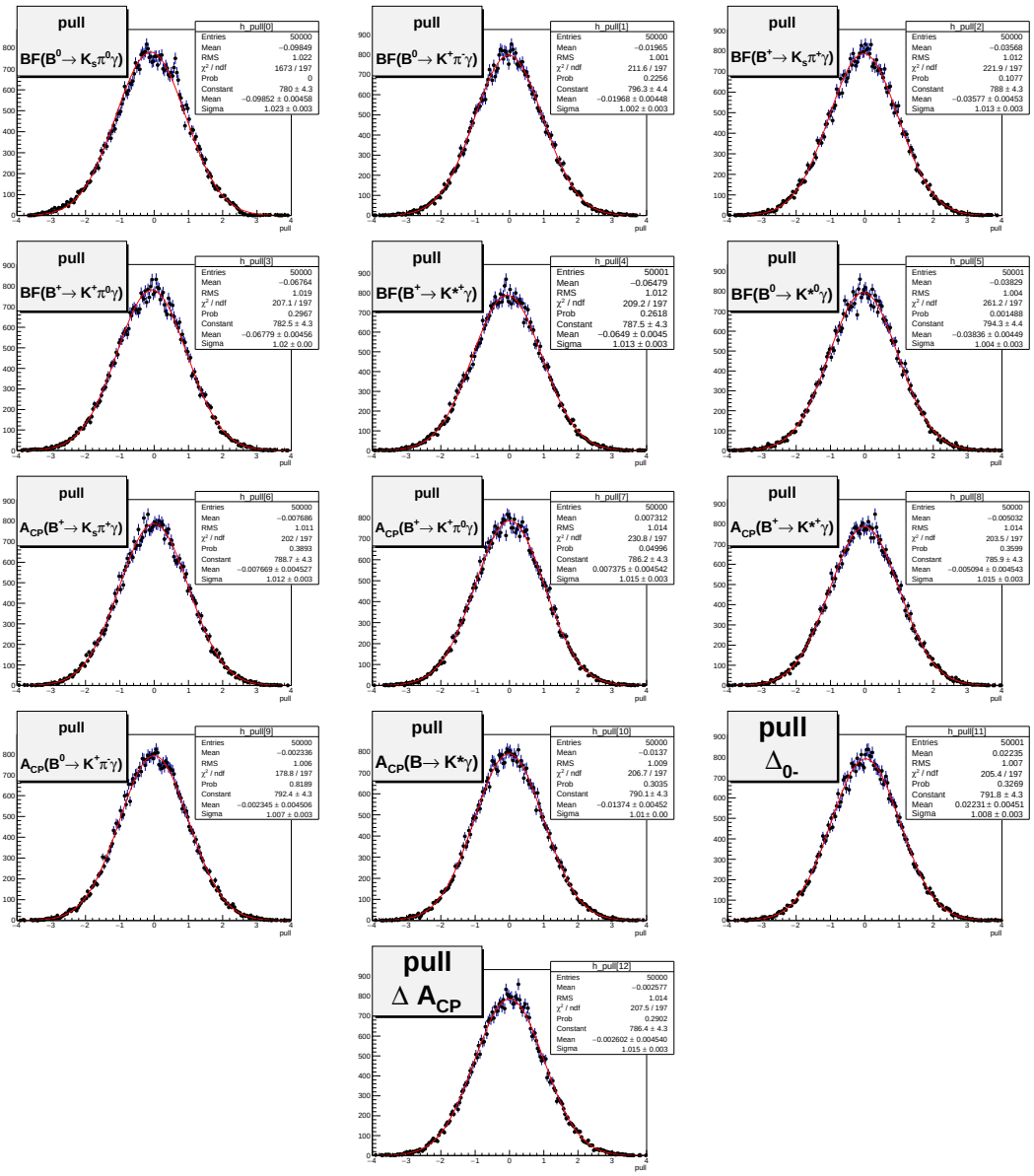

Figure 7.6.1: Pull distribution fitted by Gaussian

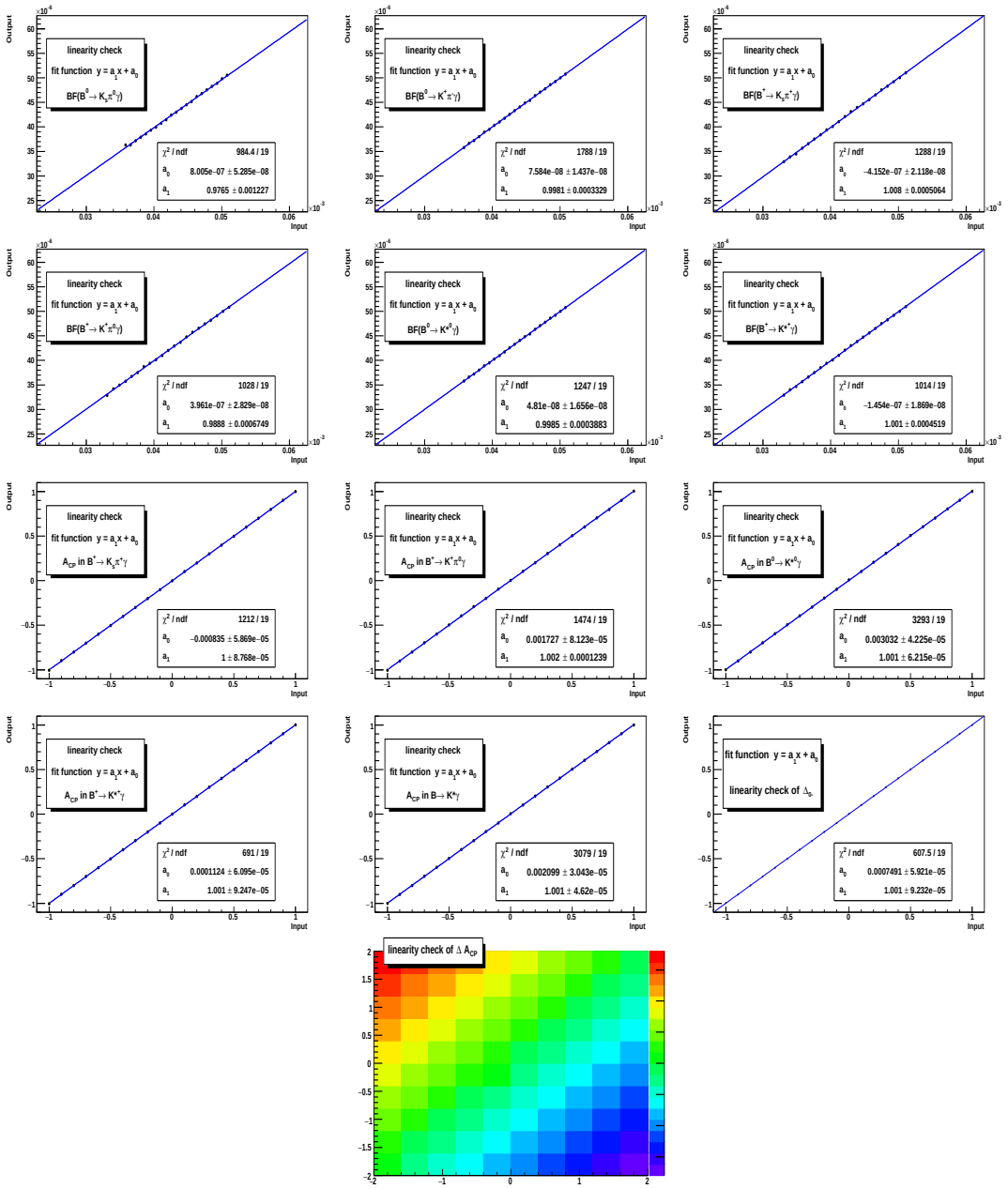

Figure 7.6.2: Linearity check of the fitter for the branching fraction, CP asymmetries, isospin asymmetry and ΔA_{CP}. The bottommost figure shows the linearity of ΔA_{CP}. The x- and y-axis in this figure show the input value of $A_{CP}^{B^+}$ and $A_{CP}^{B^0}$ and calculated ΔA_{CP}s are filled in bins of the 2D figure.

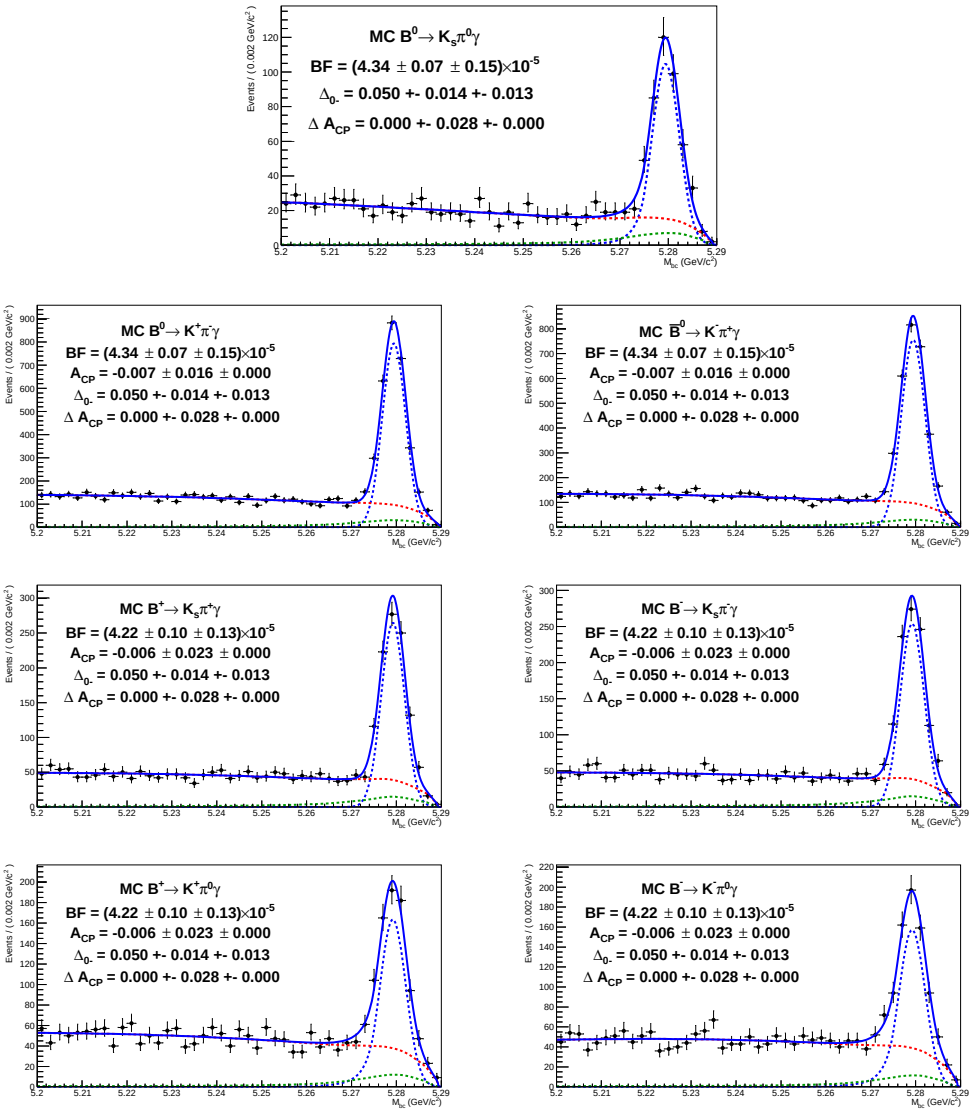

Figure 7.6.3: The $M_{\rm bc}$ distributions of one of the toy MC fitting when using Eq-(7.2.0.15) are shown. Blue solid line is sum of all components, blue dashed line is signal, red dashed line is qq bkg, green dashed line is sum of B decay background.

Chapter 8

Systematic Uncertainty

We check the difference between MC and real data, which is used for the MC sample correction and treated as systematic uncertainty. In this analysis, the amount of data, the reconstruction efficiency of the particles forming B meson, background suppression, and fit uncertainties are considered. All of systematic uncertainty sources are summarized in Table-8.0.1.

Source	$K_s\pi^0\gamma$	$K^+\pi^-\gamma$	$K_s\pi^+\gamma$	$K^+\pi^0\gamma$
Reconstruction efficiency (%)	1.247 ± 0.004	16.440 ± 0.015	5.366 ± 0.009	3.847 ± 0.007
Number of B meson pairs	1.37	1.37	1.37	1.37
Photon Selection	2.0	2.0	2.0	2.0
Tracking efficiency	-	0.70	0.35	0.35
K^+/π^+ identification	-	1.65	0.80	0.84
K_s reconstruction	1.14	-	1.14	-
π^0 reconstruction	1.27	-	-	1.27
$M(K\pi)$ uncertainty	0.11	0.11	0.11	0.11
Neurobayes + π^0/η veto	0.56	0.56	0.56	0.56
Detector response	-	0.19	0.37	0.33
Fit bias (PDF uncertainty)	2.35	0.19	0.76	1.31
f_{+-}/f_{00}	1.2	1.2	1.2	1.2
wrong-tag fraction	0.05	0.05	0.05	0.05

Table 8.0.1: The list of reconstruction efficiency (%) and systematic uncertainty (%) for branching fraction. Detector response means the difference of detector response between positive and negative track.

8.1 Number of B Mesons

The method for counting $B\overline{B}$ pairs is the amount of data accumulated on the operating on the $\Upsilon(4S)$ resonance subtracted the data operated out of $\Upsilon(4S)$ resonance [30]. The equation for calculating can be described as

$$N_{B\overline{B}} = \frac{N_{\Upsilon(4S)} - \alpha r(\epsilon_{q\bar{q}})N_{q\bar{q}}^{off}}{\epsilon_{B\overline{B}}}, \tag{8.1.0.1}$$

where $N_{\Upsilon(4S)}$ is the number of events satisfying the hadronic event selection which is tuned for rejecting background event such as Bhabha and two photon process, at on-resonance data, $r(\epsilon_{q\bar{q}})$ is the ratio of efficiency for $q\bar{q}$ events at off-resonance to one for those at on-resonance, α is the ratio of number of Bhabha events or μ pair events observed at on-resonance to those observed at off-resonance. $N_{q\bar{q}}^{off}$ is the number of events satisfying the hadronic event selection in the off-resonance data and $\epsilon_{B\overline{B}}$ is the efficiency of the $\Upsilon(4S) \to B\overline{B}$ event satisfying the selection criteria for on-resonance data.

The systematic uncertainty for number of B mesons is dominated by α, which is the scaling factor for comparing off- and on- resonance data in Eq-8.1.0.1. Belle group evaluates the number of B meson pairs as $(771.85\pm10.57)\times10^6$ therefore 1.37% of systematic uncertainty is assigned.

8.2 Photon Selection Efficiency

The detection efficiency of prompt photon is measured using radiative Bhabha events, $e^+e^- \to e^+e^-\gamma$ [52]. The missing 4-vector assuming photon is calculated after reconstructing two tracks with electron identification. Selection conditions for missing 4-vector are in barrel region, $33^\circ < \theta_{miss} < 128^\circ$ where θ_{miss} is the polar angle of missing 4-vector, $-0.3 < m^2_{miss} < 0.2$ $(\mathrm{GeV}/c^2)^2$ where m^2_{miss} is squared value of missing mass and the energy range of missing from 2 to 3 GeV. The systematic uncertainty is evaluated as 2.0% from the comparison of peak shifting between MC and real data of the distribution of $E_{photon}/E_{missing}$ where E_{photon} is photon candidate energy detected in ECL and $E_{missing}$ is missing energy and $\Delta E(= E_{photon} - E_{missing})$.

8.3 Tracking Efficiency

The systematic uncertainty for the high momentum ($p_t > 200$ MeV/c) charged particle tracking is evaluated by using the decay chain of $D^* \to D^0\pi, D^0 \to \pi^+\pi^- K_s$ and $K_s \to \pi^+\pi^-$, which provides a clean sample by mass difference selection between D^* and D^0 with sufficient statistics [53]. The decay can be reconstructed without actually detecting one of the pions from the K_s decay. The four-momentum of slow pion can be calculated from the kinematic constraints of the decay chain. The ratio of the yield of such partially reconstructed D^* to those fully reconstructed with both pions from the K_s is the track reconstruction efficiency. We calculate the result as (99.87 ± 0.32)% and assign 0.35 % per a track.

8.4 K/π Identification

Similar to performance check for K/π identification in Section-4.2, the decay of $D^{*+} \to D^0\pi^+$, $D^0 \to K^-\pi^+$ is used for systematic uncertainty estimation. Systematic uncertainty depends on momentum range of charged particles and selection tightness, so the difference between MC and real data is estimated for each selection [54]. In this analysis, the calculated efficiency ratios are summarized in Table 8.4.1.

8.5 K_s Reconstruction Efficiency

Past K_s reconstruction tool in Belle is "goodKs" [55]. Using goodK_s we evaluated the K_s candidates whether ones have good quality or not. The range of momentum of K_s (p_{K_s}) which is the parameter that K_s reconstruction efficiency depends on is divided into three, p_{K_s} <0.5 , $0.5 < p_{K_s} < 1.5$ and $1.5 < p_{K_s}$ GeV/c^2. Used cut values are the smallest approach from the

efficiency ratio (%)	$K^+\pi^-\gamma$	$K_s\pi^+\gamma$	$K^+\pi^0\gamma$
Kaon ID	99.22 ± 0.84 %	-	99.50 ± 0.84 %
Pion ID	97.74 ± 0.81 %	97.69 ± 0.80 %	-
Total	96.98 ± 1.65 %	97.69 ± 0.80 %	99.50 ± 0.84 %

Table 8.4.1: Systematic uncertainty list for K/π identifications

IP to the track in x-y plane (dr), distance between the two daughter tracks at their interaction point (z_{dist}), azimuthal angle between the momentum vector and the decay vertex vector of K_s candidate ($d\phi$) and flight length of K_s candidate in x-y axis (fl). In 2012 nisK_s finder which is the latest K_s finder in Belle and using Neurobayes technique was developed. To improve the reconstruction efficiency, new parameters used for training such as likelihood ratio between π and proton using hit information of ACC, TOF and CDC, hit information in SVD and CDC and sine of the angle between two $\pi\pm$s were added into the parameters of *good*K_s. The performances of K_s reconstruction efficiency using goodK_s and nisK_s are 76.9 % and 86.9 % [41].

8.5.1 Analysis Strategy for the Estimation of Systematic Uncertainty

The analysis method is almost same as K_s systematic uncertainty estimation method in BaBar [56]. Firstly, we define the ranges of the parameters, fl, cosine of the polar angle of K_s direction in laboratory frame ($\cos\theta_{K_s}$) and transverse momentum of K_s (pt_{K_s}) which K_s efficiency depends on. The range of fl is decided based on the Belle detector geometry, 0.15 – 1.2 – 3.0 – 4.55 – 6.05 – 8.8 – (cm) for SVD1 data and 0.15 – 1.2 – 2.0 – 4.35 – 7.00 – 8.8 – (cm) for SVD2 data, and those of $\cos\theta_{K_s}$ and pt_{K_s} are decided like -0.867 – -0.450 – 0.113 – 0.639 – 0.956 and 0.0 – 0.5 – 1.0 – 1.5 – (GeV/c). Secondly, efficiency (ϵ_{ijk}) and efficiency ratios (R_{ijk}) which are defined as

$$\epsilon_{ijk}^{\mathrm{MC/RD}} = N_{ijk}^{\mathrm{MC/RD}} / N_{\mathbf{1}jk}^{\mathrm{MC/RD}}, \quad (8.5.1.1)$$

$$R_{ijk} = \epsilon_{ijk}^{\mathrm{RD}} \ / \ \epsilon_{ijk}^{\mathrm{MC}}, \quad (8.5.1.2)$$

where i, j and k mean the bin number of fl, $\cos\theta_{K_s}$ and $p_{t_{K_s}}$ and N is extracted signal yield, are calculated. The denominator of efficiency is the 1st bin of fl used as normalization. Efficiency ratio of two pions decayed from K_s is (99.87± 0.32)% (section-8.3) with the requirement of smaller then 3.0 cm of fl, therefore this is good agreement to use the 1st bin of fl as a normalization factor. Finally, efficiency ratio is calculated by weighted summation of efficiency ratio of all bins.

We reconstruct $D^{*+} \to D^0\pi_s^+$, $D^0 \to K_s\pi^+\pi^-$, where π_s^+ means slow pion. Clean K_s candidates can be extracted by this mode with tight mass difference cut defined in Eq-8.5.1.3. Since nisK_s and goodK_s consider only $K_s \to \pi^+\pi^-$ channel, we do not use $K_s \to \pi^0\pi^0$. For charged pion candidates including slow pion, the distance from IP in x-y plane for $|dr| < 0.2$ cm and z-axis for $|dz| < 2.0$ cm, the likelihood ratio value of K/π identification for $\mathcal{LR}_{\pi/K} > 0.6$ and at least one hit in SVD and CDC are required. K_s candidates are selected from V-particle candidates list table with applying good quality nisK_s or goodK_s selection. D^0 meson is reconstructed by combining two pion candidates and a K_s candidate and D^0 candidates whose masses are grater than 1.93 GeV/c^2 or less than 1.80 GeV are excluded. D^{*+} candidates are reconstructed by pairing D^0 and a slow charged pion candidate. To reject the background from B meson decay, only high momentum D^{*+} candidates are used here we require $p_{D^*} > 2.5$ GeV/c^2 in the center of mass

system. Finally, to suppress a lot of backgrounds and select clean D^* events we require tight mass difference (M_{dif}) cut $|M_{dif} - 0.00585| < 0.0015$ GeV/c^2 here M_{dif} is defined as

$$M_{dif} = m_{D^{*+}} - m_{D^0} - m_{\pi^+} \tag{8.5.1.3}$$

If multi-candidates exit in a events, we select the candidate whose M_{dif} value is the closest to nominal value. Figure-8.5.1 show the distributions of K_s mass, D^0 mass, mass difference of K_s, transverse momentum of K_s, cosine of angle against z-axis and flight length.

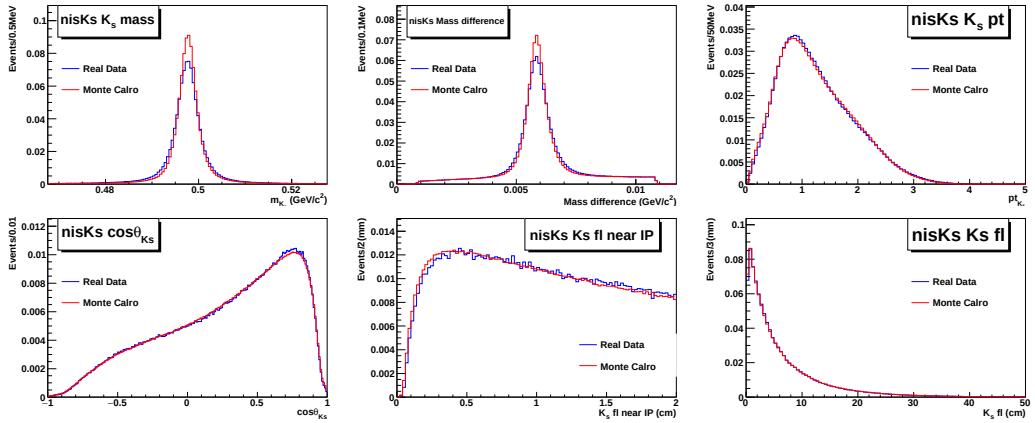

Figure 8.5.1: K_s mass, mass difference, K_s transverse momentum, $\cos\theta_{K_s}$ (lab.), flight length near IP and flight length distributions with nisK_s selection

8.5.2 Fitting and Calculating Efficiency Ratio

To extract signal yields, unbinned maximum likelihood fitting for K_s mass distribution is performed for each bin. However, we exclude the bins which have less than 1000 events and are treated as physically less important. For example, the bin with decaying in CDC, $fl > 8.8$ cm, near the edge of backward acceptance, $cos\theta_{K_s} \sim -0.866$ (;$\theta_{lab.} \sim 150$ degree), and low pt ($pt_{K_s} < 0.5$) is strongly suppressed in the energy scale of Belle. Figure-8.5.2 shows the two dimensional histogram between $cos\theta_{K_s}$ and pt_{K_s} for each fl bin. Assigned PDFs for signal and background are Bifurcated Gaussian added Gaussian and 1st order Chebyshev. Here all fit parameters and signal and background yields are floated. Figure-8.5.3 shows the fitted figures.

The fit region and signal box in which we extract the signal yield are defined as ± 30 and ± 10 MeV/c^2 around nominal K_s mass. The reason of making signal box is that due to arise long tail in K_s mass distribution, performance of signal extraction in signal box is better than fit region. Correctness of signal extraction is checked by calculation of the ratio of extracted signal yields and MC truth and this can be found in Appendix-11.4. In a lot of bins, signal yields are extracted within 1% uncertainty and some bins in which extracted signal yields are much larger than one have small number of events.

The uncertainty of efficiency ratio (σ_{ijk}) for each bin, weighted efficiency ratio (R) and uncertainty (σ) are given as

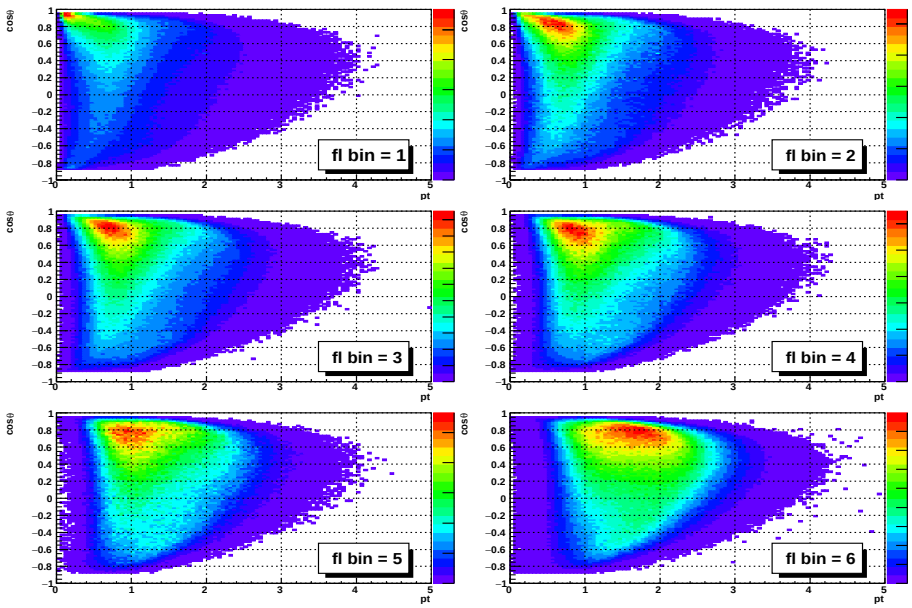

Figure 8.5.2: Two dimensional histograms for each fl bin.

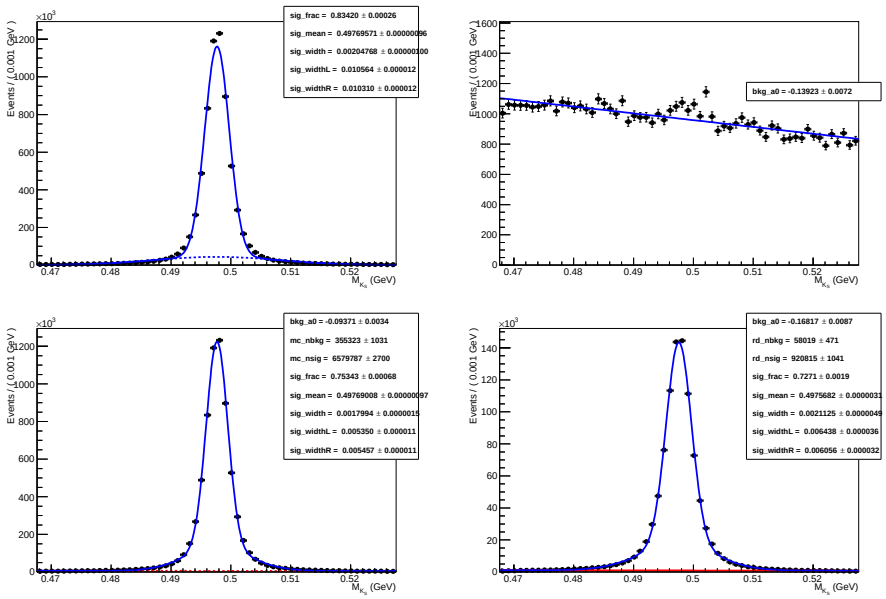

Figure 8.5.3: The K_s mass distributions with fitting and nisK_s selection. Left top figure is signal, right top figure is background, left bottom is signal + background on MC sample and right bottom figure is the real data sample.

$$\sigma_{ijk} = R_{ijk}\sqrt{(\sigma_{N^{\rm MC}_{ijk}}/N^{\rm MC}_{ijk})^2 + (\sigma_{N^{\rm RD}_{ijk}}/N^{\rm RD}_{ijk})^2}, \quad (8.5.2.1)$$

$$R = \sum_{ijk}\frac{R_{ijk}}{\sigma^2_{ijk}} \;/\; \sum_{ijk}\sigma^2_{ijk}, \quad (8.5.2.2)$$

$$\sigma = \frac{1}{N^{\rm MC}_{total}}\sum_{jk}\sqrt{\sum_i N^{\rm MC}_{ijk}R^2_{ijk} + \sum_{i\neq 1}(N^{\rm MC}_{ijk}\sigma_{ijk})^2 + (\sum_{i\neq 1}N^{\rm MC}_{ijk}R_{ijk}\sigma_{\mathbf{1}jk})^2} \quad (8.5.2.3)$$

where MC and RD mean Monte Carlo and real data, index of i, j and k mean the bin of fl, $\cos\theta_{K_s}$ and pt_{K_s}, respectively. The first term of Eq-8.5.2.3 depends on the signal MC sample statistics, the second term shows the statistical uncertainty corrected by MC sample size for each bin, and the third term represents the statistical uncertainty of normalization. This fitting and calculation are done in two types of sample, the data set of SVD1 and 2. The results are summarized in Table-8.5.1. As a result, considering the systematic uncertainty of tracking efficiency, 0.35% par a track, 100.08% and 1.16% are assigned for efficiency correction and systematic uncertainty.

Selection	SVD1	SVD2	Total
nisK_s	98.76 ± 2.42	100.30 ± 1.00	100.08 ± 0.92
goodK_s	99.22 ± 2.51	99.62 ± 1.09	99.55 ± 1.00

Table 8.5.1: Efficiency ratio for nisK_s and goodK_s list

8.6 π^0 Reconstruction

The difference of π^0 reconstruction efficiency between MC and real data is come from imperfect modeling of the material distribution in ECL and the photon shower shape [57]. The reconstruction sub-decay modes are $\eta \to \gamma\gamma$ and $\eta \to \pi^0\pi^0\pi^0$. Therefore systematic uncertainty is estimated by defining the efficiency as $\epsilon = N(\eta \to \pi^0\pi^0\pi^0)/N(\eta \to \gamma\gamma)$. Obtained efficiency ratio is $R = (95.3\pm0.9\pm0.9)$, so we assigned 95.3% for efficiency correction and 1.27% for systematic uncertainty.

8.7 $M(K\pi)$ Background Estimation Come from Higher Kaonic Resonance

To estimate the amount of the contribution from higher kaonic resonance, $M(K\pi)$ distribution is fitted. K^* mass spectrum can be represented by relativistic P-wave relativistic Breit-Wigner amplitude. In the Dalitz analysis of $D^0 \to K^-\pi^+\pi^0$ published by CLEO group, the amplitude of $D^0 \to \overline{K}^*\pi^0, \overline{K^*} \to K^-\pi^+$ is written by P-wave relativistic Breit-Wigner amplitude [51]. This amplitude depends on the invariant masses, $M(K^-\pi^+)$ and $M(K^-\pi^0)$. In this analysis, we use the amplitude canceled $M(K^-\pi^0)$ for $M(K\pi)$ fitting.

Here we use same notations in CLEO's paper [51] and modify it. In CLEO's paper, three body decay is considered, which is represented as the decay chain that mother particle "D" decays into the particle "A", "B" and "C". When the particles of A and B make a spin-1 resonance, the decay amplitude is defined as

$$\mathcal{M}_{\rm BW}(M_{AB}, M_{AC}) = F_D F_r \frac{M^2_{AC} - M^2_{BC} + (M^2_D - M^2_C)(M^2_B - M^2_A)}{M^2_r - M_{AB} - iM_r\Gamma_{AB}}, \quad (8.7.0.4)$$

where F_D and F_r are the mass and spin dependent form factors, which is so-called Blatt-Weisskopf form factors defined in Table 8.7.1, of mother particle D and resonance particle "r" formed by A and B, M_{AB} is the invariant mass of A and B, M_A is the mass of A, and Γ_{AB} is the mass dependent width of AB system defined as

$$\Gamma_{AB} = \Gamma_r \left(\frac{p_{AB}}{p_r} \right)^{2J+1} \frac{M_r}{M_{AB}} \cdot F_r^2, \tag{8.7.0.5}$$

where p_{AB} is the momentum of A and B in the rest frame of AB.

Spin	Form factor
0	1
1	$\sqrt{\frac{1+R^2p_r^2}{1+R^2p_{AB}^2}}$
2	$\sqrt{\frac{9+3R^2p_r^2+R^4p_r^4}{9+3R^2p_{AB}^2+R^4p_{AB}^4}}$

Table 8.7.1: Table of Blatt-Weisskopf form factors. R is meson radial parameter. p_{AB} is the momentum of either daughter in the rest frame. p_r is the meson mass.

When this amplitude is applied to the decay of $B \to K^*\gamma, K^* \to K\pi$, the particle A, B, C, D and resonance "r" are corresponded to K, π, γ, B meson and K^*, respectively. The $K\pi$ mass spectrum is calculated by the square of amplitude of $M_{K\gamma}$,

$$f_{BW}(M_{K\pi}) \propto \int_{M^2_{K\gamma}|_{min}}^{M^2_{K\gamma}|_{max}} |\mathcal{M}_{BW}(M_{K\pi}, M_{K\gamma})|^2 \cdot 2M_{K\pi} dM^2_{K\gamma} \tag{8.7.0.6}$$

where $M^2_{K\gamma}|_{min} = (E^*_K + E^*_\gamma)^2 - (p^*_K + p^*_3)^2$, $M^2_{K\gamma}|_{max} = (E^*_K + E^*_\gamma)^2 - (p^*_K - p^*_3)^2$, $E^*_K = (M^2_{K\pi} + M^2_K - M^2_\pi)/(2M_{K\pi})$, $E^*_\gamma = (M^2_B - M^2_{K\pi})/(2M_{K\pi})$, $(p^*_{K,\gamma})^2 = (E^*_{K,\gamma})^2 - M^2_{K,\gamma}$.

Signal yields are extracted by $M_{\rm bc}$ fit every 30 MeV step of $M(K\pi)$ window from 0.65 to 2.0 GeV and $M(K\pi)$ distribution is made by filling them. The main background source is $X_s\gamma$ bkg such as K^*_2 and non-resonant components.

Figure-8.7.1 shows the distributions of $M_{K\pi}$ distributions for each decay. The amount of higher resonance for some $M_{K\pi}$ window are found in Table-8.7.2. Signal yields extracted by $M(K\pi)$ fitting are consistent to signal yields extracted by $M_{\rm bc}$ listed in Table-9.1.1 fitting within 1 σ. From this table, assigned systematic uncertainty for all of the decay channels is assigned as 0.11%.

8.8 Neurobayes Selection and π^0/η Veto

8.8.1 Analysis Strategy

The systematic uncertainty of $q\bar{q}$ bkg suppression and π^0/η veto is estimated by using the decay of $B \to D\pi^+$. Input parameters of Neurobayes training for $q\bar{q}$ bkg suppression represent the event shape except $q \cdot r$. In the $B \to D\pi^+$ decay, if π^+ decayed from B meson directory, here this pion is named "fast pion" (π_f), is treated as prompt photon in $B \to K^*\gamma$, since the kinematics of D

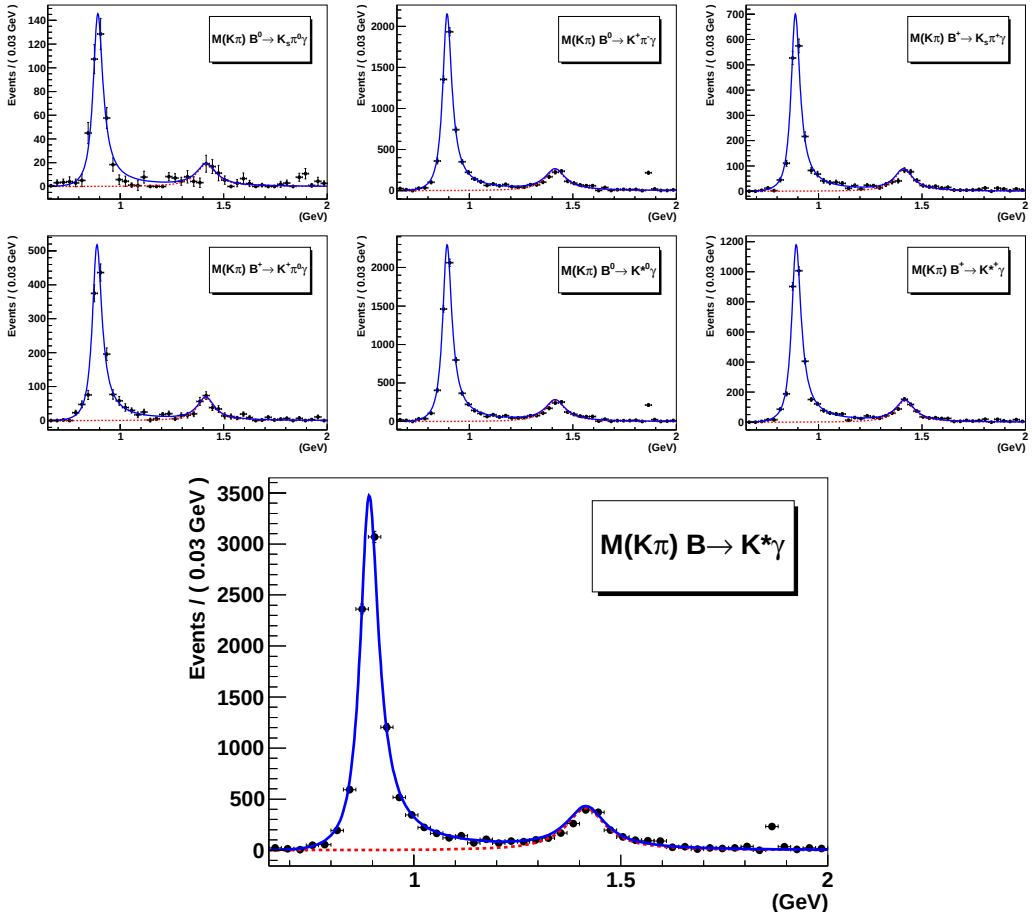

Figure 8.7.1: The $M(K\pi)$ distributions whose data set is real data fitted by P-wave Breit-Wigner function. The peak near the 1.86 GeV/c^2 is the decay of $D \to K\pi$.

Rec. Channel	Window	N signal yields	$M(K\pi)$ bkg. yields	Bkg. Fraction
$B^0 \to K_s\pi^0\gamma$	75 MeV	335.2 ± 17.3	0.4 ± 0.0	0.11 %
	80 MeV	340.9 ± 17.6	0.4 ± 0.1	0.12 %
	90 MeV	350.5 ± 18.1	0.5 ± 0.1	0.13 %
	100 MeV	358.3 ± 18.5	0.5 ± 0.1	0.15 %
$B^0 \to K^+\pi^-\gamma$	75 MeV	4735.1 ± 63.5	5.6 ± 0.2	0.12 %
	80 MeV	4810.7 ± 64.5	6.0 ± 0.2	0.13 %
	90 MeV	4938.8 ± 66.2	6.9 ± 0.2	0.14 %
	100 MeV	5043.0 ± 67.6	7.9 ± 0.2	0.16 %
$B^+ \to K_s\pi^+\gamma$	75 MeV	1511.8 ± 35.9	1.4 ± 0.1	0.09 %
	80 MeV	1535.4 ± 36.4	1.5 ± 0.1	0.10 %
	90 MeV	1575.2 ± 37.4	1.8 ± 0.1	0.11 %
	100 MeV	1607.7 ± 38.1	2.0 ± 0.1	0.12 %
$B^+ \to K^+\pi^0\gamma$	75 MeV	1167.1 ± 31.2	1.0 ± 0.1	0.08 %
	80 MeV	1186.4 ± 31.8	1.1 ± 0.1	0.09 %
	90 MeV	1219.0 ± 32.6	1.2 ± 0.1	0.10 %
	100 MeV	1245.5 ± 33.3	1.4 ± 0.1	0.11 %
$B^0 \to K^{*0}\gamma$	75 MeV	5051.7 ± 65.7	5.8 ± 0.2	0.12 %
	80 MeV	5132.4 ± 66.7	6.3 ± 0.2	0.12 %
	90 MeV	5269.0 ± 68.5	7.2 ± 0.2	0.14 %
	100 MeV	5380.0 ± 69.9	8.2 ± 0.2	0.15 %
$B^+ \to K^{*+}\gamma$	75 MeV	2640.9 ± 47.2	2.6 ± 0.1	0.10 %
	80 MeV	2684.1 ± 48.0	2.8 ± 0.1	0.10 %
	90 MeV	2757.3 ± 49.3	3.2 ± 0.1	0.12 %
	100 MeV	2816.9 ± 50.4	3.6 ± 0.2	0.13 %
$B \to K^*\gamma$	75 MeV	7692.7 ± 80.9	8.4 ± 0.2	0.11 %
	80 MeV	7816.6 ± 82.2	9.1 ± 0.2	0.12 %
	90 MeV	8026.5 ± 84.4	10.4 ± 0.3	0.13 %
	100 MeV	8197.2 ± 86.2	11.8 ± 0.3	0.14 %

Table 8.7.2: Table of Blatt-Weisskopf form factors. R is meson radial parameter. p_{AB} is the momentum of either daughter in the rest frame. p_r is the meson mass.

meson decay is similar to that of K^* decay, we can regard $B \to D\pi^+$ as a good control sample for $B \to K^*\gamma$. For the $q \cdot r$, since flavor is determined by information of B^0 which is not signal side, bias should not arise. In the systematic study of π^0/η veto, likelihood ratio for π^0 and η is calculated by combining the three vector of photon candidate and $modified\ \pi_f$, which three vector of $modified\ \pi_f$ is calculated by assigning mass less. We evaluate the systematic uncertainty by analyzing the decay of $B \to D\pi^+$ and calculating the efficiency ratio using obtained signal yields.

8.8.2 Reconstruction

In this study, we consider two sub-decay channels, $B^0 \to D^-\pi_f^+, D^- \to K^+\pi^-\pi^-$ and $B^+ \to D^0\pi_f^+, D^0 \to K^-\pi^+$. For reconstructing them, charged pions and kaons are selected based on the same selection criteria in $B \to K^*\gamma$ analysis (Table-5.5.1) is used. For π_f treated as prompt photon, we require the same selection of prompt photon except E9/E25. Instead of $M_{K\pi}$ selection, we require 10 MeV/c^2 of D meson mass window around nominal D meson mass. Since energy leakage at photon detection is nothing, we require the tight ΔE window, which is $\pm$20 MeV around zero.

8.8.3 Fit and Result

The efficiency is defined as the ratio of the signal yields of before to after background suppression. Signal yields are extracted by unbinned maximum likelihood fitting of $M_{\rm bc}$. The PDF for signal sample, continuum background and B decay background are assigned to Gaussian, ARGUS function defined in Eq-7.1.0.3 and Gaussian added ARGUS function, respectively. Fixed parameters are the end point of ARGUS function in continuum PDF and the shape and number of events of B decay background. The amount of B decay background are 1.5% and 0.8% of signal for neutral and charged B decay and their main sources are combinatorial backgrounds. The effect of this background is included in systematic uncertainty. Figure-8.8.1 show the fitted $M_{\rm bc}$ distribution before both $\pi^0\eta$ veto and selection with Neurobayes and after applying their selections. We calculate efficiencies and efficiency ratios for Neurobayes selection, π^0/η veto applying both of two selections and these are summarized in Table-8.8.1. Systematic uncertainty source of this analysis is only fit bias, two fixed parameters. We estimate the uncertainty by floating $\pm1\sigma$ of end point of ARGUS function in continuum background and $\pm$100% of number of B decay background. The result of two channels are combined and calculated as R = 97.53 ± 0.56%. We assign 97.53% to efficiency correction and 0.56% to systematic uncertainty.

8.9 Fit Bias

Fit bias is come from fitter uncertainty. Fitter uncertainty is estimated by toy Monte Carlo study which is written in section-7.4 and bias is evaluated by the deviation of mean of pull distribution. Fit bias is summarized in Table-7.5.1.

8.10 Uncertainties from Fixed Parameters

In order to stabilize the fitting, some parameters are fixed in signal extraction and these can be made uncertainty.

Fixed parameters in signal extraction are summarized in Table-7.1.1. Due to small number of events, the bias for signal extraction from fixed shape parameters on the PDFs of BB-general, rare$B$, $X_s\gamma$, combinatorial background and cross-feeds should be negligible. Therefore systematic

Decay channel		efficiency (%)	efficiency ratio (%)
Neurobayes Selection			
$B^0 \to K_s\pi^0\gamma$	MC	84.63 ± 0.11	-
$B^0 \to K^+\pi^-\gamma$	MC	83.37 ± 0.03	-
$B^+ \to K_s\pi^+\gamma$	MC	83.14 ± 0.05	-
$B^+ \to K^+\pi^0\gamma$	MC	84.13 ± 0.06	-
$B^0 \to D^+\pi^-$,	MC	86.80 ± 0.23	99.07 ± 0.73 ± 0.14
$D^+ \to K^-\pi^+\pi^+$	RD	86.00 ± 0.59	
$B^+ \to D^0\pi^+$,	MC	86.14 ± 0.24	99.12 ± 0.76 ± 0.05
$D^0 \to K^-\pi^+$	RD	85.38 ± 0.61	
π^0/η veto			
$B^0 \to K_s\pi^0\gamma$	MC	91.88 ± 0.08	-
$B^0 \to K^+\pi^-\gamma$	MC	91.89 ± 0.02	-
$B^+ \to K_s\pi^+\gamma$	MC	91.52 ± 0.04	-
$B^+ \to K^+\pi^0\gamma$	MC	91.62 ± 0.05	-
$B^0 \to D^+\pi^-$,	MC	87.69 ± 0.23	98.22 ± 0.74 ± 0.12
$D^+ \to K^-\pi^+\pi^+$	RD	86.13 ± 0.60	
$B^+ \to D^0\pi^+$,	MC	87.63 ± 0.25	98.42 ± 0.76 ± 0.04
$D^0 \to K^-\pi^+$	RD	86.24 ± 0.62	
Neurobayes Selection + π^0/η veto			
$B^0 \to K_s\pi^0\gamma$	MC	77.78 ± 0.12	-
$B^0 \to K^+\pi^-\gamma$	MC	76.61 ± 0.03	-
$B^+ \to K_s\pi^+\gamma$	MC	76.09 ± 0.06	-
$B^+ \to K^+\pi^0\gamma$	MC	77.08 ± 0.07	-
$B^0 \to D^+\pi^-$,	MC	76.99 ± 0.21	97.42 ± 0.75 ± 0.24
$D^+ \to K^-\pi^+\pi^+$	RD	75.00 ± 0.54	
$B^+ \to D^0\pi^+$,	MC	76.37 ± 0.22	97.64 ± 0.78 ± 0.08
$D^0 \to K^-\pi^+$	RD	74.57 ± 0.56	

Table 8.8.1: Efficiency and efficiency ratio list for continuum suppression and π^0/η veto. The uncertainty of efficiency is statistical one, and former and latter uncertainty of efficiency ratio are statistical and systematic uncertainty in this $B \to D\pi^+$ study, respectively.

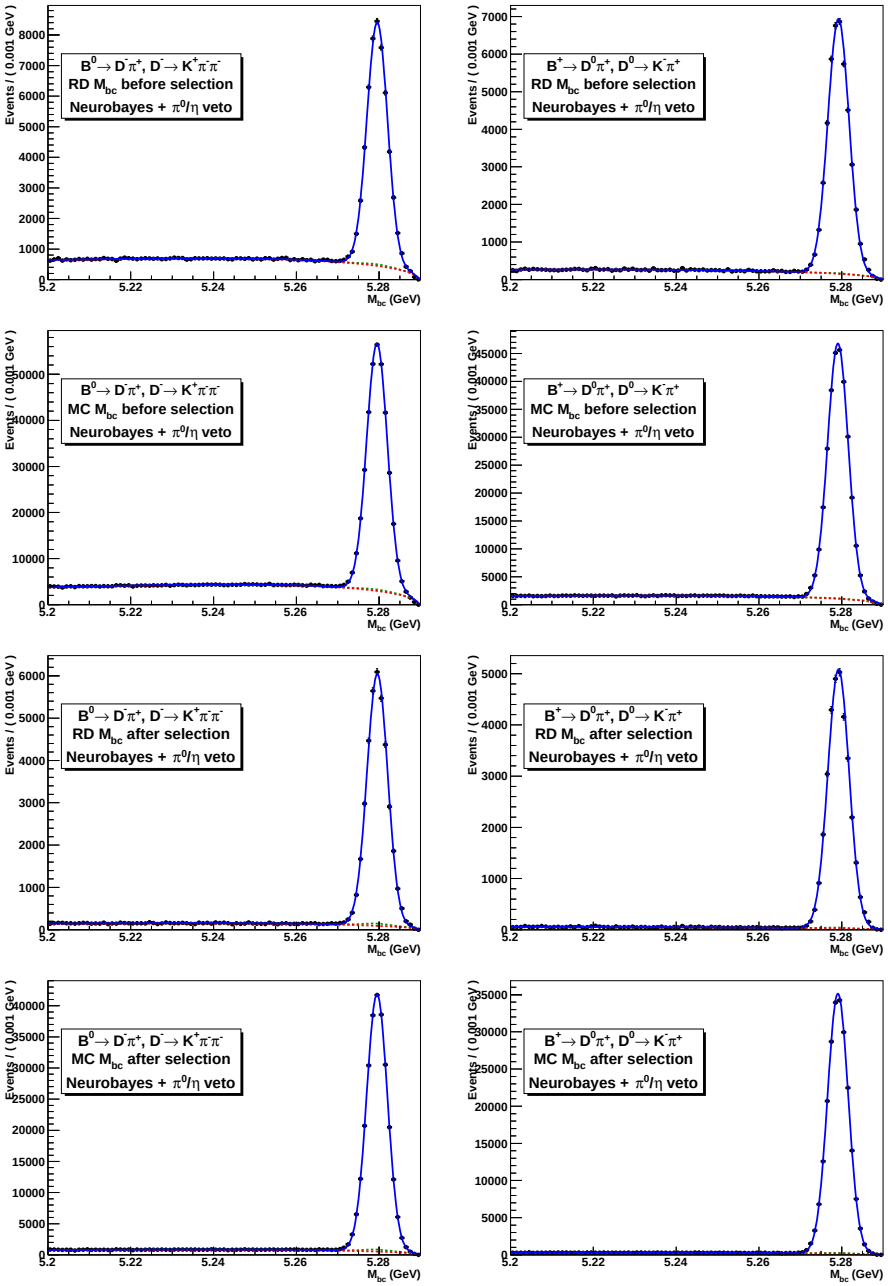

Figure 8.8.1: $M_{\rm bc}$ distributions of $B \to D\pi$ decay. Blue line shows combined 3 samples, signal, continuum and B decay background sample, red line shows continuum background and green small peak shows B decay background.

uncertainty from fixed parameters is estimated by moving them. The mean of signal and end point of ARGUS function are moved with ± 1 σ uncertainty evaluated by analyzing the decay of $B \to D\pi^+$. The tail parameter α and "n" in Crystal ball function are floated individually with the constraint of fixing the other parameters. Fixed yields are estimated with separating the samples in detail. For BB-general decay, number of this type of events are small, so we estimate the systematic uncertainty with floating ± 100 % of number of events. In rare$B$ bkg, since the main components are the decay of $B \to K^*\eta$ and $K^*\pi^0$, each PDF is decided using exclusive decay MC sample. The PDFs for $B \to K^*\eta$ and $K^*\pi^0$ are assigned then their fitted $M_{\rm bc}$ distribution figures can be found in Appendix-11.3. Their expected events are floated with ± 1 σ of the branching fraction. For the rare$B$ events without $B \to K^*\eta$ and $K^*\pi^0$, systematic uncertainties are estimated with floating $\pm 100\%$ of number of events. Grater than 80% of remaining $X_s\gamma$ sample are $B \to K\pi\pi\gamma$ events, so we separate the sample into two types, which are whether X_s decay into $K\pi\pi\gamma$ or not. The latest measurement of the branching fraction of $B \to K\pi\pi\gamma$ is performed by BaBar [38]. Events of decaying to $K\pi\pi\gamma$ are mainly come from some resonances and here we consider five resonances, $K_1(1270)$, $K_1(1400)$, $K^*(1410)$, $K_2^*(1430)$ and $K^*(1680)$. The amounts of $X_s\gamma$ bkg come from these five resonance are floated $\pm 1\sigma$ of measured uncertainty and other $X_s\gamma$ bkg except the events decaying to $K\pi\pi\gamma$ is floated $\pm 100\%$. In Table-8.10.1, assumed background list can be found.

Decay Mode	Branching Fraction	Generated MC size	Assumed error
Generic B decay	–	6 streams	$\pm 100\%$
$B^0 \to K^{*0}\eta$	$(1.59 \pm 0.10) \times 10^{-5}$	100 streams	$6.3\%(\pm 1\sigma)$
$B^+ \to K^{*+}\eta$	$(1.93 \pm 0.16) \times 10^{-5}$	100 streams	$8.3\%(\pm 1\sigma)$
$B^+ \to K^{*+}\pi^0$	$(8.2 \pm 1.9) \times 10^{-6}$	100 streams	$23\&(\pm 1\sigma)$
$B \to K_1(1270)\gamma$	$(14.5^{+2.1+1.2}_{-1.4-1.2}) \times 10^{-6}$	200 streams	$17\%(\pm 1\sigma)$
$B \to K_1(1400)\gamma$	$(4.1^{+1.9+1.2}_{-1.2-1.0}) \times 10^{-6}$	200 streams	54% $(\pm 1\sigma)$
$B \to K^*(1410)\gamma$	$(11.0^{+2.2+2.1}_{-2.0-1.1}) \times 10^{-6}$	200 streams	27% $(\pm 1\sigma)$
$B \to K_2^*(1430)\gamma$	$(1.2^{+1.0+1.2}_{-0.7-1.5}) \times 10^{-6}$	200 streams	160% $(\pm 1\sigma)$
$B \to K^*(1680)\gamma$	$(15.9^{+2.2+3.2}_{-1.9-2.4}) \times 10^{-6}$	200 streams	22% $(\pm 1\sigma)$
other rare$B$ sample	–	50 streams	$\pm 100\%$
other $X_s\gamma$ sample	–	40 streams	$\pm 100\%$

Table 8.10.1: Fixed background contribution list. Branching fraction is For $B \to K_1(1270)\gamma, K_1(1400)\gamma, K^*(1410)\gamma, K_2^*(1430)\gamma$ and $K^*(1680)\gamma$, we consider only $K\pi\pi\gamma$ final state. Their branching fractions written in the table are partial branching fraction decaying into $K\pi\pi$ final state. "rare$B$" and "$X_s\gamma$" sample are remaining rare$B$ bkg events except $B \to K^*\eta$ and $B \to K^*\pi^0$ and remaining X_s bkg events except $B \to K\pi\pi\gamma$ events.

8.11 Difference of Detector Response between Positive and Negative Charged Track

Since there are a little difference in the hadronization cross sections between positive and negative track, in general, the detection efficiency also have difference. In the measurement of CP asymmetry, the charge of B meson is determined using charged track, $K^{\pm}$ and $\pi^{\pm}$, so we have to know the difference of them exactly.

The sample which is vetoed in the $q\bar{q}$ bkg suppression step using Neurobayes technique is used. The advantage of using this sample is that there are few amount of signal and other peaking components which can have CP asymmetry. We can know the difference of the detector response unbiasedly, because the continuum events should be included randomly. Basically, applied selections are same as Table-5.5.1 and we add tight $M(K\pi)$ window selection which is same as signal box requirement, $|M(K\pi) - M_{K^*}| < 0.075$ GeV/c^2, to prevent to arise a bias come from momentum scale, change the ΔE selection to $-0.5 < \Delta E < 0.5$ GeV to increase the events and require less than zero of Neurobayes output. To reject as many B decay components as possible, Neurobayes selection is little tighter than the requirements in $B \to K^*\gamma$ analysis. Here we call this sample "anti-NB sample".

Ant-NB sample is divided into two types. One is the component of making a peak in $M_{\rm bc}$ distribution such as $B \to K^*\gamma$, $K^*\eta$ and $K * \pi^0$, the other is non-peaking component such as the $q\bar{q}$ bkg and B decay events except above peaking components. The fraction of peaking component is nearly 0.5% of all of events. This is small contribution comparing non-peaking component but not negligible. Figure-8.11.1 show the $M_{\rm bc}$ distributions of anti-NB sample for each reconstruction mode.

To obtain the amount of non-peaking components, we perform unbinned maximum likelihood fitting for $M_{\rm bc}$ distribution. PDFs for peaking and non-peaking components are assigned to Gaussian and ARGUS function, respectively. In this fitting, the shape parameters in Gaussian and the end point parameter in ARGUS function are fixed at MC value and other parameters are floated.

The results are shown in Table-8.11.1 and figures of fitted $M_{\rm bc}$ distributions are shown in Figure-8.11.2. The systematic uncertainty is evaluated by the charge asymmetry(R) defended as

$$R = \frac{N_+ - N_-}{N_+ + N_-} \tag{8.11.0.1}$$

where $N_{+/-}$ is number of positive/negative charged track events of non-peaking component. The source of systematic uncertainty arise from fixed parameters in the fitting. The charge asymmetries of signal MC are also calculated and written in Table-8.11.1 and consistent to obtained result within 1 σ error at $B^0 \to K^+\pi^-\gamma$ and $B^+ \to K_s\pi^+\gamma$ channels and width 1.3 σ error at $B^+ \to K^+\pi^0\gamma$ channel. Due to this check result, to assign the result to the systematic uncertainty is permitted.

8.12 Random Candidate Selection

To study whether some bias arise by random candidate selection or not, we perform random candidate selection 100 times with setting difference random seeds. Systematic uncertainty is described as

$$\text{Systematic uncertainty} = 1 - \frac{\mathrm{N}_{\rm sig}^{\text{new seed}}}{\mathrm{N}_{\rm sig}} \tag{8.12.0.2}$$

Reconstruction Mode	Non-peaking yield (RD)	signal MC events	asymmetry (%)
$B \to K^+\pi^-\gamma$	132,838 ± 384	581,597	RD : 0.32 ± 0.19 ± 0.02
$B \to K^-\pi^+\gamma$	131,997 ± 383	575,678	signal MC : 0.51 ± 0.09
$B \to K_s\pi^+\gamma$	36,759 ± 202	198,820	RD : -0.34 ± 0.37 ± 0.02
$B \to K_s\pi^-\gamma$	37,010 ± 204	199,715	signal MC : -0.22 ± 0.16
$B \to K^+\pi^0\gamma$	46,043 ± 229	151,246	RD : 0.87 ± 0.33 ± 0.03
$B \to K^-\pi^0\gamma$	45,250 ± 228	149,902	signal MC : 0.45 ± 0.18

Table 8.11.1: Extracted non-peaking and signal MC events and the calculation result of charge asymmetry come from detector response difference are listed. In asymmetry row, first value is asymmetry, second one is statistical uncertainty and last one is systematic uncertainty come from fixed parameter.

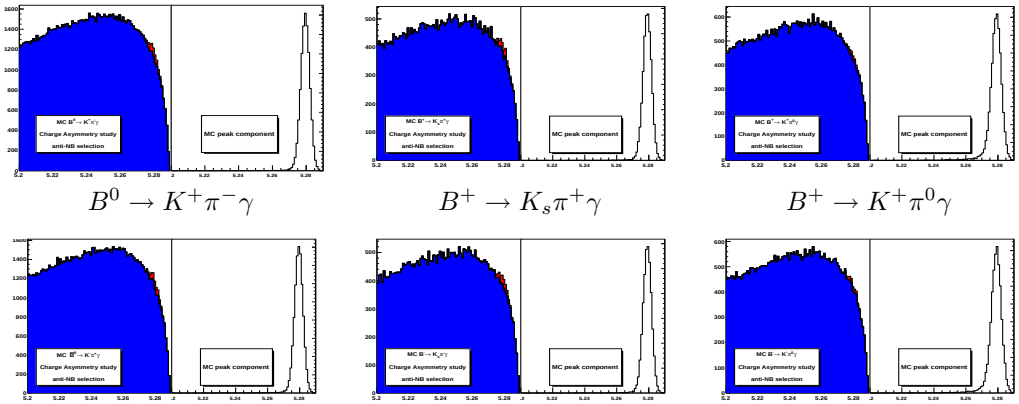

$B^0 \to K^+\pi^-\gamma$ $B^+ \to K_s\pi^+\gamma$ $B^+ \to K^+\pi^0\gamma$

$\overline{B}^0 \to K^-\pi^+\gamma$ $B^- \to K_s\pi^-\gamma$ $B^- \to K^-\pi^0\gamma$

Figure 8.11.1: $M_{\rm bc}$ distributions of anti-NB MC sample for charge asymmetry study. In the left side figures for each one, red region is peaking components and blue one is non-peaking components. The right side figures for each one show only peaking components.

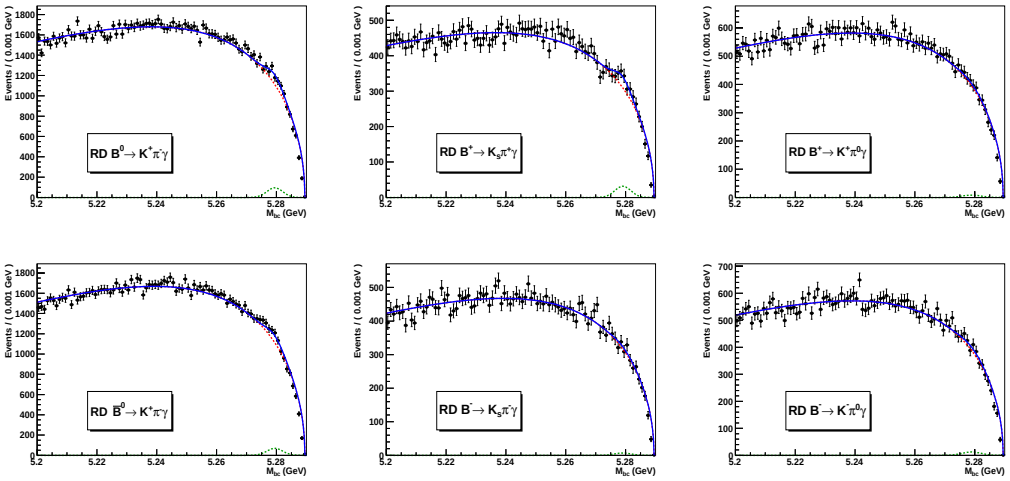

Figure 8.11.2: Fitted $M_{\rm bc}$ distributions of real data for charge asymmetry study. Blue line is sum of peaking and non-peaking components, red dotted line is non-peaking one and green dotted line is peaking one.

where $N_{sig}^{\text{new seed}}$ is the average of remaining signal events after random candidate selection in the signal box with setting new random seeds and N_{sig} is one with setting the seeds used in this analysis. The result is shown in Table-8.12.1 and numbers in this table are not scaled into 711 fb^{-1}. In all channels, evaluated systematic uncertainties are very small, so we can ignore this uncertainty.

mode	N_{evt}	Syst. (%)
$K_s\pi^0\gamma$	81,013/ 81,099	0.107 %
$K^+\pi^-\gamma$	1,068,040 / 1,068,370	0.031 %
$K_s\pi^+\gamma$	358,344 / 358,352	0.002 %
$K^+\pi^0\gamma$	256,897 / 256,654	0.095 %
combined	1,764,290 / 1,764,470	0.010 %

Table 8.12.1: Number of remaining signal events without scaling into 711 fb^{-1}, 200 streams. N_{evt} is number of remaining events in signal box after random candidate selection (RCS) then former of slash is Number of events after RCS with original seed and latter one is that of new seed. Systematic uncertainty value is absolute value.

8.13 Uncertainty in Some Parameters

In the calculation of isospin, we have to consider f_{+-}/f_{00} and τ_B^+/τ_{B^0}. The mean of f_{+-}/f_{00} is the fraction of the branching fraction of $\Upsilon(4S) \to B^+B^-$ and $\Upsilon(4S) \to B^0\overline{B}^0$ and that of τ_B^+/τ_{B^0} is life time ratio. To evaluate the isospin asymmetry exactly, the obtained branching fraction have

to be correct using f_{+-}/f_{00} and life time ratio. In the current measurements in BaBar, Belle and CLEO [58], assuming $\Upsilon(4S)$ is always decaying into $B\overline{B}$, the branching fractions are evaluated as $\mathcal{B}(\Upsilon(4S) \to B^+B^-) = 0.514 \pm 0.006$ $\mathcal{B}(\Upsilon(4S) \to B^0\overline{B}^0) = 0.486 \pm 0.006$ and life time of B mesons are measured as $\tau_{B^0} = 1.520 \pm 0.004$ ps, $\tau_{B^+} = 1.638 \pm 0.004$ ps. Therefore systematic uncertainties for f_{+-}/f_{00} and τ_B^+/τ_{B^0} are assigned as 1.2% and 0.4%.

Chapter 9

Result and Discussion

9.1 Result

The results of the measurement of the branching fractions and CP asymmetries using real data set are obtained and summarized in Table-9.1.1, 9.1.2 and fitted $M_{\rm bc}$ distributions are shown in Figure-9.1.3, 9.1.4.

	signal yield	efficiency	$\mathcal{B}(\times 10^{-5})$
$B^0 \to K_s\pi^0\gamma$	352.5 ± 23.2 ± 11.5	1.18 ± 0.00	3.98 ± 0.26 ± 0.18
$B^0 \to K^+\pi^-\gamma$	4681.3 ± 81.9 ± 74.2	15.65 ± 0.01	3.99 ± 0.07 ± 0.14
$B^+ \to K_s\pi^+\gamma$	1481.6 ± 45.9 ± 24.6	5.13 ± 0.01	3.64 ± 0.12 ± 0.12
$B^+ \to K^+\pi^0\gamma$	1145.7 ± 45.4 ± 37.9	3.64 ± 0.01	3.96 ± 0.16 ± 0.18
$B^0 \to K^{*0}\gamma$			3.99 ± 0.07 ± 0.14
$B^+ \to K^{*+}\gamma$			3.75 ± 0.09 ± 0.12

Table 9.1.1: The table of the result of branching fractions. First number is center value, second is statistical uncertainty and third is systematic uncertainty.

	N($B \to K^*\gamma$)	N($\overline{B} \to \overline{K}^*\gamma$)	A_{CP}
$B^0 \to K^+\pi^-\gamma$	2385.9 ± 57.4 ± 37.8	2294.9 ± 56.4 ± 37.9	-0.013 ± 0.017 ± 0.001
$B^+ \to K_s\pi^+\gamma$	724.5 ± 32.7 ± 12.0	757.1 ± 32.1 ± 12.6	0.017 ± 0.030 ± 0.002
$B^+ \to K^+\pi^0\gamma$	580.1 ± 32.0 ± 19.2	565.6 ± 32.2 ± 18.7	-0.005 ± 0.038 ± 0.003
$B^+ \to K^{*+}\gamma$			0.008 ± 0.024 ± 0.002
$B \to K^*\gamma$			-0.006 ± 0.014 ± 0.001

Table 9.1.2: The table of the result of CP asymmetries. First number is center value, second is statistical uncertainty and third is systematic uncertainty.

Isospin asymmetry and ΔA_{CP} are obtained as

$$\Delta_{0-} = 0.067 \pm 0.015 \pm 0.013, \quad (9.1.0.1)$$

$$\Delta A_{CP} = 0.021 \pm 0.029 \pm 0.002. \quad (9.1.0.2)$$

The all of results are plotted in Figure-9.1.1,9.1.2 and compared among experiments.

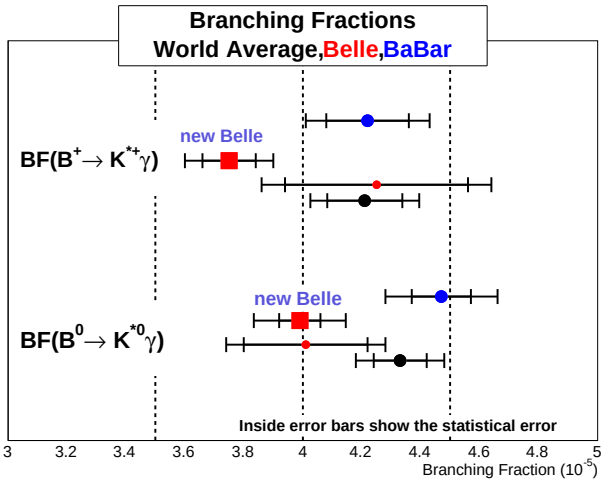

Figure 9.1.1: The plot of the result of the branching fraction each experiment. The black, red and blue points show world average and Belle and BaBar results. The internal error bars show only the statistical uncertainty and outer ones show the uncertainty combined statistical and systematic one. The small red circle points are previous Belle results and the large red square points are new Belle results.

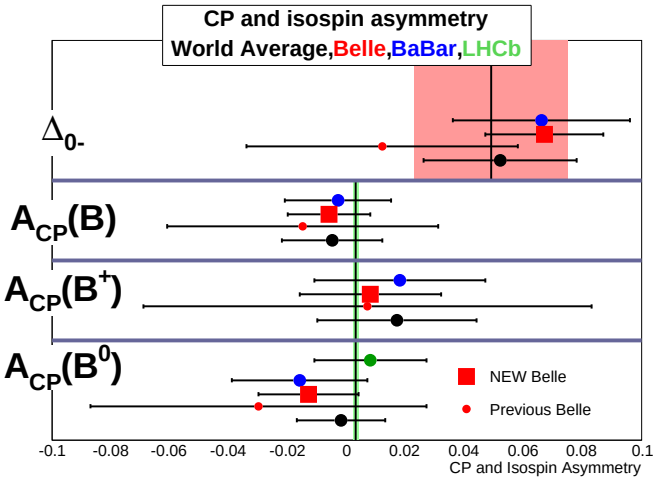

Figure 9.1.2: The plot of the result of the direct CP and isospin asymmetry, and ΔA_{CP} each experiment. The black, red, blue and green points show world average and Belle, BaBar and LHCb results. The small red circle points are previous Belle results and the large red square points are new Belle results.

All the systematic uncertainty source assigned to the result of real data are listed in Table-9.1.3, 9.1.4. The major systematic sources of the branching fractions are photon efficiency, particle identification and number of BB pairs, that of CP asymmetries and ΔA_{CP} are fitter bias and the difference of the detector response in charge asymmetry and that of isospin asymmetry is f_{+-}/f_{00}.

9.1.1 Helicity Angle of K^*

The spin of K^* is one, so the distribution of cosine of helicity angle of K^* ($\cos\theta_{hel}^{K\pi}$) can be represented by D-function like $\cos\theta_B$ defined in Eq-(6.1.0.13). The distribution is made by filling the extracted signal for each $\cos\theta_{hel}^{K\pi}$ bin. Here the step size of $\cos\theta_{hel}^{K\pi}$ is set at 0.1, so total number of bins are 20. Fit function is defined as

$$f_{helicity}(\cos\theta_{hel}^{K\pi}) = N(1-\cos^2\theta_{hel}^{K\pi}) \tag{9.1.1.1}$$

where N is normalization factor. This function has constraint of zero at $\cos\theta_{hel}^{K\pi} = \pm 1$. Since the efficiencies are reduced near edge of acceptance because K^* is the two body decay, we calibrate the efficiency using the efficiency of MC truth.

Figure-9.1.5 show the helicity angle distributions. The fittings of these distributions are succeeded, which is the good agreement that we can extract spin-1 component correctly.

9.2 Discussion

The result of the branching fraction in $B^0 \to K^{*0}\gamma$ is very close to the previous Belle result, $(4.01 \pm 0.21 \pm 0.17) \times 10^{-5}$, and deviated from BaBar result in 1.9 σ. The result of the branching fraction in $B^+ \to K^{*+}\gamma$ is deviated from the previous result and world average in 0.5σ and 1.8 σ. Since in the recent work in Belle [15], which is the measurement of the branching fraction in the decay of $B \to X_s\gamma$ using sum of exclusive method, the branching fraction with the constraint of M_{X_s} <1.15 GeV/c^2 was obtained as $\mathcal{B} = (3.99 \pm 0.08(\text{onlystat.})) \times 10^{-5}$, which is good approximation of $B \to K^*\gamma$ study because the range of $M_{X_s} < 1.15$ GeV/c^2 is dominated by $K^*\gamma$ event and little $B \to K\pi\pi\gamma$ contribution is expected by the tight requirement for ΔE selection, $-0.15 < \Delta E < 0.08$ GeV. Therefore the results in this study have good agreement with latest study.

For more detail check, the set up for each measurement are changed. The point of the difference between previous and new Belle measurements is the value of f_{+-}/f_{00}. In previous analysis, the f_{+-}/f_{00} is assumed as 1 but we use latest value, $f_{+-}/f_{00} = 1.058 \pm 0.024$. The scaled previous Belle results are

$$\mathcal{B}(B^0 \to K^{*0}\gamma) = (4.12 \pm 0.22 \pm 0.17) \times 10^{-5}\text{and} \tag{9.2.0.2}$$

$$\mathcal{B}(B^+ \to K^{*+}\gamma) = (4.13 \pm 0.30 \pm 0.23) \times 10^{-5}. \tag{9.2.0.3}$$

The our results are consistent to the previous Belle result with in 1 σ. The different point between BaBar and Belle measurements is the background sample of $B \to K\pi\pi\gamma$. We include the $B \to K\pi\pi\gamma$ samples which are generated by five types of resonances. The detail is explained in Section-4 on the other hand the method for the estimation of the amount of $B \to K\pi\pi\gamma$ in BaBar is based on inclusive $B \to X_s\gamma$ sample. To consistency check, our results are re-obtained using inclusive $B \to X_s\gamma$ sample without the $B \to K\pi\pi\gamma$ sample generated with going through resonances.

Syst. source	$K_s\pi^0\gamma$	$K^+\pi^-\gamma$	$K_s\pi^+\gamma$	$K^+\pi^0\gamma$	$K^{*+}\gamma$	$K^{*0}\gamma$
MC stat. $K_s\pi^0\gamma$	0.358	-	-	-	0.001	0.024
MC stat. $K^+\pi^-\gamma$	-	0.133	-	-	-	0.125
MC stat. $K_s\pi^+\gamma$	-	-	0.239	-	0.159	-
MC stat. $K^+\pi^0\gamma$	-	-	-	0.285	0.094	-
n_{BB}	1.370	1.370	1.370	1.370	1.370	1.370
Photon	2.000	2.000	2.000	2.000	2.000	2.000
tracking	-	0.700	0.350	0.350	0.347	0.645
K/π ID	-	1.650	0.800	0.840	0.820	1.568
π^0	1.270	-	-	1.270	0.424	0.089
K_s	1.140	-	1.140	-	0.747	0.075
$M(K\pi)$	0.110	0.110	0.110	0.110	0.110	0.110
$\pi^0\eta$ veto + qq supp.	0.560	0.560	0.560	0.560	0.565	0.568
charge asym. $K^+\pi^-\gamma$	-	0.095	-	-	-	0.088
charge asym. $K_s\pi^+\gamma$	-	-	0.180	-	0.120	0.001
charge asym. $K^+\pi^0\gamma$	-	-	-	0.157	0.053	-
life time	-	-	-	-	-	-
f_{+-}/f_{00}	1.200	1.200	1.200	1.200	1.200	1.200
wrong tag fraction	-	-	-	-	-	-
number of generic BB decay	0.022	0.014	0.018	0.003	0.008	0.013
number of rare$B$	0.248	0.663	0.594	0.579	0.581	0.636
number of $X_s\gamma$	0.090	0.070	0.113	0.114	0.108	0.076
number of combinatorial bkg.	0.126	0.023	0.051	0.157	0.085	0.029
number of cross-feeds bkg.	0.007	0.007	0.007	0.007	0.006	0.006
number of $K^*\eta$	0.057	0.084	0.117	0.091	0.106	0.081
number of $K^*\pi^0$	-	0.002	0.223	0.164	0.201	0.002
number of $K_1(1270)\gamma$	0.328	0.200	0.280	0.358	0.303	0.212
number of $K_1(1400)\gamma$	0.185	0.133	0.130	0.162	0.138	0.139
number of $K^*(1410)\gamma$	0.059	0.040	0.050	0.057	0.051	0.043
number of $K_2^*(1430)\gamma$	1.231	0.594	0.507	0.594	0.528	0.638
number of $K^*(1680)\gamma$	0.198	0.124	0.155	0.196	0.167	0.131
number of $M_{\rm bc}$ mean with π^0	0.060	-	-	0.065	0.022	0.004
number of $M_{\rm bc}$ mean without π^0	-	0.035	0.030	-	0.020	0.031
qq ARGUS m_0	0.040	0.079	0.038	0.383	0.158	0.077
Signal cb α $K_s\pi^0\gamma$	1.270	0.002	0.004	-	0.004	0.075
Signal cb α $K^+\pi^0\gamma$	-	0.002	0.004	1.896	0.233	0.003
Signal cb n $K_s\pi^0\gamma$	0.318	0.002	0.004	-	0.004	0.015
Signal cb n $K^+\pi^0\gamma$	-	0.002	0.004	1.744	0.220	0.004
Fitter bias	2.353	0.193	0.663	1.309	0.182	0.165
total	4.454	3.452	3.317	4.427	3.158	3.390

Table 9.1.3: The detail of systematic uncertainties (%) for branching fractions assigned to the real data results

Syst. source	$A_{CP}^{K^{*0}\gamma}$	$A_{CP}^{K_s\pi^+\gamma}$	$A_{CP}^{K^+\pi^0\gamma}$	$A_{CP}^{K^{*+}\gamma}$	$A_{CP}^{comb.}$	Δ_{0-}	ΔA_{CP}
MC stat. $K_s\pi^0\gamma$	-	-	-	-	-	0.012	-
MC stat. $K^+\pi^-\gamma$	-	-	-	-	-	0.062	-
MC stat. $K_s\pi^+\gamma$	-	-	-	0.002	0.001	0.079	0.002
MC stat. $K^+\pi^0\gamma$	-	-	-	0.002	0.001	0.047	0.002
n_{BB}	-	-	-	-	-	-	-
Photon	-	-	-	-	-	-	-
tracking	-	-	-	-	-	0.148	-
K/π ID	-	-	-	-	-	0.372	0.00
π^0	-	-	-	0.012	-	0.167	0.012
K_s	-	-	-	-	-	0.334	0.010
$M(K\pi)$	-	-	-	-	-	-	-
$\pi^0\eta$ veto + qq supp.	-	-	-	-	-	-	-
charge asym. $K^+\pi^-\gamma$	0.095	-	-	-	0.062	0.044	0.095
charge asym. $K_s\pi^+\gamma$	-	0.184	-	0.117	0.040	0.059	0.117
charge asym. $K^+\pi^0\gamma$	-	-	0.159	0.058	0.020	0.027	0.058
life time	-	-	-	-	-	0.185	-
f_{+-}/f_{00}	-	-	-	-	-	1.200	-
wrong tag fraction	0.005	-	-	-	-	-	0.005
number of generic BB decay	0.004	0.006	0.001	0.001	0.003	0.002	0.003
number of rare$B$	0.005	0.006	0.007	0.009	0.001	0.028	0.014
number of $X_s\gamma$	0.001	0.001	0.013	0.006	0.002	0.016	0.007
number of combinatorial bkg.	-	0.001	0.003	0.002	0.001	0.028	0.002
number of cross-feeds bkg.	-	-	0.001	-	-	-	-
number of $K^*\eta$	0.014	0.004	0.004	0.003	0.008	0.012	0.018
number of $K^*\pi^0$	-	0.002	0.004	0.001	0.001	0.099	0.001
number of $K_1(1270)\gamma$	0.003	0.016	0.010	0.016	0.008	0.046	0.013
number of $K_1(1400)\gamma$	0.002	0.010	0.002	0.008	0.005	-	0.006
number of $K^*(1410)\gamma$	0.001	0.003	0.001	0.002	0.001	0.004	0.001
number of $K_2^*(1430)\gamma$	0.018	0.027	0.025	0.028	0.022	0.055	0.010
number of $K^*(1680)\gamma$	0.001	0.008	0.005	0.008	0.004	0.018	0.007
number of $M_{\rm bc}$ mean with π^0	-	-	0.005	0.001	-	0.009	0.001
number of $M_{\rm bc}$ mean without π^0	0.001	0.003	-	0.002	-	0.005	0.003
qq ARGUS m_0	0.005	0.006	0.069	0.037	0.016	0.040	0.032
Signal cb α $K_s\pi^0\gamma$	0.004	-	-	0.009	0.005	0.036	0.005
Signal cb α $K^+\pi^0\gamma$	0.009	-	0.103	0.001	0.004	0.117	0.008
Signal cb n $K_s\pi^0\gamma$	0.005	-	-	0.009	0.005	0.006	0.004
Signal cb n $K^+\pi^0\gamma$	0.003	-	0.072	0.014	0.006	0.112	0.011
Fitter bias	0.070	0.116	0.164	0.092	0.082	0.083	0.115
total	0.121	0.220	0.271	0.170	0.117	1.324	0.204

Table 9.1.4: The detail of systematic uncertainties (%) for several variables assigned to the real data results

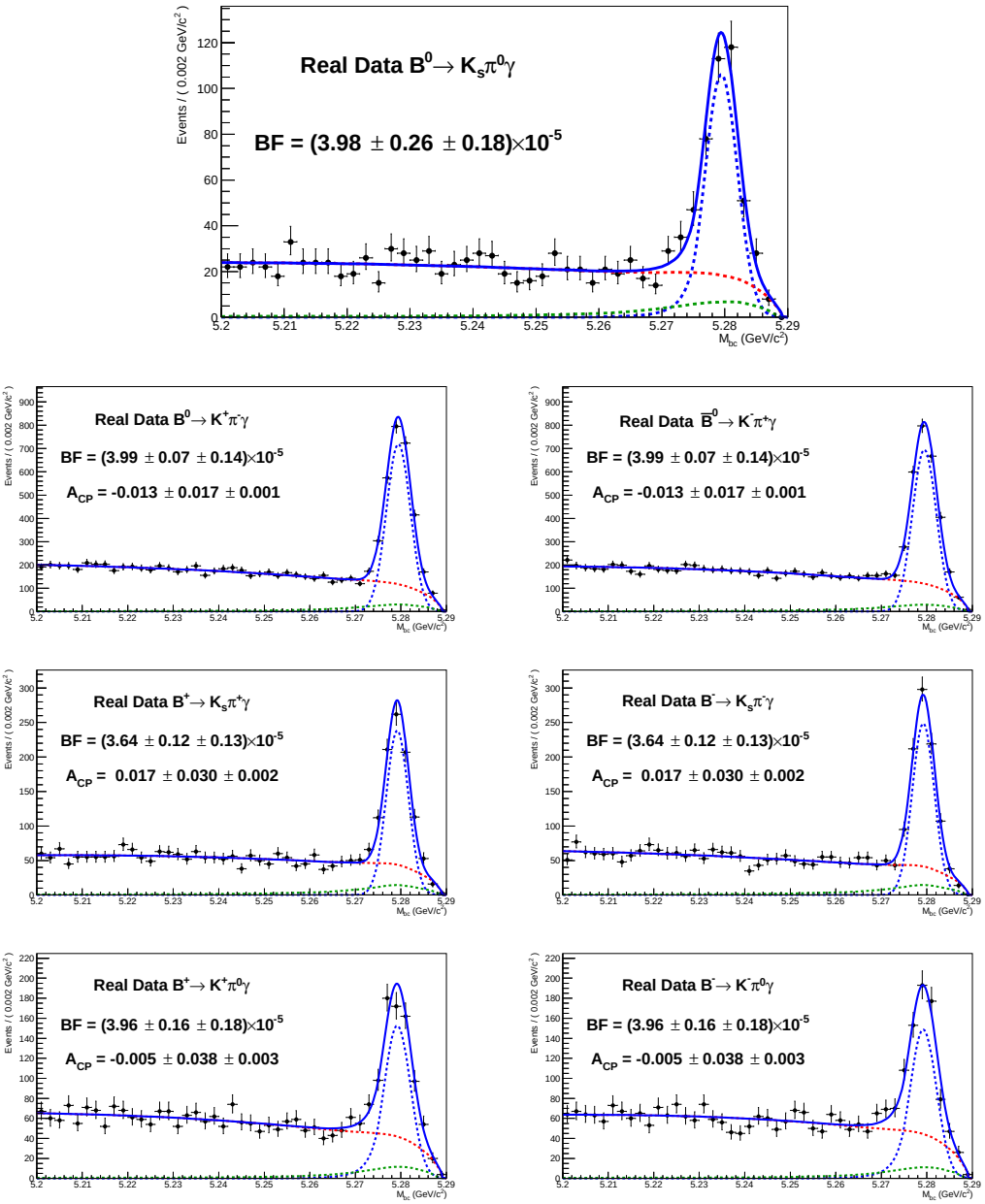

Figure 9.1.3: Fit result of $M_{\rm bc}$ distributions for real data. Likelihood functions used for these fits are Eq-7.2.0.10, 7.2.0.11, 7.2.0.12, 7.2.0.13.

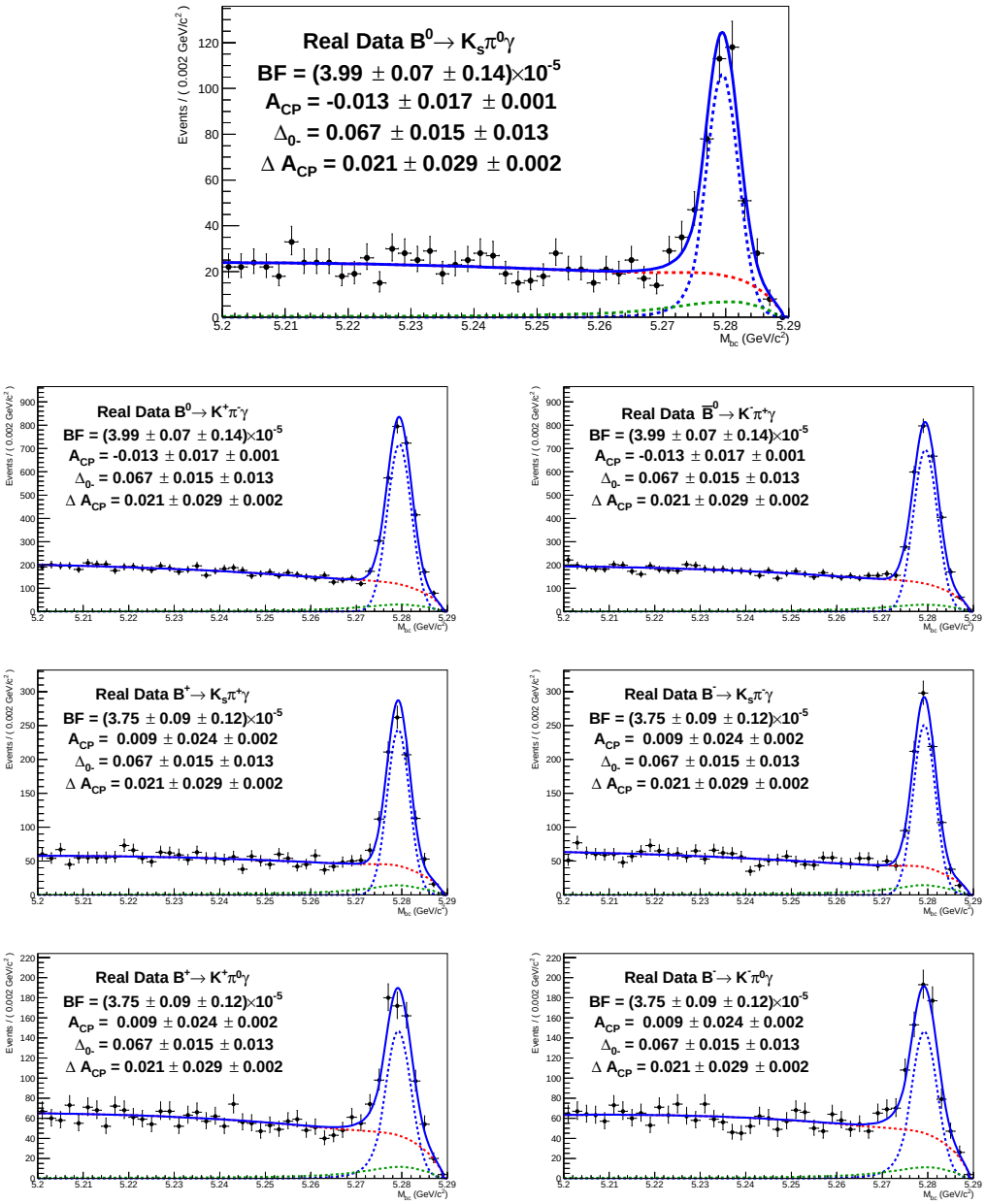

Figure 9.1.4: Fit result of $M_{\rm bc}$ distributions for real data. Likelihood function used for these fits is Eq-7.2.0.15

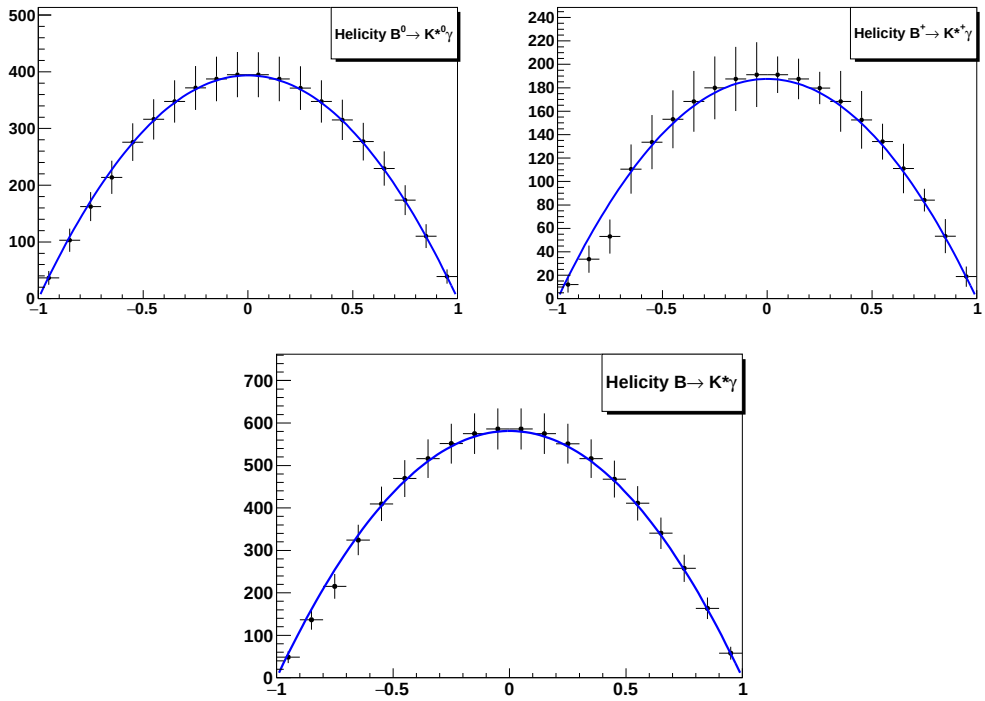

Figure 9.1.5: The distributions of Cosine of helicity angle of K^* fitted by 2-nd order Chebyshev, Eq-9.1.1.1

The re-obtained new Belle results are

$$\mathcal{B}(B^0 \to K^{*0}\gamma) = (4.10 \pm 0.07 \pm 0.14) \times 10^{-5} \text{and} \tag{9.2.0.4}$$

$$\mathcal{B}(B^+ \to K^{*+}\gamma) = (4.88 \pm 0.10 \pm 0.12) \times 10^{-5}. \tag{9.2.0.5}$$

Using these results, the deviations of neutral and charged B decay from BaBar results are recalculated as 1.5 and 1.4 σ. The most precise measurement of branching fractions in the world are updated by this results. However, the sensitivity to the new physics is little by the measurement of the branching fraction, because of huge form factor uncertainty. The uncertainty for the branching fractions are dominated by the systematic uncertainty and the main sources are the counting of number of B mesons and high energy photon detection. Therefore the significant improvement in Belle II which is the experiment upgrading the KEKB accelerator to 40 times instantaneous luminosity is not expected. However particle identification system will be updated, so the PID uncertainty will get small and since we will have significant number of events, the background come from B decay can be rejected by requiring tight ΔE range.

The result of all of CP asymmetries are consistent to both world average and zero within 1 σ. The most sensitive measurements except the decay of $B^0 \to K^{*0}\gamma$ are updated. The current best measurement of CP asymmetry in $B^0 \to K^{*0}\gamma$ is reported by LHCb with $A_{CP} = 0.008 \pm 0.017 \pm 0.009$ [22]. Our obtained result is comparable to it. As we introduce in section-2.4.2, direct CP asymmetry is sensitive to the imaginary part of Wilson coefficient C_7. Due to our result, the world average is approached to zero and the uncertainty is got small. Since the world average is updated with including this result, the allowed range of 95% C.L of constraint for the imaginary part of C_7 is got narrow from $|\mathrm{Im}C_7(m_b)| < 0.16$ to $|\mathrm{Im}C_7(m_b)| < 0.11$. Figure-9.2.1 shows the latest constraint.

In the future, if the CP asymmetry of charged decay mode, $B^+ \to K^{*+}\gamma$, is calculated, the constraint for $\mathrm{Im}C_7$ will be tight because annihilation contribution can be cancel the real part of C_7 and the contribution of imaginary part is enhanced. The measurement of the direct CP asymmetry in the decay of $B^+ \to K^{*+}\gamma$ is hard in LHCb because identifying the π^0 or K_s is challenging.

The result of isospin asymmetry is consistent to world average and the standard model prediction. In addition, the first evidence of isospin violation is measured with 3.4 σ precision. This result is updated the current world record. The constraint of 95% confidence level (C.L) for $m_{1/2}$ and $\tan\beta$ explained in Section-2.4.2 is not updated, which is shown in Figure-9.2.2, but the center value of this result is grater than world average and the constraint from our result is strict since the uncertainty is got small.

The result of difference of CP asymmetry between charged and neutral B meson in the decay of $B \to K^*\gamma$ is first measurement in the world. In the SM, ΔA_{CP} is exactly zero, so the result in this study is consistent to SM prediction.

In Belle II, statistical uncertainties of all measurements will be got small nearly 1/7 because the design integrated luminosity is 50 times of Belle. The branching fraction uncertainty is already dominated by systematic uncertainty, so the dramatic improvement is hopeless. The uncertainties of CP asymmetry and ΔA_{CP} are dominated by statistical one so the sensitivity will be improved significantly to distinguish some new physics stability. Then the statistical uncertainty of A_{CP} will be comparable to the systematic uncertainty at the final result of Belle II.

The statistical uncertainty of isospin asymmetry uncertainty is similar to systematic one which is dominated by f_{+-}/f_{00}. Both the statistical and systematic uncertainty will be improved. f_{+-}/f_{00} is measured by using computing the fraction of the single and double tagging reconstruction [59]. The single tagging is to reconstruct the decay of $B \to D^{*+}\ell\bar{\nu}_\ell$ in single B meson and double one is to reconstruct the same decay mode in both of B and $\bar{B}$. The uncertainty of

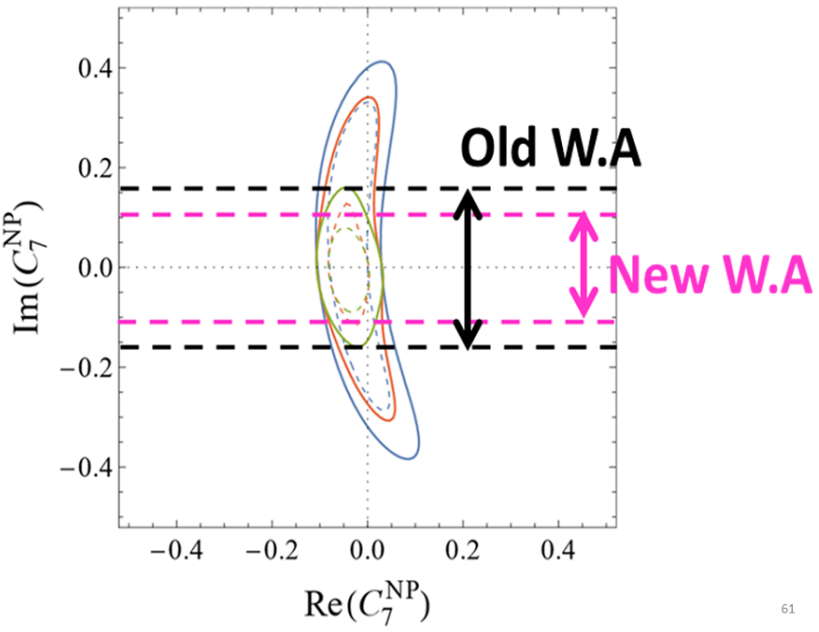

Figure 9.2.1: The contour plot of Re($C_7^{\rm NP}$)-Im($C_7^{\rm NP}$). The blue dot and solid line show the 1 and 2 σ constraint without the result of $A_{CP}(B \to K^*\gamma)$. The red (green) line show the constraint including 50 (25)% theoretical uncertainty with including the result of $A_{CP}(B \to K^*\gamma)$. The black and magenta dotted lines show the constraint for Im($C_7^{\rm NP}$) by previous and new world average (W.A) of $A_{CP}(B \to K^*\gamma)$.

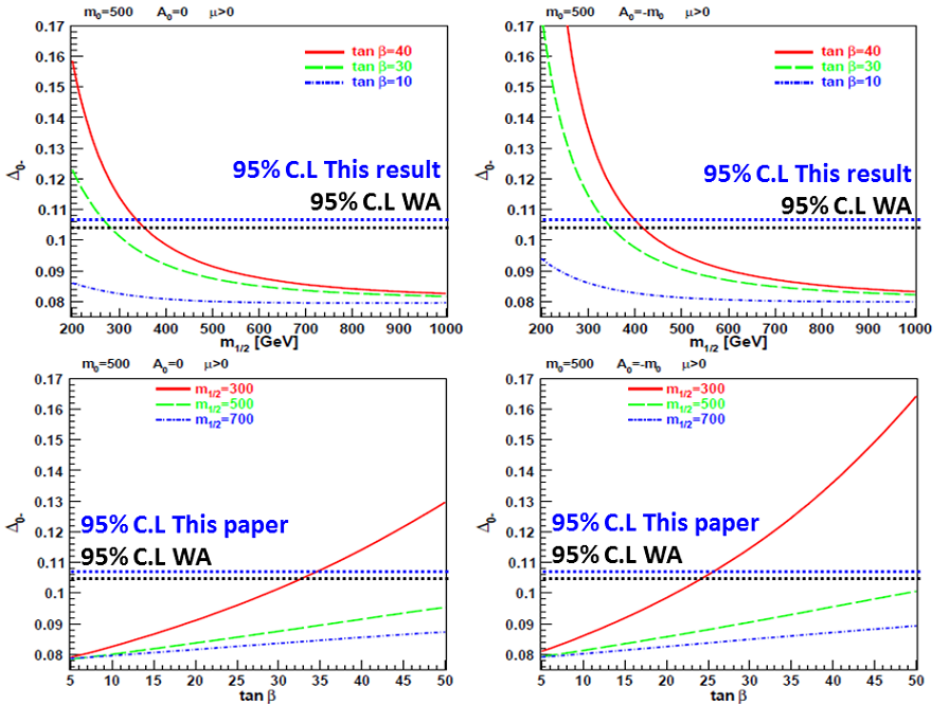

Figure 9.2.2: Isospin asymmetry vs $m_{1/2}$ and $\tan\beta$ for $A_0 = 0$ and $A_0 = -m_0$ with 95% C.L lines. WA means the world average (Black line) and our result (Blue line).

current result is dominated by statistical one, so the precision of f_{+-}/f_{00} will be able to get small in the future. Therefor the first discovery of isospin violation can be expected significantly in the end of the Belle Ⅱ experiment.

Chapter 10

Conclusion

The decay of $B \to K^*(892)\gamma$ is one of the most sensitive decays to new physics in $b \to s$ transition because its decay process can be predicted with high precision, it has large branching fraction and there are small amount of backgrounds since $K^*(892)$ is far from higher kaon resonances.

We use the full data set around $\Upsilon(4S)$ resonance accumulated by the Belle experiment which is corresponding to 772 million $B\overline{B}$ pairs. The obtained results are

$$\begin{aligned}
\mathcal{B}(B^0 \to K^{*0}\gamma) &= (3.99 \pm 0.07 \pm 0.14) \times 10^{-5}, \\
\mathcal{B}(B^+ \to K^{*+}\gamma) &= (3.75 \pm 0.09 \pm 0.12) \times 10^{-5}, \\
A_{CP}(B^0 \to K^{*0}\gamma) &= -0.013 \pm 0.017 \pm 0.001, \\
A_{CP}(B^+ \to K^{*+}\gamma) &= 0.008 \pm 0.024 \pm 0.002, \\
A_{CP}(B \to K^*\gamma) &= -0.006 \pm 0.014 \pm 0.001, \\
\Delta_{0-} &= 0.067 \pm 0.015 \pm 0.013 \quad \text{and} \\
\Delta A_{CP} &= 0.021 \pm 0.029 \pm 0.002
\end{aligned}$$

where the first and second uncertainties are statistical and systematic ones, respectively. The branching fractions in the decay of $B^0 \to K^{*0}\gamma$ and $B^+ \to K^{*+}\gamma$ are consistent to the previous Belle result within 1 σ and to the BaBar's result within 1.5 σ, respectively.

Obtained CP asymmetries are consistent to zero within 1σ. Obtained isospin asymmetries are close to the standard model prediction and this measurement is the first evidence of isospin violation in $B \to K^*\gamma$ with 3.4 σ precision. The ΔA_{CP} for $B \to K^*\gamma$ is the first measurement. Since in the standard model prediction, ΔA_{CP} is zero, obtained value is consistent. The most precise measurements of all the observables measured at this study in the world are updated by our result. The uncertainty of the branching fraction is dominated by the systematic one, so we can not expect the significant improvement in the future B-factory Belle Ⅱ. On the other hand, the uncertainties of CP asymmetry and ΔA_{CP} are dominated by statistical one therefore more precise test for the NP will able to be performed in Belle Ⅱ. The statistical and systematic uncertainty of the isospin asymmetry is comparable and if it will be measured in Belle Ⅱ, isospin violation will be found with 5 σ precision.

Chapter 11

Appendix

11.1 Some Figures of Reconstructed B meson

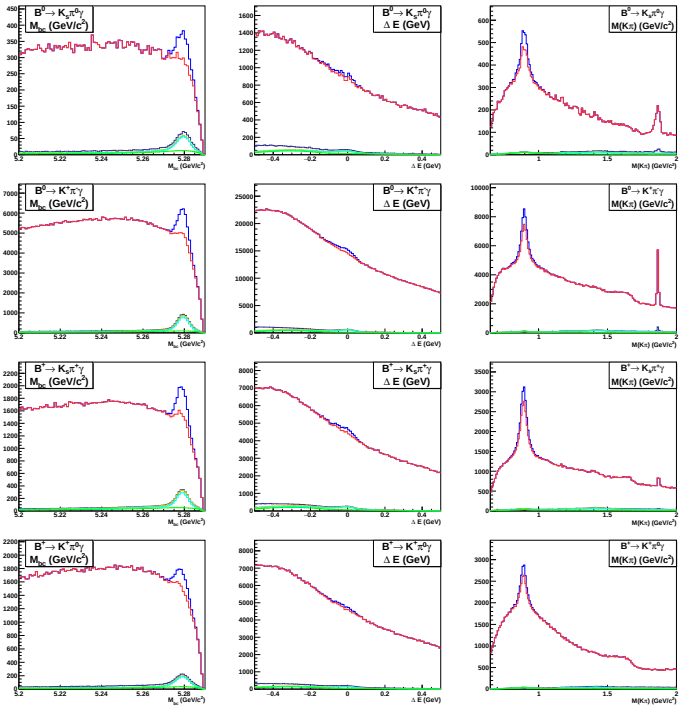

Figure 11.1.1: $M_{\rm bc}$ and $M(K\pi)$ distributions without $M_{\rm bc}$ and $M(K\pi)$ selection

11.2 $M(K\pi)$ fit function

In general $M(K\pi)$ distribution is represented by P-wave Breit-Wigner function. Here the detail of Eq-(8.7.0.6) is written.

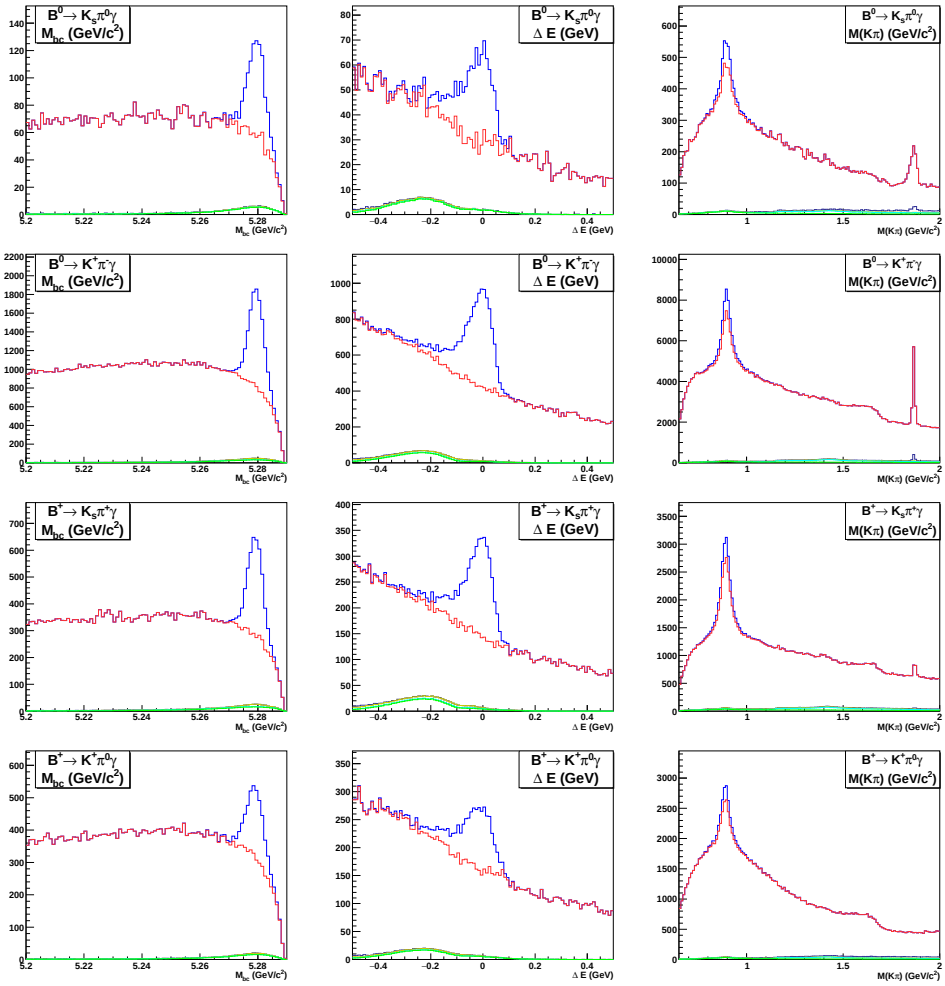

Figure 11.1.2: $M_{\rm bc}$ distribution with $M(K\pi)$ selection and $M(K\pi)$ distribution with $M_{\rm bc}$ selection

$$
\begin{aligned}
f_{BW}(M_{K\pi}) &= \frac{2M_{K\pi}F_{K^*}^2}{(M_{K^*}^2 - M_{K\pi}^2)^2 + M_{K^*}^2\Gamma_{K\pi}^2}\Big\{(M_{K\pi}^2+\alpha)^2\beta + 2(M_{K\pi}^2+\alpha)\beta^2 + \frac{4}{3}\beta^3\Big\} \\
&\textit{where} \\
\alpha &= \frac{M_B^2(M_\pi^2 - M_K^2)}{M_{K^*}^2} - (M_B^2 + M_K^2 + M_\pi^2) \\
\beta &= -4\Big\{\Big(\frac{M_{K\pi}^2 + M_K^2 - M_\pi^2}{2M_{K\pi}}\Big)^2 - M_K^2\Big\}\Big(\frac{M_B^2 - M_{K\pi}^2}{2M_{K\pi}}\Big)^2
\end{aligned}
$$

11.3 Fit Figures

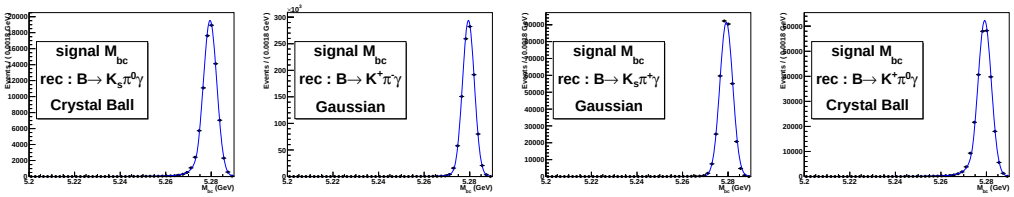

Figure 11.3.1: Signal $M_{\rm bc}$ distribution fitted by Gaussian for witout π^0 modes and by Crystal ball shape function for with π^0 modes

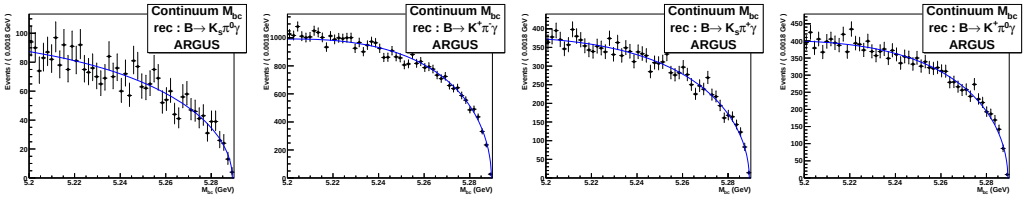

Figure 11.3.2: $M_{\rm bc}$ distribution of continuum background fitted by Argus function

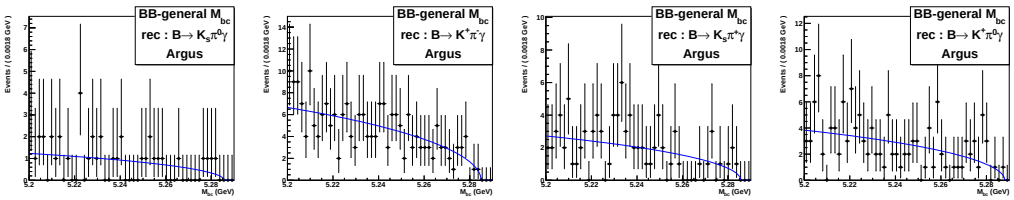

Figure 11.3.3: $M_{\rm bc}$ distribution of general B decay background fitted by Argus function

11.4 K_s systematics

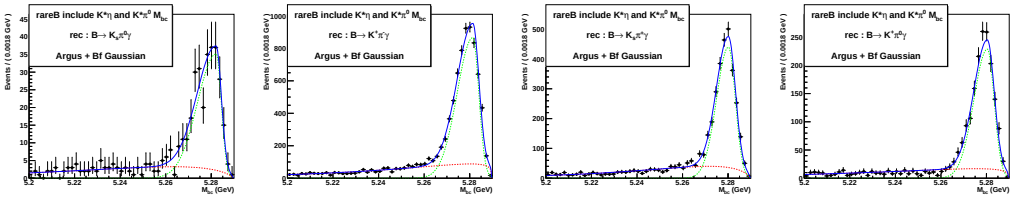

Figure 11.3.4: $M_{\rm bc}$ distribution of rare B decay background fitted by Argus function added Bifurecated Gaussian

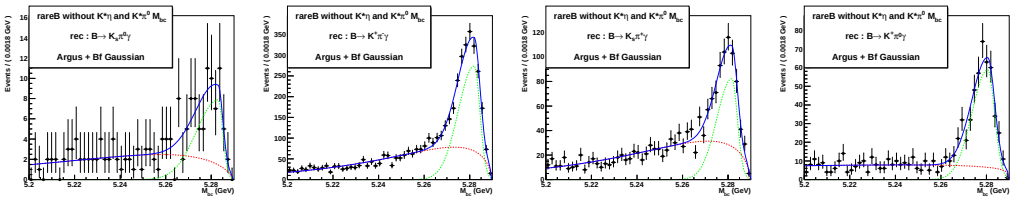

Figure 11.3.5: $M_{\rm bc}$ distribution of rare B decay background without $B \to K^*\eta$ and $B \to K^*\pi^0$ components fitted by Argus function added Bifurecated Gaussian

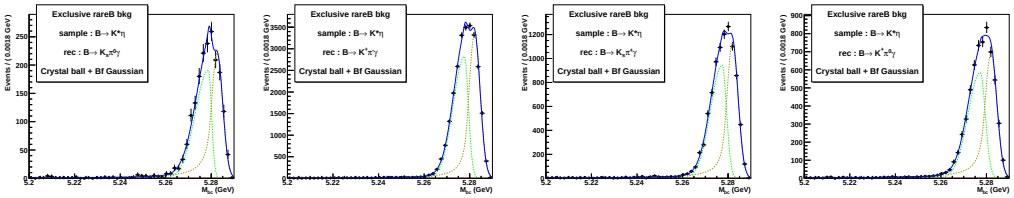

Figure 11.3.6: $M_{\rm bc}$ distribution of $B \to K^*\eta$ fitted by Crystal ball function added Bifurecated Gaussian

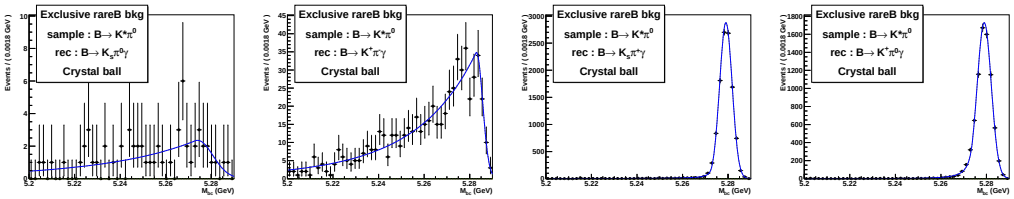

Figure 11.3.7: $M_{\rm bc}$ distribution of $B \to K^*\pi^0$ fitted by Crystal ball function added Bifurecated Gaussian

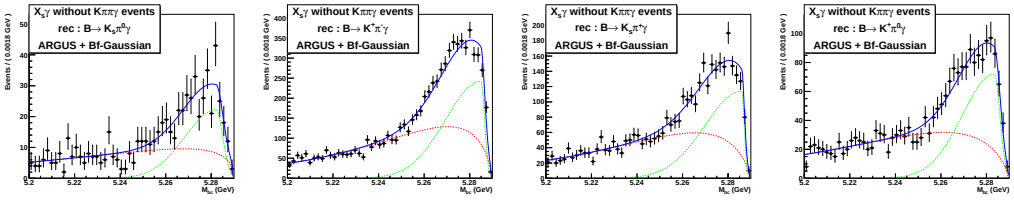

Figure 11.3.8: $M_{\rm bc}$ distribution of $X_s\gamma$ background fitted by Argus function added Bifurecated Gaussian

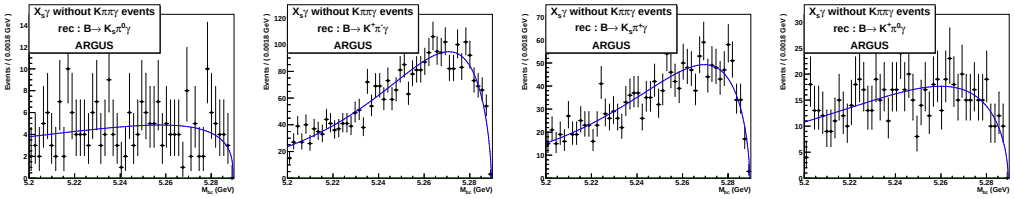

Figure 11.3.9: $M_{\rm bc}$ distribution of $X_s\gamma$ background without $B \to K\pi\pi\gamma$ components fitted by Argus function

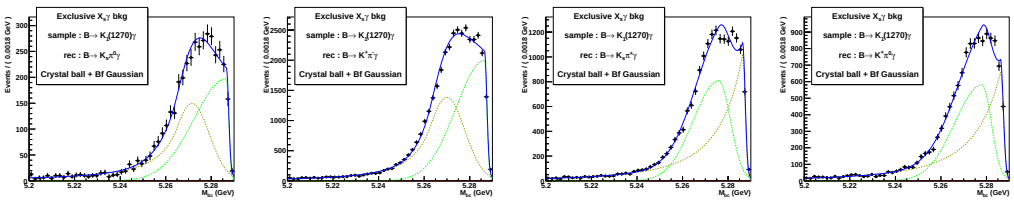

Figure 11.3.10: $M_{\rm bc}$ distribution of $B \to K_1(1270)\gamma$ fitted by Crystal ball function added Bifurecated Gaussian

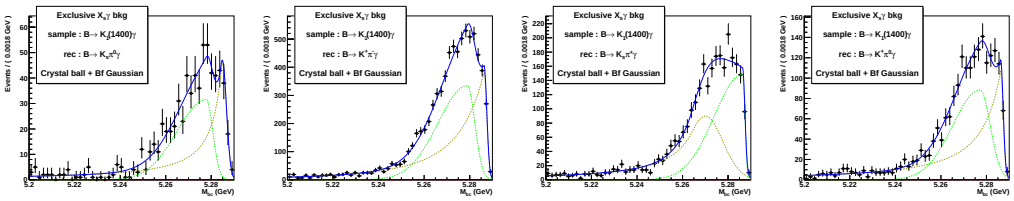

Figure 11.3.11: $M_{\rm bc}$ distribution of $B \to K_1(1400)\gamma$ fitted by Crystal ball function added Bifurecated Gaussian

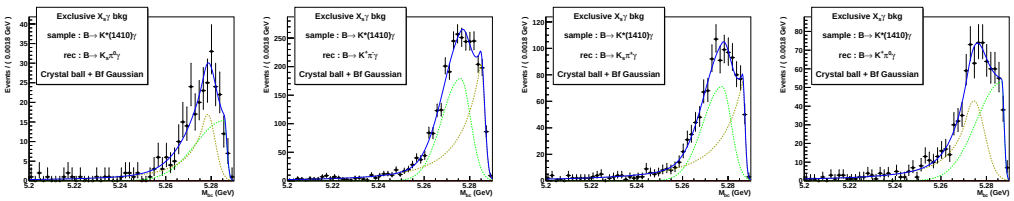

Figure 11.3.12: $M_{\rm bc}$ distribution of $B \to K^*(1410)\gamma$ fitted by Crystal ball function added Bifurecated Gaussian

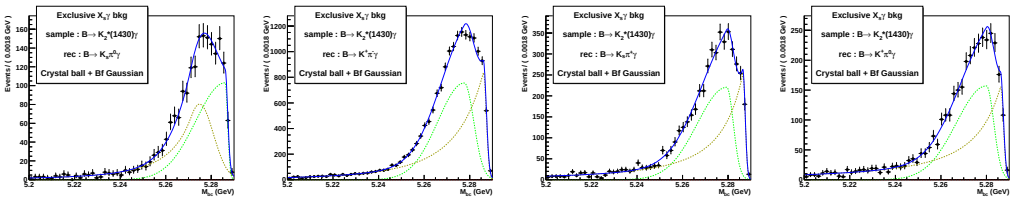

Figure 11.3.13: $M_{\rm bc}$ distribution of $B \to K_2^*(1430)\gamma$ fitted by Crystal ball function added Bifurecated Gaussian

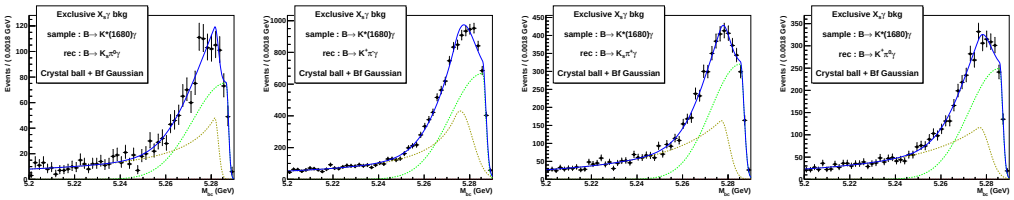

Figure 11.3.14: $M_{\rm bc}$ distribution of $B \to K^*(1680)\gamma$ fitted by Crystal ball function added Bifurecated Gaussian

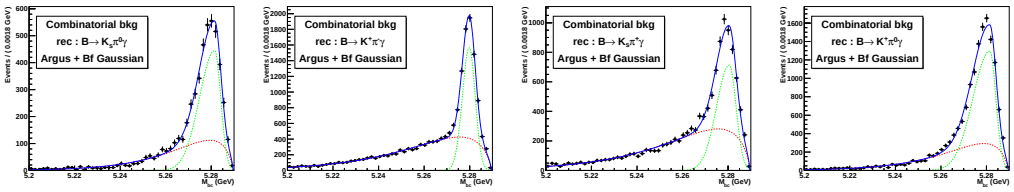

Figure 11.3.15: $M_{\rm bc}$ distribution of combinatorial background fitted by Argus function added Bifurecated Gaussian

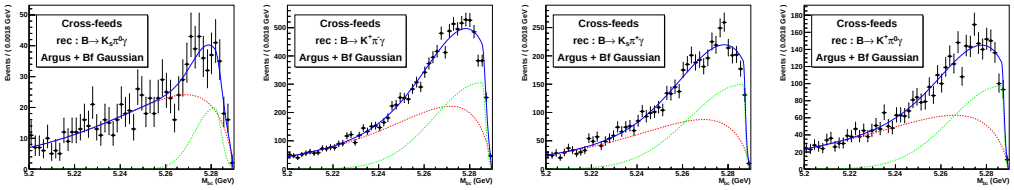

Figure 11.3.16: $M_{\rm bc}$ distribution of cross-feeds fitted by Argus function added Bifurecated Gaussian

binning \ fl-bin	1	2	3	4	5	6
SVD1 cos bin 1-th / pt bin 1-th	1.000 ± 0.042	0.000 ± 0.000	0.000 ± 0.000	0.000 ± 0.000	0.000 ± 0.000	0.000 ± 0.000
SVD1 cos bin 1-th / pt bin 2-th	1.000 ± 0.046	1.026 ± 0.040	0.000 ± 0.000	0.000 ± 0.000	0.000 ± 0.000	0.000 ± 0.000
SVD1 cos bin 1-th / pt bin 3-th	1.000 ± 0.058	0.000 ± 0.000	0.000 ± 0.000	0.000 ± 0.000	0.000 ± 0.000	0.000 ± 0.000
SVD1 cos bin 1-th / pt bin 4-th	1.000 ± 0.080	0.000 ± 0.000	0.000 ± 0.000	0.000 ± 0.000	0.000 ± 0.000	0.000 ± 0.000
SVD1 cos bin 2-th / pt bin 1-th	1.000 ± 0.032	0.000 ± 0.000	0.000 ± 0.000	0.000 ± 0.000	0.000 ± 0.000	0.000 ± 0.000
SVD1 cos bin 2-th / pt bin 2-th	1.000 ± 0.022	1.005 ± 0.022	1.020 ± 0.029	1.017 ± 0.035	1.008 ± 0.033	1.020 ± 0.033
SVD1 cos bin 2-th / pt bin 3-th	1.000 ± 0.028	1.023 ± 0.025	1.087 ± 0.031	0.979 ± 0.036	0.997 ± 0.033	0.999 ± 0.023
SVD1 cos bin 2-th / pt bin 4-th	1.000 ± 0.059	0.992 ± 0.029	0.964 ± 0.030	0.969 ± 0.041	0.929 ± 0.026	0.906 ± 0.016
SVD1 cos bin 3-th / pt bin 1-th	1.000 ± 0.033	1.039 ± 0.035	0.000 ± 0.000	0.000 ± 0.000	0.000 ± 0.000	0.000 ± 0.000
SVD1 cos bin 3-th / pt bin 2-th	1.000 ± 0.017	1.002 ± 0.018	0.976 ± 0.022	0.970 ± 0.031	0.889 ± 0.026	0.956 ± 0.028
SVD1 cos bin 3-th / pt bin 3-th	1.000 ± 0.022	0.986 ± 0.020	0.969 ± 0.023	0.898 ± 0.027	0.937 ± 0.022	0.949 ± 0.017
SVD1 cos bin 3-th / pt bin 4-th	1.000 ± 0.025	1.099 ± 0.023	1.059 ± 0.024	1.058 ± 0.028	1.029 ± 0.021	0.965 ± 0.012
SVD1 cos bin 4-th / pt bin 1-th	1.000 ± 0.025	1.045 ± 0.038	0.000 ± 0.000	0.000 ± 0.000	0.000 ± 0.000	0.000 ± 0.000
SVD1 cos bin 4-th / pt bin 2-th	1.000 ± 0.021	0.983 ± 0.021	0.942 ± 0.031	0.953 ± 0.038	0.966 ± 0.033	0.970 ± 0.032
SVD1 cos bin 4-th / pt bin 3-th	1.000 ± 0.030	0.973 ± 0.027	0.967 ± 0.033	0.979 ± 0.039	0.975 ± 0.030	0.961 ± 0.023
SVD1 cos bin 4-th / pt bin 4-th	1.000 ± 0.037	1.043 ± 0.030	1.029 ± 0.034	1.056 ± 0.038	1.035 ± 0.031	0.992 ± 0.018
SVD2 cos bin 1-th / pt bin 1-th	1.000 ± 0.014	1.025 ± 0.025	1.035 ± 0.021	0.948 ± 0.037	0.000 ± 0.000	0.000 ± 0.000
SVD2 cos bin 1-th / pt bin 2-th	1.000 ± 0.013	1.037 ± 0.020	1.010 ± 0.013	1.000 ± 0.016	1.016 ± 0.027	0.950 ± 0.020
SVD2 cos bin 1-th / pt bin 3-th	1.000 ± 0.020	1.046 ± 0.027	1.040 ± 0.016	1.019 ± 0.018	1.040 ± 0.027	0.976 ± 0.015
SVD2 cos bin 1-th / pt bin 4-th	1.000 ± 0.032	0.000 ± 0.000	1.056 ± 0.025	1.020 ± 0.027	1.060 ± 0.038	1.002 ± 0.018
SVD2 cos bin 2-th / pt bin 1-th	1.000 ± 0.013	1.005 ± 0.022	0.991 ± 0.018	0.988 ± 0.030	0.000 ± 0.000	0.000 ± 0.000
SVD2 cos bin 2-th / pt bin 2-th	1.000 ± 0.009	1.025 ± 0.013	1.015 ± 0.008	0.990 ± 0.011	0.979 ± 0.017	1.005 ± 0.013
SVD2 cos bin 2-th / pt bin 3-th	1.000 ± 0.012	1.039 ± 0.016	1.019 ± 0.009	1.021 ± 0.011	1.004 ± 0.016	0.963 ± 0.009
SVD2 cos bin 2-th / pt bin 4-th	1.000 ± 0.013	1.017 ± 0.017	1.026 ± 0.010	1.030 ± 0.011	1.028 ± 0.014	0.960 ± 0.007
SVD2 cos bin 3-th / pt bin 1-th	1.000 ± 0.012	1.000 ± 0.021	1.000 ± 0.016	1.005 ± 0.030	0.000 ± 0.000	0.000 ± 0.000
SVD2 cos bin 3-th / pt bin 2-th	1.000 ± 0.007	1.018 ± 0.011	1.020 ± 0.007	0.998 ± 0.009	0.971 ± 0.016	0.975 ± 0.011
SVD2 cos bin 3-th / pt bin 3-th	1.000 ± 0.009	1.018 ± 0.013	1.034 ± 0.008	1.011 ± 0.009	0.984 ± 0.012	0.988 ± 0.007
SVD2 cos bin 3-th / pt bin 4-th	1.000 ± 0.010	1.025 ± 0.013	1.038 ± 0.008	1.019 ± 0.008	1.017 ± 0.011	0.973 ± 0.005
SVD2 cos bin 4-th / pt bin 1-th	1.000 ± 0.009	1.047 ± 0.019	1.045 ± 0.016	1.020 ± 0.037	0.000 ± 0.000	0.000 ± 0.000
SVD2 cos bin 4-th / pt bin 2-th	1.000 ± 0.008	1.019 ± 0.012	1.003 ± 0.008	1.001 ± 0.011	0.993 ± 0.018	1.010 ± 0.013
SVD2 cos bin 4-th / pt bin 3-th	1.000 ± 0.011	1.008 ± 0.015	1.001 ± 0.009	0.987 ± 0.010	0.975 ± 0.016	0.961 ± 0.009
SVD2 cos bin 4-th / pt bin 4-th	1.000 ± 0.014	1.009 ± 0.017	1.012 ± 0.010	1.006 ± 0.011	1.015 ± 0.015	1.015 ± 0.007

Table 11.4.1: The table of detailed result of the efficiency ratio with standard $\mathbf{nisK_s}$ selction. The bin numbers of 1 to 6 at top of the table are the flight length bins. "0.000" means the bin which is rejected because of small number of events.

fl-bin / binning	1	2	3	4	5	6
SVD1 cos bin 1-th / pt bin 1-th	1.000 ± 0.043	0.000 ± 0.000	0.000 ± 0.000	0.000 ± 0.000	0.000 ± 0.000	0.000 ± 0.000
SVD1 cos bin 1-th / pt bin 2-th	1.000 ± 0.041	0.000 ± 0.000	0.000 ± 0.000	0.000 ± 0.000	0.000 ± 0.000	0.000 ± 0.000
SVD1 cos bin 1-th / pt bin 3-th	1.000 ± 0.057	0.000 ± 0.000	0.000 ± 0.000	0.000 ± 0.000	0.000 ± 0.000	0.000 ± 0.000
SVD1 cos bin 1-th / pt bin 4-th	1.000 ± 0.089	0.000 ± 0.000	0.000 ± 0.000	0.000 ± 0.000	0.000 ± 0.000	0.000 ± 0.000
SVD1 cos bin 2-th / pt bin 1-th	1.000 ± 0.033	0.000 ± 0.000	0.000 ± 0.000	0.000 ± 0.000	0.000 ± 0.000	0.000 ± 0.000
SVD1 cos bin 2-th / pt bin 2-th	1.000 ± 0.022	1.001 ± 0.021	1.022 ± 0.029	1.045 ± 0.037	0.977 ± 0.033	1.010 ± 0.033
SVD1 cos bin 2-th / pt bin 3-th	1.000 ± 0.032	1.051 ± 0.027	1.115 ± 0.033	1.026 ± 0.036	1.000 ± 0.031	1.011 ± 0.023
SVD1 cos bin 2-th / pt bin 4-th	1.000 ± 0.038	1.064 ± 0.029	1.039 ± 0.032	1.041 ± 0.074	0.992 ± 0.028	0.959 ± 0.017
SVD1 cos bin 3-th / pt bin 1-th	1.000 ± 0.029	1.042 ± 0.036	0.000 ± 0.000	0.000 ± 0.000	0.000 ± 0.000	0.000 ± 0.000
SVD1 cos bin 3-th / pt bin 2-th	1.000 ± 0.018	1.012 ± 0.018	0.979 ± 0.022	0.958 ± 0.029	0.865 ± 0.026	0.925 ± 0.026
SVD1 cos bin 3-th / pt bin 3-th	1.000 ± 0.024	1.014 ± 0.021	0.978 ± 0.024	0.904 ± 0.028	0.949 ± 0.023	0.958 ± 0.017
SVD1 cos bin 3-th / pt bin 4-th	1.000 ± 0.028	1.067 ± 0.023	1.042 ± 0.024	1.053 ± 0.031	1.024 ± 0.021	0.949 ± 0.012
SVD1 cos bin 4-th / pt bin 1-th	1.000 ± 0.025	1.027 ± 0.035	0.000 ± 0.000	0.000 ± 0.000	0.000 ± 0.000	0.000 ± 0.000
SVD1 cos bin 4-th / pt bin 2-th	1.000 ± 0.022	0.986 ± 0.020	0.946 ± 0.027	0.947 ± 0.035	0.972 ± 0.033	0.947 ± 0.032
SVD1 cos bin 4-th / pt bin 3-th	1.000 ± 0.033	0.979 ± 0.026	0.989 ± 0.031	0.989 ± 0.036	0.986 ± 0.031	0.969 ± 0.022
SVD1 cos bin 4-th / pt bin 4-th	1.000 ± 0.041	1.040 ± 0.030	1.031 ± 0.033	0.000 ± 0.000	1.049 ± 0.031	1.003 ± 0.018
SVD2 cos bin 1-th / pt bin 1-th	1.000 ± 0.014	1.019 ± 0.026	1.020 ± 0.020	0.000 ± 0.000	0.000 ± 0.000	0.000 ± 0.000
SVD2 cos bin 1-th / pt bin 2-th	1.000 ± 0.014	1.040 ± 0.020	1.010 ± 0.013	0.996 ± 0.016	1.007 ± 0.027	0.923 ± 0.020
SVD2 cos bin 1-th / pt bin 3-th	1.000 ± 0.021	1.054 ± 0.027	1.051 ± 0.016	1.027 ± 0.018	1.032 ± 0.026	0.977 ± 0.015
SVD2 cos bin 1-th / pt bin 4-th	1.000 ± 0.036	0.000 ± 0.000	1.068 ± 0.025	1.033 ± 0.027	1.061 ± 0.038	1.006 ± 0.018
SVD2 cos bin 2-th / pt bin 1-th	1.000 ± 0.013	0.994 ± 0.022	0.964 ± 0.017	0.955 ± 0.031	0.000 ± 0.000	0.000 ± 0.000
SVD2 cos bin 2-th / pt bin 2-th	1.000 ± 0.009	1.014 ± 0.012	1.004 ± 0.008	0.978 ± 0.010	0.959 ± 0.017	0.973 ± 0.013
SVD2 cos bin 2-th / pt bin 3-th	1.000 ± 0.013	1.039 ± 0.016	1.008 ± 0.009	1.002 ± 0.011	0.977 ± 0.016	0.932 ± 0.009
SVD2 cos bin 2-th / pt bin 4-th	1.000 ± 0.015	1.002 ± 0.017	1.012 ± 0.010	1.015 ± 0.010	1.008 ± 0.014	0.939 ± 0.006
SVD2 cos bin 3-th / pt bin 1-th	1.000 ± 0.012	0.990 ± 0.020	0.978 ± 0.016	0.967 ± 0.030	0.000 ± 0.000	0.000 ± 0.000
SVD2 cos bin 3-th / pt bin 2-th	1.000 ± 0.008	1.010 ± 0.011	1.009 ± 0.007	0.985 ± 0.009	0.957 ± 0.014	0.944 ± 0.010
SVD2 cos bin 3-th / pt bin 3-th	1.000 ± 0.010	1.003 ± 0.013	1.019 ± 0.008	0.993 ± 0.008	0.969 ± 0.012	0.958 ± 0.007
SVD2 cos bin 3-th / pt bin 4-th	1.000 ± 0.011	1.019 ± 0.013	1.042 ± 0.008	1.023 ± 0.008	1.018 ± 0.011	0.969 ± 0.005
SVD2 cos bin 4-th / pt bin 1-th	1.000 ± 0.010	1.047 ± 0.017	1.050 ± 0.015	1.025 ± 0.032	0.000 ± 0.000	0.000 ± 0.000
SVD2 cos bin 4-th / pt bin 2-th	1.000 ± 0.008	1.022 ± 0.012	1.012 ± 0.008	0.998 ± 0.010	0.984 ± 0.016	1.007 ± 0.012
SVD2 cos bin 4-th / pt bin 3-th	1.000 ± 0.012	1.015 ± 0.015	1.013 ± 0.009	0.992 ± 0.010	0.980 ± 0.015	0.974 ± 0.009
SVD2 cos bin 4-th / pt bin 4-th	1.000 ± 0.015	1.006 ± 0.018	1.009 ± 0.010	1.005 ± 0.011	1.012 ± 0.015	1.009 ± 0.007

Table 11.4.2: The table of detailed result of the efficiency ratio with standard $\mathbf{goodK_s}$ selction. The bin numbers of 1 to 6 at top of the table are the flight length bins. "0.000" means the bin which is rejected because of small number of events.

binning \ fl-bin	1	2	3	4	5	6
SVD1 cos bin 1-th / pt bin 1-th	0.980 ± 0.002	0.000 ± 0.000	0.000 ± 0.000	0.000 ± 0.000	0.000 ± 0.000	0.000 ± 0.000
SVD1 cos bin 1-th / pt bin 2-th	0.979 ± 0.002	0.975 ± 0.002	0.000 ± 0.000	0.000 ± 0.000	0.000 ± 0.000	0.000 ± 0.000
SVD1 cos bin 1-th / pt bin 3-th	0.988 ± 0.002	0.000 ± 0.000	0.000 ± 0.000	0.000 ± 0.000	0.000 ± 0.000	0.000 ± 0.000
SVD1 cos bin 1-th / pt bin 4-th	0.997 ± 0.002	0.000 ± 0.000	0.000 ± 0.000	0.000 ± 0.000	0.000 ± 0.000	0.000 ± 0.000
SVD1 cos bin 2-th / pt bin 1-th	0.983 ± 0.001	0.000 ± 0.000	0.000 ± 0.000	0.000 ± 0.000	0.000 ± 0.000	0.000 ± 0.000
SVD1 cos bin 2-th / pt bin 2-th	0.992 ± 0.001	0.985 ± 0.001	0.983 ± 0.001	0.984 ± 0.001	0.987 ± 0.001	0.983 ± 0.001
SVD1 cos bin 2-th / pt bin 3-th	0.991 ± 0.001	0.991 ± 0.001	0.989 ± 0.001	0.989 ± 0.001	0.990 ± 0.001	0.986 ± 0.001
SVD1 cos bin 2-th / pt bin 4-th	0.995 ± 0.001	0.991 ± 0.001	0.990 ± 0.001	0.992 ± 0.001	0.991 ± 0.001	0.985 ± 0.001
SVD1 cos bin 3-th / pt bin 1-th	0.988 ± 0.001	0.980 ± 0.002	0.000 ± 0.000	0.000 ± 0.000	0.000 ± 0.000	0.000 ± 0.000
SVD1 cos bin 3-th / pt bin 2-th	0.991 ± 0.001	0.985 ± 0.001	0.983 ± 0.001	0.980 ± 0.001	0.985 ± 0.001	0.985 ± 0.001
SVD1 cos bin 3-th / pt bin 3-th	0.990 ± 0.001	0.989 ± 0.001	0.987 ± 0.001	0.989 ± 0.001	0.989 ± 0.001	0.988 ± 0.001
SVD1 cos bin 3-th / pt bin 4-th	0.996 ± 0.001	0.990 ± 0.001	0.991 ± 0.001	0.990 ± 0.001	0.992 ± 0.001	0.986 ± 0.000
SVD1 cos bin 4-th / pt bin 1-th	0.986 ± 0.001	0.972 ± 0.002	0.000 ± 0.000	0.000 ± 0.000	0.000 ± 0.000	0.000 ± 0.000
SVD1 cos bin 4-th / pt bin 2-th	0.985 ± 0.001	0.975 ± 0.001	0.974 ± 0.001	0.972 ± 0.002	0.980 ± 0.001	0.977 ± 0.002
SVD1 cos bin 4-th / pt bin 3-th	0.994 ± 0.001	0.982 ± 0.001	0.980 ± 0.001	0.985 ± 0.001	0.986 ± 0.001	0.981 ± 0.001
SVD1 cos bin 4-th / pt bin 4-th	0.994 ± 0.001	0.988 ± 0.001	0.988 ± 0.001	0.985 ± 0.001	0.989 ± 0.001	0.987 ± 0.001
SVD2 cos bin 1-th / pt bin 1-th	0.991 ± 0.000	0.981 ± 0.001	0.981 ± 0.001	0.975 ± 0.002	0.000 ± 0.000	0.000 ± 0.000
SVD2 cos bin 1-th / pt bin 2-th	0.990 ± 0.000	0.986 ± 0.001	0.986 ± 0.000	0.984 ± 0.001	0.983 ± 0.001	0.976 ± 0.001
SVD2 cos bin 1-th / pt bin 3-th	0.993 ± 0.001	0.989 ± 0.001	0.991 ± 0.000	0.988 ± 0.001	0.986 ± 0.001	0.984 ± 0.001
SVD2 cos bin 1-th / pt bin 4-th	0.994 ± 0.001	0.000 ± 0.000	0.993 ± 0.001	0.992 ± 0.001	0.990 ± 0.001	0.986 ± 0.001
SVD2 cos bin 2-th / pt bin 1-th	0.989 ± 0.000	0.985 ± 0.001	0.984 ± 0.001	0.978 ± 0.001	0.000 ± 0.000	0.000 ± 0.000
SVD2 cos bin 2-th / pt bin 2-th	0.991 ± 0.000	0.985 ± 0.000	0.987 ± 0.000	0.985 ± 0.000	0.984 ± 0.001	0.979 ± 0.001
SVD2 cos bin 2-th / pt bin 3-th	0.994 ± 0.000	0.991 ± 0.000	0.990 ± 0.000	0.989 ± 0.000	0.987 ± 0.001	0.984 ± 0.000
SVD2 cos bin 2-th / pt bin 4-th	0.995 ± 0.000	0.994 ± 0.000	0.994 ± 0.000	0.991 ± 0.000	0.990 ± 0.000	0.983 ± 0.000
SVD2 cos bin 3-th / pt bin 1-th	0.991 ± 0.000	0.986 ± 0.001	0.980 ± 0.001	0.975 ± 0.001	0.000 ± 0.000	0.000 ± 0.000
SVD2 cos bin 3-th / pt bin 2-th	0.991 ± 0.000	0.986 ± 0.000	0.985 ± 0.000	0.984 ± 0.000	0.983 ± 0.001	0.976 ± 0.001
SVD2 cos bin 3-th / pt bin 3-th	0.993 ± 0.000	0.992 ± 0.000	0.990 ± 0.000	0.989 ± 0.000	0.988 ± 0.000	0.983 ± 0.000
SVD2 cos bin 3-th / pt bin 4-th	0.998 ± 0.000	0.995 ± 0.000	0.993 ± 0.000	0.991 ± 0.000	0.990 ± 0.000	0.983 ± 0.000
SVD2 cos bin 4-th / pt bin 1-th	0.986 ± 0.000	0.975 ± 0.001	0.972 ± 0.001	0.973 ± 0.001	0.000 ± 0.000	0.000 ± 0.000
SVD2 cos bin 4-th / pt bin 2-th	0.988 ± 0.000	0.982 ± 0.000	0.980 ± 0.000	0.978 ± 0.000	0.978 ± 0.001	0.971 ± 0.001
SVD2 cos bin 4-th / pt bin 3-th	0.991 ± 0.000	0.987 ± 0.001	0.987 ± 0.000	0.985 ± 0.000	0.983 ± 0.001	0.979 ± 0.000
SVD2 cos bin 4-th / pt bin 4-th	0.994 ± 0.000	0.991 ± 0.001	0.991 ± 0.000	0.990 ± 0.000	0.989 ± 0.001	0.983 ± 0.000

Table 11.4.3: The signal extraction correctness is shown in the table. These are calculated by $\frac{N_{fit}}{N_{truth}}$, where N_{fit} and N_{truth} are number of extracted signal events and truth events with standard **nisK$_S$** selction. The bin numbers of 1 to 6 at top of the table are the flight length bins. "0.000" means the bin which is rejected because of small number of events.

binning \ fl-bin	1	2	3	4	5	6
SVD1 cos bin 1-th / pt bin 1-th	0.995 ± 0.001	0.000 ± 0.000	0.000 ± 0.000	0.000 ± 0.000	0.000 ± 0.000	0.000 ± 0.000
SVD1 cos bin 1-th / pt bin 2-th	0.992 ± 0.001	0.000 ± 0.000	0.000 ± 0.000	0.000 ± 0.000	0.000 ± 0.000	0.000 ± 0.000
SVD1 cos bin 1-th / pt bin 3-th	0.996 ± 0.001	0.000 ± 0.000	0.000 ± 0.000	0.000 ± 0.000	0.000 ± 0.000	0.000 ± 0.000
SVD1 cos bin 1-th / pt bin 4-th	1.000 ± 0.001	0.000 ± 0.000	0.000 ± 0.000	0.000 ± 0.000	0.000 ± 0.000	0.000 ± 0.000
SVD1 cos bin 2-th / pt bin 1-th	0.996 ± 0.001	0.000 ± 0.000	0.000 ± 0.000	0.000 ± 0.000	0.000 ± 0.000	0.000 ± 0.000
SVD1 cos bin 2-th / pt bin 2-th	0.997 ± 0.000	0.993 ± 0.001	0.991 ± 0.001	0.947 ± 0.003	0.994 ± 0.001	0.990 ± 0.001
SVD1 cos bin 2-th / pt bin 3-th	0.995 ± 0.001	0.994 ± 0.001	0.992 ± 0.001	0.992 ± 0.001	0.993 ± 0.001	0.991 ± 0.001
SVD1 cos bin 2-th / pt bin 4-th	1.000 ± 0.000	0.995 ± 0.001	0.994 ± 0.001	0.996 ± 0.001	0.993 ± 0.001	0.987 ± 0.001
SVD1 cos bin 3-th / pt bin 1-th	0.997 ± 0.001	0.992 ± 0.001	0.000 ± 0.000	0.000 ± 0.000	0.000 ± 0.000	0.000 ± 0.000
SVD1 cos bin 3-th / pt bin 2-th	0.997 ± 0.000	0.992 ± 0.001	0.989 ± 0.001	0.988 ± 0.001	0.993 ± 0.001	0.991 ± 0.001
SVD1 cos bin 3-th / pt bin 3-th	0.996 ± 0.001	0.993 ± 0.001	0.991 ± 0.001	0.994 ± 0.001	0.995 ± 0.001	0.992 ± 0.001
SVD1 cos bin 3-th / pt bin 4-th	0.999 ± 0.000	0.995 ± 0.000	0.994 ± 0.001	0.994 ± 0.001	0.994 ± 0.001	0.989 ± 0.000
SVD1 cos bin 4-th / pt bin 1-th	0.998 ± 0.000	0.988 ± 0.001	0.000 ± 0.000	0.000 ± 0.000	0.000 ± 0.000	0.000 ± 0.000
SVD1 cos bin 4-th / pt bin 2-th	0.995 ± 0.001	0.989 ± 0.001	0.988 ± 0.001	0.986 ± 0.001	0.993 ± 0.001	0.993 ± 0.001
SVD1 cos bin 4-th / pt bin 3-th	0.998 ± 0.000	0.994 ± 0.001	0.992 ± 0.001	0.995 ± 0.001	0.993 ± 0.001	0.991 ± 0.001
SVD1 cos bin 4-th / pt bin 4-th	0.997 ± 0.001	0.993 ± 0.001	0.993 ± 0.001	0.000 ± 0.000	0.994 ± 0.001	0.992 ± 0.001
SVD2 cos bin 1-th / pt bin 1-th	0.997 ± 0.000	0.992 ± 0.001	0.994 ± 0.001	0.000 ± 0.000	0.000 ± 0.000	0.000 ± 0.000
SVD2 cos bin 1-th / pt bin 2-th	0.996 ± 0.000	0.993 ± 0.001	0.992 ± 0.000	0.992 ± 0.000	0.992 ± 0.001	0.988 ± 0.001
SVD2 cos bin 1-th / pt bin 3-th	0.998 ± 0.000	0.995 ± 0.001	0.995 ± 0.000	0.994 ± 0.000	0.992 ± 0.001	0.989 ± 0.000
SVD2 cos bin 1-th / pt bin 4-th	0.997 ± 0.001	0.000 ± 0.000	0.996 ± 0.001	0.996 ± 0.001	0.994 ± 0.001	0.990 ± 0.001
SVD2 cos bin 2-th / pt bin 1-th	0.996 ± 0.000	0.996 ± 0.000	0.995 ± 0.000	0.993 ± 0.001	0.000 ± 0.000	0.000 ± 0.000
SVD2 cos bin 2-th / pt bin 2-th	0.997 ± 0.000	0.994 ± 0.000	0.994 ± 0.000	0.993 ± 0.000	0.993 ± 0.000	0.988 ± 0.000
SVD2 cos bin 2-th / pt bin 3-th	0.996 ± 0.000	0.995 ± 0.000	0.993 ± 0.000	0.994 ± 0.000	0.993 ± 0.000	0.992 ± 0.000
SVD2 cos bin 2-th / pt bin 4-th	0.998 ± 0.000	0.997 ± 0.000	0.996 ± 0.000	0.994 ± 0.000	0.993 ± 0.000	0.986 ± 0.000
SVD2 cos bin 3-th / pt bin 1-th	0.998 ± 0.000	0.995 ± 0.000	0.993 ± 0.000	0.992 ± 0.001	0.000 ± 0.000	0.000 ± 0.000
SVD2 cos bin 3-th / pt bin 2-th	0.997 ± 0.000	0.994 ± 0.000	0.993 ± 0.000	0.992 ± 0.000	0.992 ± 0.000	0.985 ± 0.000
SVD2 cos bin 3-th / pt bin 3-th	0.996 ± 0.000	0.995 ± 0.000	0.994 ± 0.000	0.993 ± 0.000	0.994 ± 0.000	0.990 ± 0.000
SVD2 cos bin 3-th / pt bin 4-th	0.998 ± 0.000	0.998 ± 0.000	0.996 ± 0.000	0.994 ± 0.000	0.993 ± 0.000	0.987 ± 0.000
SVD2 cos bin 4-th / pt bin 1-th	0.994 ± 0.000	0.989 ± 0.001	0.990 ± 0.000	0.990 ± 0.001	0.000 ± 0.000	0.000 ± 0.000
SVD2 cos bin 4-th / pt bin 2-th	0.996 ± 0.000	0.993 ± 0.000	0.992 ± 0.000	0.991 ± 0.000	0.992 ± 0.000	0.988 ± 0.000
SVD2 cos bin 4-th / pt bin 3-th	0.997 ± 0.000	0.996 ± 0.000	0.995 ± 0.000	0.994 ± 0.000	0.993 ± 0.000	0.990 ± 0.000
SVD2 cos bin 4-th / pt bin 4-th	0.997 ± 0.000	0.995 ± 0.000	0.995 ± 0.000	0.993 ± 0.000	0.993 ± 0.000	0.989 ± 0.000

Table 11.4.4: The signal extraction correctness is shown in the table. These are calculated by $\frac{N_{fit}}{N_{truth}}$, where N_{fit} and N_{truth} are number of extracted signal events and truth events with standard $\mathbf{goodK_s}$ selction. The bin numbers of 1 to 6 at top of the table are the flight length bins. "0.000" means the bin which is rejected because of small number of events.

Bibliography

[1] G. Aad *et al.* [ATLAS Collaboration], Phys. Lett. B **716**, 1 (2012)

[2] S. Chatrchyan *et al.* [CMS Collaboration], Phys. Lett. B **716**, 30 (2012)

[3] Begeman, K. 1989, A&A, 223, 47 (1989)

[4] J. R. Ellis, M. K. Gaillard, D. V. Nanopoulos and S. Rudaz, Nucl. Phys. B 131, 285 (1977)

[5] R. Ammar et al. (CLEO Collaboration), Phys. Rev. Lett. **71**, 674 (1993).

[6] T. Hurth, Rev. Mod. Phys. **75** (2003) 1159 [hep-ph/0212304].

[7] T. Hurth and E. Lunghi, eConf C **0304052**, WG206 (2003) [hep-ph/0307142].

[8] Wilson KG. Phys. Rev. 179:1499 (1969)

[9] Wilson KG. Phys. Rev. D 3:1818 (1971)

[10] M. Beneke, G. Buchalla, M. Neubert and C. T. Sachrajda, Phys. Rev. Lett. **83**, 1914 (1999) [hep-ph/9905312].

[11] M. Beneke, G. Buchalla, M. Neubert and C. T. Sachrajda, Nucl. Phys. B **591**, 313 (2000)

[12] C. W. Bauer, S. Fleming, D. Pirjol and I. W. Stewart, Phys. Rev. D **63**, 114020 (2001)

[13] N. G. Deshpande, OITS-530.

[14] T. Saito *et al.* [Belle Collaboration], Phys. Rev. D **91**, no. 5, 052004 (2015)

[15] Ph.D thesis written by T. Saito.
Precision Measurements of Radiative B Meson Decay $B \to X_s\gamma$ with a Semi-inclusive Reconstruction Method `http://epx.phys.tohoku.ac.jp/~saito/Belle/dthesis_saito.pdf`

[16] H. M. Asatrian, C. Greub, A. Hovhannisyan, T. Hurth and V. Poghosyan, Phys. Lett. B **619**, 322 (2005)

[17] Xiao Zhen-Jun et al. 2006 Commun. Theor. Phys. **46** 895

[18] C. Greub, H. Simma, and D. Wyler, Nucl. Phys. B 434,39 (1995).895

[19] A. Paul and D. M. Straub, arXiv:1608.02556 [hep-ph].

[20] B. Aubert *et al.* [BaBar Collaboration], Phys. Rev. Lett. **103**, 211802 (2009)

[21] M. Nakao *et al.* [Belle Collaboration], Phys. Rev. D **69**, 112001 (2004)

[22] R. Aaij *et al.* [LHCb Collaboration], Nucl. Phys. B **867**, 1 (2013)

[23] W. Altmannshofer and D. M. Straub, Eur. Phys. J. C **75**, no. 8, 382 (2015)

[24] A. L. Kagan and M. Neubert, Phys. Lett. B **539**, 227 (2002)

[25] M. R. Ahmady and F. Mahmoudi, Phys. Rev. D **75**, 015007 (2007)

[26] F. Mahmoudi, Comput. Phys. Commun. **178**, 745 (2008)

[27] T. Blake, G. Lanfranchi and D. M. Straub, Prog. Part. Nucl. Phys. **92**, 50 (2017)

[28] S. Kurokawa, E. Kikutani Nucl. Phys. A **499**, 1 (2003)

[29] S. Kurokawa, E. Kikutani Particle Accelerators, 1990, Vol. 26, pp. 87-96

[30] A. J. Bevan *et al.* [BaBar and Belle Collaborations], Eur. Phys. J. C **74**, 3026 (2014)

[31] A. Abashian *et al.*, Nucl. Instrum. Meth. A **479**, 117 (2002).

[32] E. Nygard, et al., Nucl. Instr. and Meth. A 301 (1991) 506

[33] O. Toker, et al., Nucl. Instr. and Meth. A 340 (1994) 572.

[34] V. Chabaud, et al., Nucl. Instr. and Meth. A 368 (1996) 314.

[35] `http://evtgen.warwick.ac.uk/`

[36] http://www-pdg.lbl.gov/C. Patrignani, Chin. Phys. C **40**, no. 10, 100001 (2016).

[37] A. L. Kagan and M. Neubert, Eur. Phys. J. C **7**, 5 (1999) .

[38] P. del Amo Sanchez *et al.* [BaBar Collaboration], Phys. Rev. D **93**, no. 5, 052013 (2016)

[39] Belle Note 665.

[40] `http://hep.phys.s.u-tokyo.ac.jp/workshops/software2000/pdf/jtanaka2.pdf`

[41] Belle note 1253.

[42] `https://twiki.cern.ch/twiki/bin/view/Main/NeuroBayes`

[43] G. C. Fox and S. Wolfram, Phys. Rev. Lett. **41**, 1581 (1978).

[44] K. Abe *et al.* (Belle Collabolation), Phys. Lett. B **511**, 151 (2001).

[45] S.H. Lee *et al.* (Belle Collabolation), Phys. Rev, Lett. **91**, 261801 (2003).

[46] H. Kakuno *et al.* [Belle Collaboration], Nucl. Instrum. Meth. A **533**, 516 (2004)

[47] `https://root.cern.ch/doc/master/classTRandom3.html`

[48] J. P. Lees *et al.* [BaBar Collaboration], Phys. Rev. D **84**, 092007 (2011)

[49] T. Skwarnicki, Ph.D Thesis, Institute for Nueclear Physics, Krakow 1986; Desy internal report, DESY F31-86-02 (1986).

[50] ARGUS Collaboration, H. Albrecht *et al.*, Physics. Lett. B**241** (1990) 278.

[51] CLEO Collaboration, S. Kopp et al., Phys. Rev. D63, 092001 (2001)., 112001 (2004)

[52] Belle note 499

[53] Belle note 1165

[54] Belle note 779

[55] Belle note 323

[56] T. Allmendinger *et al.*, Nucl. Instrum. Meth. A **704**, 44 (2013)

[57] Belle note 645

[58] Heavy Flavor Averaging Group `http://www.slac.stanford.edu/xorg/hfag/osc/spring_2016/`

[59] B. Aubert *et al.* [BaBar Collaboration], Phys. Rev. Lett. **95**, 042001 (2005)

Note : "Belle note" is the internal review paper in Belle group.